Oxygen Reduction on Platinum: An EIS Study

by

Theodore Golfinopoulos

Submitted to the Department of Electrical Engineering and Computer Science
in partial fulfillment of the requirements for the degree of

Master of Science in Computer Science and Engineering

at the

MASSACHUSETTS INSTITUTE OF TECHNOLOGY

February 2009

Author .....
Department of Electrical Engineering and Computer Science
January 16, 2009

Certified by .....
Yang Shao-Horn
Associate Professor
Thesis Supervisor

Accepted by .....
Terry Orlando
Chairman, Department Committee on Graduate Students

Oxygen Reduction on Platinum: An EIS Study

by

Theodore Golfinopoulos

Submitted to the Department of Electrical Engineering and Computer Science
on January 16, 2009, in partial fulfillment of the
requirements for the degree of
Master of Science in Computer Science and Engineering

Abstract

The oxygen reduction reaction (ORR) on platinum over yttria-stabilized zirconia (YSZ) is examined via electrochemical impedance spectroscopy (EIS) for oxygen partial pressures between 10^{-4} and 1 atm and at temperatures between 475 and 700°C. Use of photolithographic techniques in electrode fabrication renders a precise geometry of the Pt electrodes. Circular electrode design leads to *cylindrical* symmetry so that models may be applied exactly to the experimental geometry. Interpretation of EIS spectra is carried out by reducing and then extending existing models, and is consistent with the postulate that ORR is rate-limited jointly by two surface chemical processes, namely, sorption/dissociation of molecular O_2 into $O_a^{\delta-}$ over Pt, as well as surface diffusion. Further, the novel experimental design, in conjunction with streamlined analysis techniques, provides accurate surface characterization within the electrochemical environment and allows for a more transparent comparison to relevant literature data. An adsorption coverage isotherm is extracted, and the surface diffusion coefficient is obtained for a number of experimental conditions. Extracted diffusivities fell between 2×10^{-2} and 2×10^{-7} cm^2/s, in agreement with literature values for the indicated temperature range.

Thesis Supervisor: Yang Shao-Horn
Title: Associate Professor

Acknowledgments

I emphatically express my gratitude to Dr. Gerardo-José La O' and Ethan Crumlin for their invaluable help and guidance, particularly with regard to fabricating the microelectrodes used in this study, and to Dr. Shuo Chen for her help in using the scanning electron microscopy facilities. I also gratefully acknowledge the contribution of my colleague, Dr. Serkan Naci Koc, from whose work this project was born. I have benefitted from a number of discussions with several members of the MIT community, including Professor Mehran Kardar in the Physics Department, Professor Markus Zahn of the Electrical Engineering and Computer Science Department, lecturers Dr. Benjamin Seibold and Dr. Aslan Kasimov of the Mathematics Department, and Professor Robert Savinell from Case Western Reserve University, who has spent the 2007-2008 academic year as a visiting professor in the Electrochemical Energy Laboratory at MIT. I'd also like to thank Professor Stuart Adler of the University of Washington for helpful conversations and advice. And to my advisor, Professor Yang Shao-Horn, my deepest thanks for wise mentoring, patience, and support. Finally, to all of my colleagues in the Electrochemical Energy Laboratory, I give my thanks and well wishes.

I'd also like to thank my wonderful family. And along those lines, I dedicate this volume to my grandparents,

Eunice and Martin, Iouannoula and Theodoros,

from whom and for whom I have learned so much.

TG, Fall 2008

Contents

List of Figures

List of Tables

Chapter 1

Introduction

This work will not solve the world's energy crisis. It will not reverse global warming. It will not help to conserve the world's precious oil reserves. It will not, by itself, make fuel cells a commercially viable technology. But perhaps it is a humble step in the right direction. It is my belief that science proceeds by myriad small steps, notwithstanding the occasional major breakthrough to generate renewed interest and ideas. And it is my hope that applied science will play a role in the solution of the challenges faced by the global society.

Most likely, the reader of this work has also chosen a career in the applied sciences, and agrees with these statements. And for this reason, I feel compelled to state something else: though we may believe in the ability of our profession to bring about social change while extending the grasp of the human mind, it is important for us to remember that the solution to society's great challenges will not come entirely from the laboratory. And, in the sense that we who have chosen technical and scientific professions are perhaps in a better position to understand how this technology affects, or might affect, our world, it is our responsibility to educate the society at large about how it can improve its lot, both in the present and in the future. It is therefore exceedingly important for the scientific community, and particularly the applied science community, to work together with government officials and other public servants at every level - municipal, state or provincial, national, and multinational - to better implement existing technological solutions and to prepare for long-term

changes. Imagine how much energy could be saved if governments made a real effort to enforce or reward the use of compact fluorescent lamps rather than incandescents[1], or of small heaters inside truck cabs. And imagine the possibilities of planning a comprehensive, sustainable energy infrastructure now, rather than twenty years from now.

This stated, I will proceed to the subject of the present work. The primary goal of this thesis is to characterize the oxygen reduction reaction on platinum over the solid electrolyte, yttria-stabilized zirconia (YSZ). Electrochemical impedance spectroscopy (EIS) is used to characterize the ORR, in conjunction with novel microfabrication techniques which render possible the precise control of electrode geometry. In characterizing ORR, I hope to demonstrate quantitatively that dissociative adsorption and surface diffusion together *colimit* the oxygen reduction reaction (ORR). This concept of colimited ORR on Pt has existed within the electrocatalysis community since at least as early as 1990, but the quantitative validation of the model is as yet incomplete [2].

1.1 Technological Context

Fuel cells stand alongside batteries, supercapacitors, flywheels, and many other devices as *energy storage* technology. The fuel of a fuel cell, whether hydrogen gas or methanol or some other chemical, always comes from elsewhere. These fuels, especially hydrogen, may serve as chemical energy storage media, whether as a means of making portable the mains power from large, centralized fission or fusion power plants, or for smoothing output from distributed renewable systems with irregular power generation, as wind or tidal turbines or solar panels. The fuel cell's role is to provide an efficient means of utilizing the energy stored within these chemical media, namely, by converting the chemical energy into electrical energy. Fuel cells are readily scalable, so that the same or similar technology might power a single small electronic

[1] Indeed, the U.S. has recently made major legislation in the regulation of lighting technology [13, sec. 321], as have many other nations.

device or an entire vehicle, a room in a house or a large hospital, and so forth. The technology is potentially portable, as both fuel and fuel cell can be taken onboard the device.

Within the family of fuel cell technologies, the solid oxide fuel cell (SOFC) has emerged as a promising candidate technology for small- to medium-scale power plants, especially in the capacity of a secondary power source, as, for example, a stationary backup generator or a source of electricity for large fossil-fuel powered vehicles. Because it requires high-temperatures (currently around 800℃ [26]) for operation, it is also ideal for use in combined-cycle power sources, where excess heat from the conventional power systems, whether electrical generators or large vehicle engines, or industrial operations may be used to elevate SOFC systems to operating temperatures.

The technology is distinguished by its use of oxygen ions passing through a solid oxide electrolyte (here, YSZ) as the ion conductor, rather than hydrogen ions (protons) as in the low-temperature proton-exchange membrane fuel cell (PEMFC). Major strides have been made in the technology by using thinner electrolyte layers to reduce electrolyte resistance. However, a slow oxygen reduction reaction still limits device performance.

But the oxide materials that make possible oxygen ion transport are also responsible for the requirement of a high operating temperature for SOFC devices. This high operating temperature has presented a major challenge to the technology's commercial deployment, particularly with regard to sealing the system and separating fuel and oxygen/air flows. Platinum is the best naturally available catalyst for ORR, and is widely used for proton-exchange membrane fuel cells [26], as well as industrially in CO oxidation [44]. Its use in SOFCs might allow lower operating temperatures. While it is more likely that mixed conductor oxide systems, as lanthanum strontium manganate (LSM) or lanthanum strontium ferrate (LSF) will see eventual use in commercial SOFCs [26], the study of platinum in the SOFC system is still of fundamental importance.

1.1.1 Previous Work

A shortcoming of many of the Pt/YSZ studies in the literature is that model parameters are often estimated only at the level of order-of-magnitude accuracy. Specific examples of this appear in the excellent body of work by Mitterdorfer and Gaukler, where the triple-phase boundary length, ℓ, is only estimated roughly for the study's porous electrodes [36, 37, 38]. Studies performed in the Electrochemical Energy Laboratory here at MIT, as well as in other laboratories, have sought to improve this situation by using photolithography to precisely define square electrodes, thereby specifying *by design* the geometrical parameters (chiefly perimeter length, area, and height above the YSZ substrate). However, in-plane studies have led to non-uniformity and uncertainty in the activity of different regions on the electrode[2]. The square-electrode through-plane scheme improves upon this situation, as the field distribution and current flow through the YSZ will have four-fold symmetry. However, the fields and currents at the corners of the electrode will be complex, and the surface problem will not reduce to one dimension. For larger square electrodes, this issue becomes less objectionable, but it is still troublesome.

The approach taken here is to use photolithography to precisely define cylindrically-symmetric geometries. The electrode radii studied are 12.5, 25, 50, 100, and 200 μm - multiple sizes are intended to help discern scaling behavior of the impedance (in particular, whether the scaling of each impedance contribution depends on perimeter or area of the electrode).

Cylindrical symmetry makes the triple phase boundary (TPB) universally uniform, and reduces the modeling problem from two dimensions to one. This eliminates a potential source of error in the analysis unrelated to the physical interpretation of the processes in the ORR pathway, allowing focus to remain on whether the envisioned reaction pathway, as encapsulated in the governing PDEs, adequately describes the actual pathway.

[2]Here, in-plane refers to the scheme where the electrode and counterelectrode sit in the same plane over the YSZ substrate, and oxygen ions travel laterally through the YSZ electrolyte. Through-plane refers to placing the electrode and counterelectrode on opposite sides of the solid electrolyte.

Figure 1-1 summarizes the evolution of microelectrode geometries from porous electrodes to the proposed cylindrically-symmetric variants. It should be noted that these other microelectrode designs are not without merit; the point emphasized here is that the proposed cylindrical geometry is the best scheme for the present purposes.

1.2 Goals of the Study

It has been stated that the primary goal of this work is to demonstrate that the oxygen reduction reaction on Pt over YSZ is *colimited* by dissociative adsorption and surface diffusion. In the process of achieving this goal, this work generates coverage isotherms for oxygen on polycrystalline Pt; such isotherms are difficult to find in the literature (see section 2.4.1), despite intense study of oxygen adsorption on Pt, and so the coverage data presented here is a potentially unique contribution. Also, diffusivity data is produced via analysis of EIS spectra. Again, while diffusion of oxygen on Pt has been extensively studied, diffusivity data is limited largely to high-vacuum, low-temperature conditions, with a few notable exceptions. Diffusivity data for oxygen on thin film polycrystalline Pt over a range of pressures and temperatures is therefore an important output of this work. Together, coverage and diffusivity data collected over a range of thermodynamic states provide a means of investigating the details of the platinum-oxygen system. Understanding this system is a key element in the design and synthesis of new catalyst materials for ORR, as the goal of of this design work might be interpreted in many ways as recreating the Pt-O system without using Pt[3].

Aside from these products of the study, the methodology presented here is also novel in many ways, and may be exported for the analysis of other similar, or perhaps not-so-similar, material systems. In particular, the use of microfabrication techniques to create experimental testbeds whose geometries are amenable to theoretical investigation represents a useful paradigm that may be emulated in other characterization studies. Further, the test system need not precisely recreate conditions in commercially-viable versions of the technology and material set in order to char-

[3]effectively alchemy!

acterize the processes in these systems; indeed, it may be essential to simplify the experimental picture to extract any useful information. In addition, the power of analysis via electrochemical impedance spectroscopy, and the ability of this class of experiments to isolate and inform on physical processes, is demonstrated.

Lastly, the thesis records a number of useful theoretical results, among them models of impedance spectra, coverage isotherms, and diffusivity functions from first principles at the level of statistical mechanics. Detailed derivations of this work are present in the appendices.

1.3 Outline

The remaining chapters of this thesis consist of

- an outline of the theoretical framework used to interpret EIS spectra,
- a presentation of details on the experimental implementation and analysis,
- a discussion of the results of the experiments,
- a proposal for future work related to the project, and
- concluding remarks.

The appendices include

- a list of symbols used in the work,
- derivations from statistical mechanics,
- derivations of electrochemical spectra for several different geometries and comparison with spectra previously derived elsewhere,
- a description of some of the mathematical details and useful tools of the fitting procedure,

- a generalization of a theoretical result obtained by Mitterdorfer and Gauckler [36] regarding the coverage value which maximizes current for a given temperature, and
- a set of tables containing estimates found in the literature of a number of model parameters from this study.

These bodies of work are connected; the theoretical picture generated is used to help design a better experiment, and to predict experimental outcomes prior to data collection. And as experimental realities present themselves, the theoretical picture is modified to focus on those aspects of the physical processes which might be understood from the available data and given uncertainties.

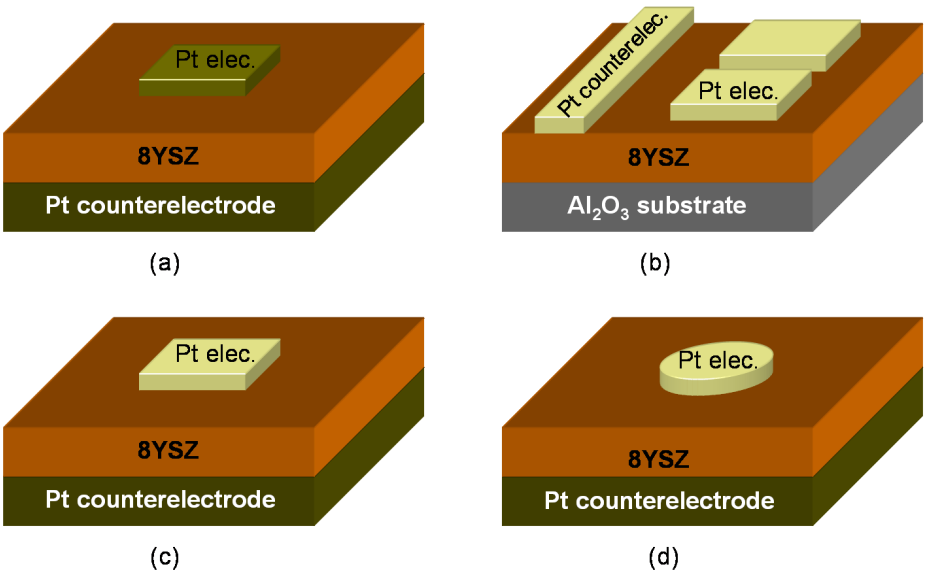

Figure 1-1: Evolution of microelectrode geometries leading to current configuration. Dark green-yellow represents porous Pt paste; light yellow is solid polycrystalline Pt. Not to scale. (a) Porous electrode in through-plane configuration (used in [36, 37, 38]). Porous electrodes, while more realistic to actual electrocatalyst design, are not ideal test platforms, as contact length and area are hard to determine, as are the effects of gas traveling through micropores in order to reach the catalytically-active region. (b) In-plane and (c) through-plane square electrode geometries with solid (non-porous) microstructure, defined by photolithography, allow for precise determination of geometrical parameters, but are still hard to analyze due to limited symmetries. (d) Circular microelectrodes in the through-plane configuration, with a uniform ground-plane on the electrolyte underside, creates cylindrical symmetry, reducing the dimensionality of the Pt surface analysis problem from two to one. In this case, error in the ORR modeling may be conclusively attributed to inadequacies in the proposed scheme of governing physical processes rather than an inexact solution to the PDE problem.

Chapter 2

Theory

2.1 Introduction

The purpose of this chapter is to arrive at a context for understanding electrochemical impedance spectra. Experiments described in subsequent chapters are designed in such a way as to reinforce the quantitative relationships described here.

An outline of the chapter is as follows: first, a model is introduced which proposes a set of physical processes at work during EIS experiments. These processes include gas adsorption onto a metal surface, transport of adsorbate on the surface, and charge transfer at the metal-electrolyte boundary. Subsequently, the chapter demonstrates how impedance expressions are derived from these first principles. Finally, assumptions inherent in the model, as well as the model's major shortcomings, are included in the discussion.

2.2 Model

2.2.1 Physical Processes

Adsorption/Desorption and Isotherm

Theoretical treatment of gas adsorption onto metals begins with the seminal model of Irving Langmuir, which dates to 1916 [28, see also [51]]. The theory likens the

adsorption process to a chemical reaction,

$$A_{gas} + \alpha s \underset{k_{des}}{\overset{k_{ads}}{\rightleftharpoons}} \alpha A_{ads} \tag{2.1}$$

Here, "reactants" in the model are the gas molecules, A_{gas}, and vacant adsorption sites on the surface, s; the "products" consist of the adsorbate population, A_{ads}. Parameter, α, represents the stoichiometry of the adsorption reaction and allows for the description of dissociation and association in the surface reaction. k_{ads} and k_{des} are the rate constants for the adsorption and desorption reactions. The law of mass action applied to 2.1 produces kinetic relations which can be solved for the equilibrium case to produce an isotherm relating gas concentration to adsorbate coverage.

In the Langmuir model is found most of the essential concepts of adsorption - adsorption site limitation (by reaction with empty sites, s, which may be related to adsorbate coverage as $s = \Gamma - A_{ads}$, where Γ is the total number of surface sites), association/dissociation, and adsorption/desorption activation (through appropriate interpretation of k_{ads} and k_{des}). It may be further extended by adding additional reactions to create a kinetic hierarchy, which might be used to treat multi-step reactions, multilayer adsorption, and so forth. Its two main shortcomings are its phenomenological nature, which renders interpretation of parameters (particularly the rate constants) somewhat imprecise, and its inability to gracefully handle interactions between adsorbates (which would manifest themselves in a dependence of the rate constants on A_{ads})[1].

The application of the Langmuir model to the present case is demonstrated in the initial studies of ORR on Pt by Mitterdorfer and Gauckler; there, the model takes the form [36, 37],

$$P + 2\Gamma(1-\theta) \underset{k_{des}}{\overset{k_{ads}}{\rightleftharpoons}} 2\Gamma\theta \tag{2.2}$$

where P is the O_2 gas partial pressure. The use of the gas partial pressure instead of

[1]The Langmuir model also assumes a uniform surface; it is conceivable that additional coupled reactions might be added to describe a nonuniform surface. However, despite the fact that nonuniform surfaces are the rule rather than the exception, for simplicity's sake, they are generally excluded from the discussion herein.

the gas concentration results in different units for each of the reaction rate constants, but in general there is some ambiguity as to the choice of A_{gas}, as the gas exists in a different medium than the surface concentration. One option would be to let A_{gas} be a sticking probability, with k_{ads} representing the number of oxygen atoms impinging on the surface per unit time; then the rate constants may be compared more naturally.

More recent theoretical descriptions of adsorption have extended the kinetics approach of the Langmuir model [12], blended the kinetics approach with principles from statistical mechanics [25], used state transition theory and Fermi's Golden Rule to analyze the adsorption step [16], and conducted first-principles simulations to analyze stable states [49], among other contributions. Tang et al. have created a phase diagram showing the stable phases of chemisorbed atomic O on the Pt(111) surface [49]. This is a very useful reference for understanding the structure of the adsorbate layer; also useful is its set of energetics data with interaction energies for the first several diagrams of a diagram expansion.

The work by Kreuzer et al. is particularly suitable for the purposes of this paper in that it incorporates and explains experimentally-determined parameters, in particular, chemisorption and physisorption binding energies, dissociation barriers, and sticking coefficients [25] (see Appendix F for literature-recorded values of these parameters). The authors combine a kinetics and equilibrium statistical mechanics approach to model the sorption process; this scheme is typified by the expression,

$$\left(\frac{d\theta}{dt}\right)_{ad-des} = S(\theta, T)\left[a_s \frac{\lambda}{h}(P - \overline{P})\right], \tag{2.3}$$

where $a_s = \frac{1}{\Gamma}$ is the area per adsorption site so that $a_s \frac{\lambda}{h} P$ is the total flux rate of impinging particles per adsorption site, $\lambda = h/\sqrt{2\pi m_{O_2} k_B T}$ is the thermal wavelength of the oxygen gas with m_{O_2} the mass of an oxygen molecule, P is the instantaneous gas pressure and $\overline{P}$ the pressure corresponding to equilibrium at the instantaneous coverage, and S the sticking coefficient (the probability that an impinging particle will adsorb). An advantage of this scheme is that data for S exists from surface studies

[20, 17, 56, 54, 58, for example]. For our purposes, we might more conveniently define the instantaneous, linearized adsorption rate, α, in the perturbation limit where $\Delta P = P - \overline{P}$ is small, and $\tilde{\theta}$ is a small perturbation in coverage, as (see Appendix C)

$$\left(\frac{d\theta}{dt}\right)_{ad-des} = -\alpha\tilde{\theta} = -S(\theta, T)\left[a_s \frac{\lambda}{h}\left(\frac{\partial P}{\partial \theta}\right) d\theta\right]. \tag{2.4}$$

The quantity, $\frac{\partial P}{\partial \theta}$, is readily evaluated from the coverage isotherm (see Appendix B),

$$\left(\frac{\theta}{1-\theta} e^{\beta u_0 \theta}\right)^2 = e^{2\beta\epsilon} \frac{z_{v,ads}^2}{z_{v,r,gas}} \frac{P\lambda^3}{k_B T} \tag{2.5}$$

as

$$\frac{\mathrm{d}P}{\mathrm{d}\theta} = 2P\left(\beta u_0 + \frac{1}{\theta(1-\theta)}\right). \tag{2.6}$$

u_0 relates to the energetics of adsorbate-adsorbate interactions; it is positive when reactions are repulsive and negative when they are attractive. Also, $\beta \equiv 1/(k_B T)$.

A detailed derivation of the coverage isotherm from statistical mechanics first principles appears in Appendix B; see also [22, 25, 9] for methods[2]. Implicit in the use of this quantity is the statement that the rates of adsorption and desorption are equal at equilibrium. As such, the desorption process need never be modeled explicitly so long as the equilibrium rate of adsorption is known at the instantaneous coverage.

While seemingly more complex, 2.3 actually does not introduce a greater number of parameters than present in the Langmuir sorption expression in 2.2. What's more, all parameters present in 2.3 may be extracted or estimated from surface studies in the literature [17, 18, 20, 25, 29, 54, 56]; Appendix F lists many parameter values found in the literature. This and other similar modifications to 2.2 help to make the results of EIS data analysis more transparent with respect to the current body of

[2]It may seem odd to take the derivative of pressure with respect to coverage when, in fact, pressure is an experimental control variable. However, we are interested in an approximation for the relative difference of pressure from that which *would* give equilibrium at the instantaneous coverage, and for this purpose, the derivative above is appropriate.

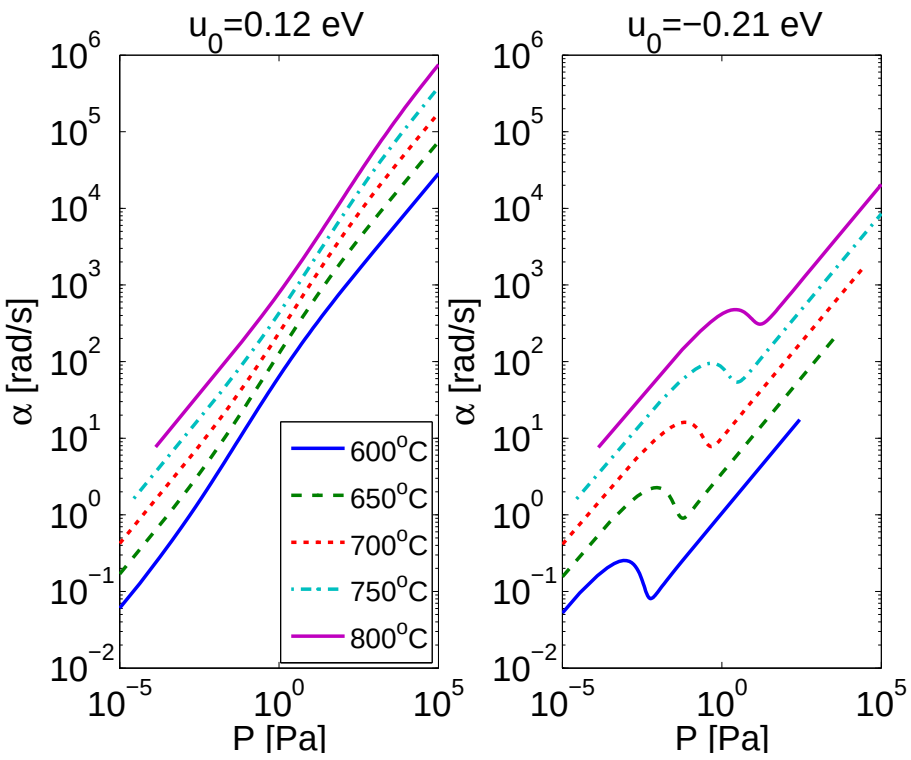

Figure 2-1: The linearized net adsorption rate, α, against pressure for several temperatures. The plot on the left displays the parameter when interactions between adsorbates are repulsive according to the interaction energy listed in [56]; on the right, when interactions are attractive according to the interaction energetics in [49] for the p(2×2) configuration.

existing work.

Figure 2-1 plots the linearized net adsorption rate against pressure for several temperatures. Behavior is monotonic in pressure for repulsive interactions between adsorbates, but can go through a maximum and a minimum when interactions are attractive.

Transport

Once oxygen molecules adsorb and dissociate on the surface, they must migrate to the Pt-YSZ interface. Platinum is not an ion conductor, so we can expect surface diffusion to be the dominant mechanism of transport. The starting point for a theoretical interpretation of diffusion phenomena is the phenomenological Fick's law,

$$\begin{aligned} J &= -D\nabla C \\ \frac{\partial\theta}{\partial t} &= \nabla\left[D(\theta)\nabla\theta\right] \end{aligned} \tag{2.7}$$

which states that the diffusion flux, J, is proportional to, and flows down, the concentration gradient, and that the total particle number is conserved[3], ∇C. The constant of proportionality, D, is called the *diffusion coefficient* or the *diffusivity*. Fick's law may be derived by considering Brownian motion of non-interacting particles [32], and is mathematically identical to Fourier's law of heat diffusion and a family of related phenomenological relations. For non-interacting particles undergoing random walks (e.g. molecules in a dilute gas, phonons, etc.), D is constant with respect to concentration. In fact, even for uniform media, D should not be expected to be a constant with respect to C so long as non-hard-core interactions between diffusing particles exist[4]. The effect of concentration (density) on the diffusion coefficient has been the subject of a number of theoretical studies [42, 4, 9, 57], one of the more influential of which is that by Reed and Ehrlich from 1981 [42], which pointed out that the driving force for diffusion is a gradient in the *chemical potential*. To help understand the mechanisms that result in a dependence of D on concentration, Reed and Ehrlich introduced a factorization, now standard in the literature [9, 57], of the form (in one dimension, x),

$$J = -L_T \frac{\partial\mu}{\partial x} \tag{2.8}$$

where L_T is a phenomenological transport coefficient. By comparison with 2.7,

[3]In reviewing literature and in communications with colleagues, I have found that there is occasional confusion as to how Fick's law applies to situations in other than three dimensions. The general rule is that the flux represents flow normal to a differential unit of dimension $d-1$, where d is the number of dimensions. C is the concentration per unit d-dimensional volume, and is in units of number/length^d. The diffusivity, D, *always* has units of length^2/time. Here, we are interested in surface phenomena; consequently, the flux is per unit *length*, and concentration per unit *area*.

[4]There might also exist strong interactions between diffusing particles and the medium, but these might be viewed as "indirect" interparticle interactions, and could be treated as such mathematically.

$$J = -L_T \frac{\partial \mu}{\partial x} = -L_T k_B T \left(\frac{\partial \mu / k_B T}{\partial \theta} \right) \left(\frac{\partial \theta}{\partial x} \right), \tag{2.9}$$

we can now identify the diffusion coefficient as

$$D = -L_T k_B T \left(\frac{\partial \mu / k_B T}{\partial \theta} \right) \tag{2.10}$$

This can be further decomposed into a tracer diffusion prefactor,

$$D_0 = -L_T k_B T \tag{2.11}$$

and a dimensionless thermodynamic factor,

$$\chi_t = \frac{\partial \mu / k_B T}{\partial \theta}, \tag{2.12}$$

related to the mean square concentration fluctuation over the spatial domain. D_0 is the diffusion coefficient which arises when particle-particle interactions are negligible (in which case χ_t tends to unity).

Using an extension of this theory by Bokun et al. [9], and simplifying their results with the mean field approximations used throughout this paper, we can get a simple analytical expression for D highlighting the dependence of D on θ:

$$D(\theta) = D_0 e^{-\beta\epsilon} e^{\theta\beta u_0} \left(1 + \beta u_0 \theta (1 - \theta)\right) \tag{2.13}$$

ϵ is the adparticle binding energy to the surface. The diffusion energy barrier is contained in D_0. A derivation of this expression is given in Appendix B.

Figure 2-2 displays the dependence of D on coverage predicted by this result. D increases with θ for repulsive interactions between adsorbates ($u_0 > 0$) and decreases with θ for attractive interactions ($u_0 < 0$). This behavior might be intuited by reasoning that adsorbates tend to stick together with attractive interactions, slowing down transport, and to push each other apart when interactions are repulsive, speeding up transport. When u_0=0, hard-sphere interactions still exist by merit of the

site-limiting requirement (each lattice site can only support one adsorbate). However, in this limit, there is *no* change in D with respect to θ, as shown in [42]. It is noteworthy that when $-\beta u_0 > 4$, the expression predicts values for D less than zero. This is not necessarily unphysical - it simply states that transport proceeds up the concentration gradient instead of down because high-concentration clumps are finally energetically-favorable enough to defeat random motions in determining the evolution of concentration. However, in this case, interactions are the dominant driving force of transport instead of a correction to Brownian motion, and as such, the simple diffusivity expressions presented here are probably fairly inaccurate beyond the qualitative description given above.

It is reassuring that the diffusion data reported by Mitterdorfer and Gauckler tend to reproduce the behavior seen in Figure 2-2, although those authors are skeptical of the accuracy of this particular work [37] due to the simplicity of the adsorption isotherm used in their modeling.

Załuska-Kotur et al. take a different approach from [9], invoking a Markovian master equation for the hopping model to derive an analytical expression for the chemical diffusion coefficient without the Reed-Ehrlich factorization [57]. However, care must be exercised in applying the results from this and other studies based around the hopping model, as diffusion by a Markov process is only realistic for thermal energies sufficiently lower than the migration energy barrier. For the high-temperatures of the present work, this is an important limitation to these kinds of lattice-hopping models of diffusion [4] (of which the model derived from Bokun et al. is one).

There is a lot of excellent experimental work on surface diffusion in general, and oxygen diffusion on Pt in particular; however, extensive data of diffusion dependence on coverage, particularly in the temperature and coverage regimes relevant to this experiment, are hard to find in the literature [4, 30, 53]. In 2.5.2, we will examine some of the data provided by Mitterdorfer and Gauckler in their EIS study of ORR on Pt-YSZ [37].

Appendix F lists diffusivity parameters for O_2 on Pt found in the literature and

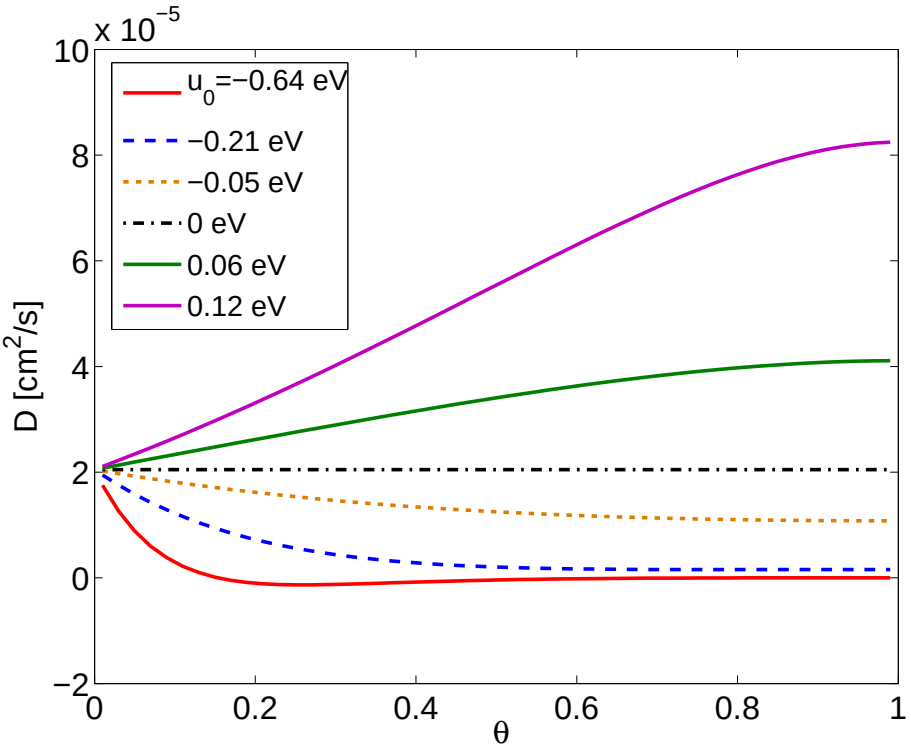

Figure 2-2: Dependence of diffusion coefficient on coverage after mean-field approach to account for adsorbate interactions. *D increases* with coverage when interactions are *repulsive* and *decreases* when interactions are attractive.

used here in theoretical calculations.

Charge Transfer

Upon adsorption, oxygen picks up a quantity of charge from the Pt surface - this quantity depends on the state into which the oxygen adsorbs [14]. There is some uncertainty as to how much charge the oxygen ions pick up on polycrystalline Pt, and how much must be transferred before incorporation into the YSZ solid electrolyte, and, indeed, what steps are involved in the incorporation process [2]. However, if a single charge transfer/incorporation step is assumed which (a) adjusts the oxygen oxidation state until it is appropriate to enter or exit the electrolyte and (b) accounts for oxygen ions entering or leaving a vacancy in the YSZ, we might write a phenomenological kinetic relation accounting for the charge transfer step as

$$\Gamma\theta + \mathrm{V}_{\ddot{\mathrm{O}}} + (\times - \delta^-)e^- \underset{k_{-1}}{\overset{k_1}{\rightleftharpoons}} \mathrm{O}_{\mathrm{O}}^{\times} + \Gamma(1-\theta). \tag{2.14}$$

where k_1 is the forward electrochemical rate constant, k_{-1} the backward, $\mathrm{V}_{\ddot{\mathrm{O}}}$ is the oxygen vacancy concentration inside the YSZ (material constant), $\mathrm{O}_{\mathrm{O}}^{\times}$ the oxygen ions concentration, $(\times - \delta^-)e^-$ is representative of a final charge transfer before adsorbate incorporation into the YSZ, and the term, $\Gamma(1-\theta)$ is the empty-site concentration on the surface. Here, $\times$ is the oxidation state of oxygen in the electrolyte, and δ^- that on the Pt surface. This formulation is employed in the work of Mitterdorfer and Gauckler [36, 37, 38], and leads to an expression for the flux of oxygen ions *into* the YSZ:

$$\phi(r_{tpb})_{\text{into YSZ}} = \Gamma\theta k_1 \mathrm{V}_{\ddot{\mathrm{O}}} - \Gamma(1-\theta)k_{-1}\mathrm{O}_{\mathrm{O}}^{\times} \tag{2.15}$$

The electric current *into* the YSZ is simply the flux multiplied by the total TPB length, ℓ, and the total charge transferred by each oxygen anion incorporation, $-nq_e$ (here, n=2):

$$I = -nq_e\ell\phi(r_{tpb})_{\text{into YSZ}} = nq_e\ell\Gamma((1-\theta)k_{-1}\mathrm{O}_{\mathrm{O}}^{\times} - \theta k_1 \mathrm{V}_{\ddot{\mathrm{O}}}) \tag{2.16}$$

where θ here is evaluated at the triple phase boundary.

This provides a constraint relating Faradaic current and coverage, and will provide a boundary condition in the determination of the coverage profile on the surface.

2.2.2 Perturbation Formalism

The premise of electrochemical impedance spectroscopy is that the applied sinusoidal voltage is sufficiently small so as only to perturb the system in a *linear* manner. The natural place to enforce this requirement is the only time-varying state variable: coverage. It is convenient to decompose the coverage as

$$\theta = \bar{\theta} + \tilde{\theta} \approx \bar{\theta}, \tag{2.17}$$

where $\bar{\theta}$ is the mean or equilibrium coverage and $\tilde{\theta}$ is a small, time-varying perturbation.

To extend the small-signal formalism to parameters that depend upon coverage, we carry out a Taylor series expansion for any such quantity, $f(\theta)$, in θ about $\bar{\theta}$,

$$f(\theta) = \sum_{n=0}^{\infty} \frac{1}{n!} \left[\frac{\mathrm{d}^n f}{\mathrm{d}\theta^n}\right]_{\bar{\theta}} \tilde{\theta}^n = f(\bar{\theta}) + \left[\frac{\mathrm{d}f}{\mathrm{d}\theta}\right]_{\bar{\theta}} \tilde{\theta} + \cdots \tag{2.18}$$

Assuming the series is well-ordered such that the higher-order terms decay, we desire that $f(\theta) = f(\bar{\theta}) + \left[\frac{\mathrm{d}f}{\mathrm{d}\theta}\right]_{\bar{\theta}} \tilde{\theta} + \mathscr{O}(\tilde{\theta}^2) \approx f(\bar{\theta})$, or

$$f(\bar{\theta}) \gg \left[\frac{\mathrm{d}f}{\mathrm{d}\theta}\right]_{\bar{\theta}} \tilde{\theta} \tag{2.19}$$

This is the zeroth-order approximation for coverage-dependent values; the model parameters for which this approximation is employed are the diffusion coefficient, D, and effective net adsorption rate, α. More will be said on the applicability of this approximation in 2.5.2.

Rewriting the governing differential equations from the previous sections with the perturbation scheme, we obtain

$$\left(\frac{\partial \tilde{\theta}}{\partial t}\right)_{transport} \approx D(\bar{\theta})\nabla^2\tilde{\theta} \tag{2.20}$$

$$\left(\frac{\mathrm{d}\theta}{\mathrm{d}t}\right)_{ad-des} = S(\bar{\theta}, T)\left[a_s \frac{\lambda}{h}(P - \overline{P})\right], \tag{2.21}$$

2.2.3 Synthesis of Governing Equations

When the adsorption and diffusion relations are combined with charge transfer at the triple phase boundary within the perturbation limit, the result is the following governing differential equation,

$$\frac{\partial \tilde{\theta}}{\partial t} = D(\bar{\theta})\nabla^2\tilde{\theta} - \alpha(\bar{\theta})\tilde{\theta} \tag{2.22}$$

with boundary conditions,

$$\begin{gathered} 1.\, \phi_r(R_e;t) = \frac{I}{nq_e\ell} = -D(\bar{\theta})\Gamma\nabla\tilde{\theta} \quad \text{Flux condition at Pt-YSZ interface} \\ 2.\, \phi_r(0) = 0 \quad \text{Flux condition at origin} \end{gathered} \tag{2.23}$$

Here, ϕ_r is the radial component of the oxygen ion flux over the Pt surface (number per unit length per unit time), R_e the radius of the circular electrode, and $\ell = 2\pi R_e$ the triple phase boundary length[5]. The tangential component of the flux is zero by symmetry. We will make use of the reaction in 2.14 for the Faradaic current, I, at the Pt-YSZ interface,

$$I = nq_e\ell\Gamma\left[k_{-1}\mathrm{O}_{\mathrm{O}}^{\times}(1-\theta) - k_1\mathrm{V}_{\ddot{\mathrm{O}}}\theta\right] \tag{2.24}$$

where the forward and backward electrochemical rate constants, k_{-1} and k_1, are defined as

$$k_{-1} = k_{-1,0}e^{b_{-1}v} \tag{2.25a}$$

$$k_1 = k_{1,0}e^{b_1 v} \tag{2.25b}$$

with

$$b_{-1} \equiv \frac{q_e}{k_B T}(1-\zeta) \tag{2.26a}$$

$$b_1 \equiv -\frac{q_e}{k_B T}\zeta. \tag{2.26b}$$

v is the overpotential above the equilibrium voltage, $v = V - V_{eq}$, and $\zeta \in [0,1]$ is the charge transfer coefficient[6] between the forward and backward reactions, and is usually around $\frac{1}{2}$.

[5]These are two Neumann boundary conditions, and so only the relative changes of $\tilde{\theta}$ are specified. However, these relative shifts in $\tilde{\theta}$ must be about zero by merit of the fact that this quantity is defined as the perturbation about $\bar{\theta}$.

[6]or Tafel constant, symmetry factor

2.3 Solution and Impedance

Detailed derivations for the expressions given below appear in Appendix C. This appendix also includes derivations for two other geometries and boundary conditions, and places the results in a more general context.

2.3.1 Solution to Governing Equations

The governing differential equation found above may be solved exactly in certain restricted cases. One of these is the case of a circular electrode geometry. The circular symmetry, combined with the negative sign before the coefficient, α, suggests that the solutions will be in the form of a zeroth-order modified Bessel function of the first kind, $\mathrm{M}_0(x)$ [7]. The solution is written as

$$\tilde{\theta}(r) = \frac{\tilde{I}}{nq_e\Gamma\ell D/\xi}\frac{\mathrm{M}_0(r/\xi)}{\mathrm{M}_1(R_e/\xi)} \tag{2.27}$$

where r is the radial coordinate,

$$\xi \equiv \sqrt{\frac{D}{j\omega+\alpha}} \tag{2.28}$$

is the length-scale of the decay in perturbations from the triple phase boundary, and M_1 is the first-order modified Bessel function of the first kind.

It is noteworthy that $\tilde{\theta}$ is proportional to $\tilde{I}$, where the tilde over the current represents this quantity's phasor-domain transform. This proportionality holds across multiple geometries and boundary conditions.

[7] The traditional notation for the modified Bessel function uses an I [1]; however, an M is utilized here to avoid confusion with current. Also, it is the negative sign before α which distinguishes the solution as a *modified* Bessel function; this is just for convenience. In general, the modified Bessel function of the first kind is related to the Bessel function of the first kind via $\mathrm{M}_p(x) = \mathrm{J}_p(jx)/j^p$, where j is the imaginary number (also otherwise referred to as $-i$, and again renamed as per the electrical engineering convention to avoid confusion with current!).

2.3.2 Impedance

Finally, by expanding the Faradaic current to first order in both θ and the overpotential, v, substituting the previously-determined relations for the derivatives, and taking advantage of the fact that $\tilde{\theta} \propto I$, we arrive at an expression for impedance for the cylindrical geometry,

$$Z_{cyl} = R_{ct}\left(1 + \frac{\mathrm{M}_0\left(R_e/\xi\right)\partial I/\partial\theta}{nq_e\ell\Gamma\mathrm{M}_1\left(R_e/\xi\right)D/\xi}\right) \tag{2.29}$$

where

$$R_{ct} \equiv \left(\frac{\partial I}{\partial v}\right)^{-1} \tag{2.30}$$

Using the expression for Faradaic current in 2.24, the charge transfer resistance is calculated as

$$R_{ct} \equiv \left(\frac{\partial I}{\partial v}\right)^{-1} = \left[nq_e\ell\Gamma\left(b_{-1}k_{-1}\mathrm{O}_{\mathrm{O}}^{\times}\left(1-\theta\right) - b_1k_1\mathrm{V}_{\ddot{\mathrm{O}}}\theta\right)\right]^{-1} \tag{2.31}$$

and for $\frac{\partial I}{\partial\theta}$,

$$\frac{\partial I}{\partial\theta} = nq_e\ell\Gamma\left(k_1\mathrm{V}_{\ddot{\mathrm{O}}} + k_{-1}\mathrm{O}_{\mathrm{O}}^{\times}\right). \tag{2.32}$$

When the Faradaic current is nominally zero, a useful simplification is obtained from 2.24, namely,

$$\frac{\theta\left(R_e\right)}{1-\theta\left(R_e\right)} = \frac{k_{-1}\mathrm{O}_{\mathrm{O}}^{\times}}{k_1\mathrm{V}_{\ddot{\mathrm{O}}}}, \tag{2.33}$$

where $\theta\left(R_e\right)$ is the coverage at the edge of the electrode, with R_e the electrode radius. Invoking the perturbation approximation everywhere on the surface of the electrode, $\theta = \bar{\theta} + \tilde{\theta} \approx \bar{\theta}$, $\theta\left(R_e\right) \approx \bar{\theta}$. The quantity,

$$R_{ct}\frac{\partial I}{\partial\theta}\frac{1}{nq_e\ell\Gamma},$$

becomes

$$\frac{1}{nq_e\ell\Gamma\frac{q_e}{k_BT}\bar{\theta}(1-\bar{\theta})}$$

so that the frequency-dependent part of the cylindrical-electrode impedance is

$$Z_{cyl,f} = \frac{\mathrm{M}_0\left(R_e/\xi\right)}{nq_e\ell\Gamma\frac{q_e}{k_BT}\bar{\theta}(1-\bar{\theta})\mathrm{M}_1\left(R_e/\xi\right)D/\xi} \tag{2.34}$$

The benefit here is that the electrochemical rate constants, k_1 and k_{-1}, are[8] removed from the problem, and are replaced by terms involving only the coverage and other known quantities. The coverage is already required in other parts of the model, and as such, we have lowered the number of model parameters by one[9], a huge savings in computational effort. Further, while it is difficult to determine the coverage precisely, there are a number of theoretical and experimental methods for estimating it [25, e.g.], whereas the electrochemical rate constants are much more complicated quantities to work with.

Another interesting property of this simplification is that we have entirely removed the electrolyte from the description of the frequency-dependent impedance component. As such, within a frequency-independent offset, the same Faradaic component of the impedance spectrum should arise regardless of the electrolyte identity. This is a result of allowing the system to reach equilibrium; the equilibrium potential relative to a consistent reference electrode may vary from electrolyte to electrolyte, but the behavior is the same for all electrodes for perturbations around this equilibrium point. This is a readily testable claim, but is not investigated experimentally in the present work (see Chapter 5).

[8] or, more precisely, their ratio is

[9] two if the individual rate constant values are never sought

2.4 Interpretation of Results

2.4.1 Coverage Isotherm

Despite the fact that sorption of oxygen on platinum has been intensively studied using surface methods [14, 17, 18, 30, 20, 44, 48, 49, 53, 54, 56], there is very little data available on the coverage isotherm. Légaré et al. report an isotherm[10] limited to three values of coverage [29]; those authors believe that they are the first to publish such a finding. Kishimoto et al. condense the findings of Mizusaki et al. into an isotherm [23], though in the work of Mizusaki et al., coverage is determined indirectly via electrochemical measurements [40] (as opposed to using one of various surface techniques, as low energy electron diffraction (LEED), or secondary ion mass spectrometry (SIMS)). Similarly, Mitterdorfer and Gauckler, using indirect electrochemical techniques, report a coverage isotherm for one temperature in [37], and use parameters extracted from their studies to simulate constant coverage contours for various temperatures and pressures [38].

The coverage isotherm derived in Appendix B might be used to get an idea of the coverages to be encountered in the experimental conditions here. Figure 2-3 shows the calculation from this coverage isotherm using parameters from literature corresponding to the Pt(111) surface. It roughly agrees with the limited coverage data available in [29]. The reference to $\theta_{max} = 1/4$ relates to an assumed saturation in the (2×2) configuration; other configurations are possible, including (2×1) with a saturation coverage of $\frac{1}{2}$ [49]; however, (2×2) seems more prevalent in the literature and ought to be more stable [17, 18, 49].

In the present work, we have a means for estimating coverage independently at each temperature and pressure for which an electrochemical impedance spectrum is collected. We also have a theoretical reference with which to compare these observations (see Section 2-3). As such, we have the opportunity to expand on the limited coverage data available in the literature.

It should be noted that the exact number of available sites on the polycrystalline

[10] in fact, isocoverage - perhaps isokalypsi or isostroma

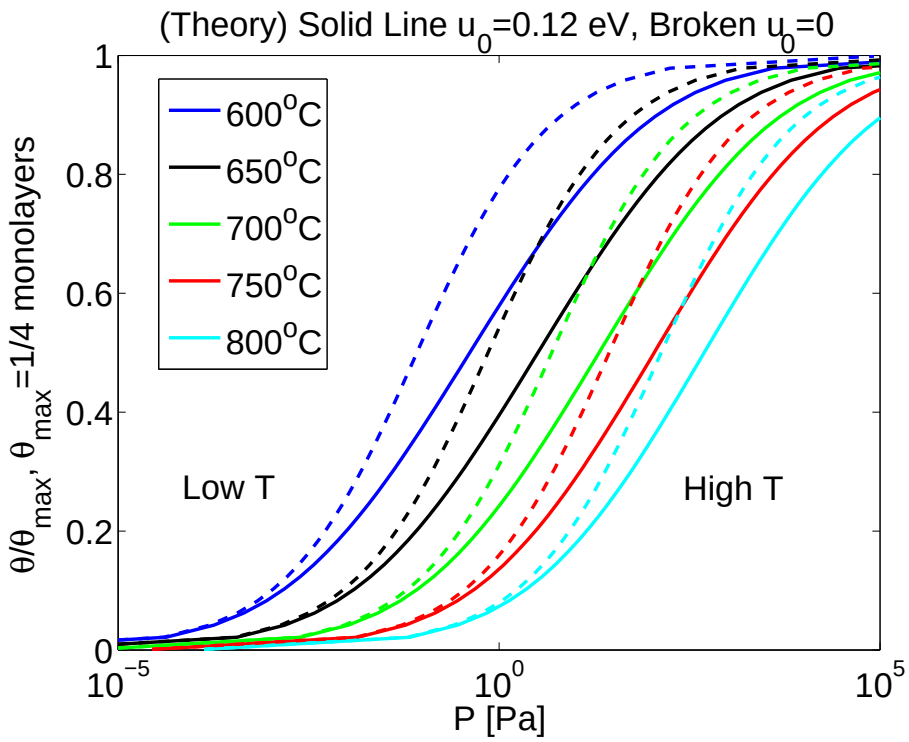

Figure 2-3: Coverage isotherm for oxygen on Pt(111). Binding (1.6 eV) and net interaction (0.12 eV) energies are from [56] (net *repulsive* interaction); vibrational frequencies for adsorbed oxygen from [48]. The isotherm without interactions is also shown. The effect of repulsive interactions is to depress the isotherms such that higher pressures are needed to achieve the same coverages; the phenomenon is more pronounced at higher coverages, and vanishes as $\theta \rightarrow 0$, as expected. Attractive interactions pull up the isotherms toward lower pressures.

Pt surface is not known from literature. Mitterdorfer and Gauckler estimate the value at $1{\times}10^{19}$ m^{-2}, which is the number of Pt atoms per square meter on the Pt(111) surface. While this may cause difficulties in calculating accurate estimates for model parameters based on first principles (in particular, α), it does not hamper efforts to extract these parameters from EIS data, though it requires multiple spectra at different thermodynamic states to ensure proper normalization for coverage from trends in the data.

2.4.2 Diffusion Coefficient

Analysis of the diffusion coefficient provides a number of rich topics of inquiry. To begin, literature data themed on oxygen adsorption on Pt typically record *repulsive* interactions between adsorbates [25, 56], while diffusion dependence on coverage for this system suggests *attractive* interactions [4, 37, 42, 53]. In fact, interactions between adsorbates show both attractive and repulsive interactions depending upon position and configuration according to quantum-level studies [49]. As such, studying diffusion gives insight into the interplay between adsorbate-surface and adsorbate-adsorbate.

Accurate estimation of this parameter also gives indirect information about defect properties of the surface, and as such provides a means to characterize different electrode treatments. And there are a number of fundamental questions that remain regarding surface diffusion of adsorbed gas on transition metals [4] - diffusivity data from higher temperatures and pressures would be a valuable resource for this endeavor, where many studies are carried out under high vacuum.

Figure 2-4 shows the diffusion coefficient calculation using repulsive interaction energies from literature, as well as a plot with an arbitrary attractive energy which more closely resembles literature diffusivity trends.

It should be remembered, however, that the simple picture of diffusion described in this chapter and in Appendix B is likely far from quantitatively accurate. A number of exotic behaviors, including ballistic motion coupled to adsorption and dissociation events as well as other forms of long jumps, are not accounted for [4]. Fortunately, the bulk surface diffusivity that appears in the EIS expressions assumes nothing about diffusion mechanisms; only that diffusion is Fickian and the diffusivity is roughly equal to its equilibrium value everywhere on the surface. As such, the diffusion coefficient determined from EIS data may well provide insight into how transport is affected by the presence of these interesting behaviors.

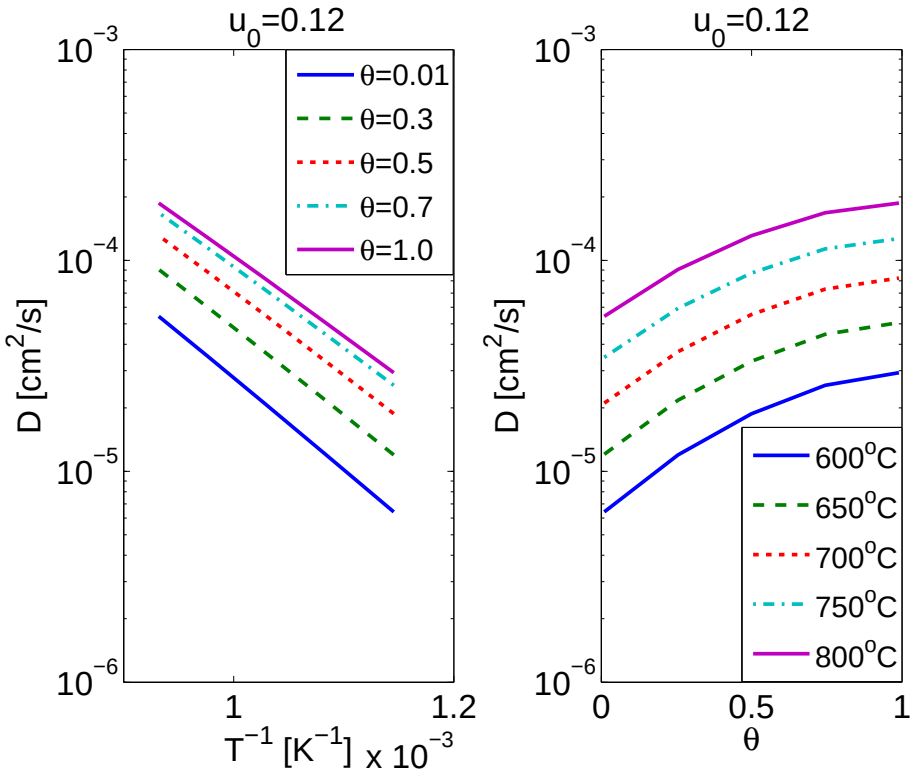

(a)
u_0=0.12eV

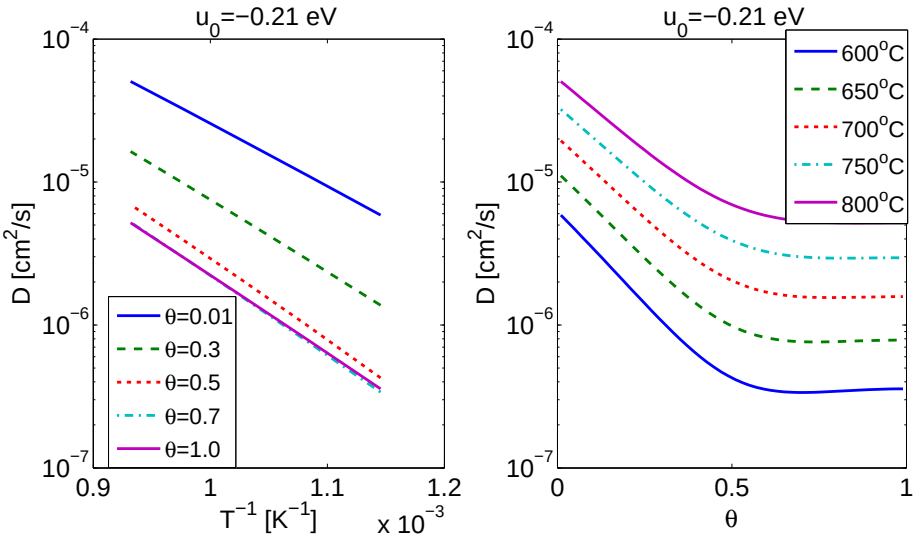

(b)
u_0=−0.21eV

Figure 2-4: (Top) Arrhenius plot of diffusion coefficient and dependence on coverage when u_0 represents a net repulsive at around 0.12 eV [56]. (Bottom) for u_0 representing a net attractive at around -0.21 eV.

2.4.3 Rate-Limiting Steps

One of the principle goals of this study is to determine which, if any, physical processes are dominant in controlling the rate of oxygen reduction on Pt.

A recent contribution to the long-lived debate on this subject was made by Robertson and Michaels in 1990 [2]. These authors suggested that diffusion and adsorption together *colimit* the oxygen reduction reaction. By "colimit", it is meant that both of these physical processes - transport and sorption - are important in determining the overall rate.

With the impedance model we have presented, we are already in a position to gauge the validity of this idea[11]. The approach will be to take the limit as diffusion becomes infinitely fast or very slow relative to adsorption, and vice versa. This is accomplished by taking the limit of the impedance as $D \to 0$ and $D \to \infty$ and as $\alpha \to 0, \infty$. We'll focus on the frequency-dependent impedance in 2.34, since this is where D and α appear explicitly.

In taking the limit as $D \to \infty$, it is useful to take a mathematical detour to examine the series expansions defining the Bessel functions,

$$\begin{aligned} \mathrm{M}_p(x) = \mathrm{J}_p(jx)/j^p &= \sum_{n=0}^{\infty} (-1)^n \frac{(jx/2)^{(2n+p)}}{n!(n+p)!j^p} \\ &= \sum_{n=0}^{\infty} \frac{(x/2)^{(2n+p)}}{n!(n+p)!} \\ &= \frac{1}{p!}\left(\frac{x}{2}\right)^p + \frac{1}{(1+p)!}\left(\frac{x}{2}\right)^{2+p} + \cdots \end{aligned} \tag{2.35}$$

where J_p is the p^{th}-order Bessel function of the first kind. Then the initial expansion terms for the zeroth- and first-order modified Bessel functions are,

[11] It should be noted that Adler [2] already defends the notion of a colimited reaction from an EIS perspective examining the same physical processes considered in this work - here, the discussion extends to the case of finite geometry.

$$\mathrm{M}_0(x) = 1 + \frac{x^2}{4} + \cdots \tag{2.36a}$$

$$\mathrm{M}_1(x) = \frac{x}{2} + \frac{x^3}{16} + \cdots \tag{2.36b}$$

If $x = R_e/\xi$, with $\xi \equiv \sqrt{\frac{D}{j\omega+\alpha}}$ then to first order in x, the limit of $D \to \infty$ ($x = R_e/\xi \to 0$ such that electrode is small compared to length scale of the coverage perturbation) gives for the frequency-dependent impedance

$$\begin{aligned} Z_{cyl,f} &= \frac{\mathrm{M}_0\left(R_e/\xi\right)}{nq_e\ell\Gamma\frac{q_e}{k_BT}\bar{\theta}(1-\bar{\theta})\mathrm{M}_1\left(R_e/\xi\right)D/\xi} \\ &= \frac{2}{nq_e\ell\Gamma\frac{q_e}{k_BT}\bar{\theta}(1-\bar{\theta})R_eD/\xi^2} \\ &= \frac{2}{nq_e\ell\Gamma\frac{q_e}{k_BT}\bar{\theta}(1-\bar{\theta})R_e(j\omega+\alpha)} \end{aligned} \tag{2.37}$$

D has entirely vanished from the impedance expression, so that only the sorption parameter remains.

The impedance in this limit is the same as that for a parallel combination of a resistor and capacitor with effective capacitance, $C_{eff} = R_e/(2R_{ct}\frac{\partial I}{\partial\theta}\frac{1}{nq_e\ell\Gamma}) = nq_e\ell\Gamma\frac{q_e}{k_BT}\bar{\theta}(1-\bar{\theta})R_e/2$, and effective resistance, $R_{eff} = 1/(\alpha C_{eff}) = 2/[\alpha nq_e\ell\Gamma\frac{q_e}{k_BT}\bar{\theta}(1-\bar{\theta})R_e]$, where, again, R_e is the electrode radius. Because $\ell \propto R_e$, C_{eff} scales with the square of the electrode radius, and R_{eff} with the inverse square.

When D becomes very small, $x = R_e/\xi \to \infty$ such that the perturbations in coverage are localized to the edge of the electrode and cannot sense its size. We take advantage of

$$\lim_{x\to\infty}\frac{\mathrm{M}_0(x)}{\mathrm{M}_1(x)} = 1 \tag{2.38}$$

In this case, the frequency-dependent impedance becomes

$$\begin{aligned} Z_{cyl,f} &= \frac{\mathrm{M}_0\left(R_e/\xi\right)}{nq_e\ell\Gamma\frac{q_e}{k_BT}\bar{\theta}(1-\bar{\theta})\mathrm{M}_1\left(R_e/\xi\right)D/\xi} \\ &= \frac{1}{nq_e\ell\Gamma\frac{q_e}{k_BT}\bar{\theta}(1-\bar{\theta})D/\xi} \\ &= \frac{1}{nq_e\ell\Gamma\frac{q_e}{k_BT}\bar{\theta}(1-\bar{\theta})\sqrt{D(j\omega+\alpha)}} \end{aligned} \tag{2.39}$$

where this expression has obtained a term, $1/\sqrt{j\omega+\alpha}$, characteristic of the "Gerischer" impedance element, which models a system with processes behaving as a distributed reaction in conjunction with diffusion for a one-dimensional, semi-infinite domain [2]. Now, the impedance at $\omega = 0$ scales as the inverse of R_e, as compared with R_e^{-2} for R_{eff}.

It is important to point out that at low frequencies where $\omega \ll \alpha$, the limit where $D \to \infty$ is *the same* as the limit where $\alpha \to 0^+$. Likewise, the limit where $D \to 0^+$ is the same as that where $\alpha \to \infty$. It is for this reason that ORR on Pt has been termed "colimited" by diffusion and sorption. The understanding we obtain from the colimiting concept is that the ORR rate[12] is tied to the ratio, $l_\delta \equiv \sqrt{D/\alpha}$, termed the *utilization length* by Adler [2]. The impedance response has distinctive shapes depending on the value of l_δ relative to the electrode dimensions, R_e.

Figure 2-5 displays the Nyquist (complex plane) and Bode plots in the three regimes, $l_\delta \ll R_e$, $l_\delta \gg R_e$, and $l_\delta \backsim R_e$. The different lines show the effect of changing only the electrode radius from below the utilization length, l_δ, to above. The figure does not show the fact that, in addition to the shape change, there is also a shift in impedance magnitude because $\ell \propto R_e$. Here, the offset, $R_{ct} + R_{ysz}$, the sum of the charge transfer and ohmic electrolyte resistances, has been set to zero for all plots to reveal in the Bode plot the angle at which the Nyquist loci depart from the real axis. Further, the precise dependence of R_{ysz} on the electrode radius, R_e, is likely complicated and afield from the primary interests of this work.

When l_δ is much smaller than the electrode dimensions, only the edge of the

[12] at least, in the linearized perturbation limit

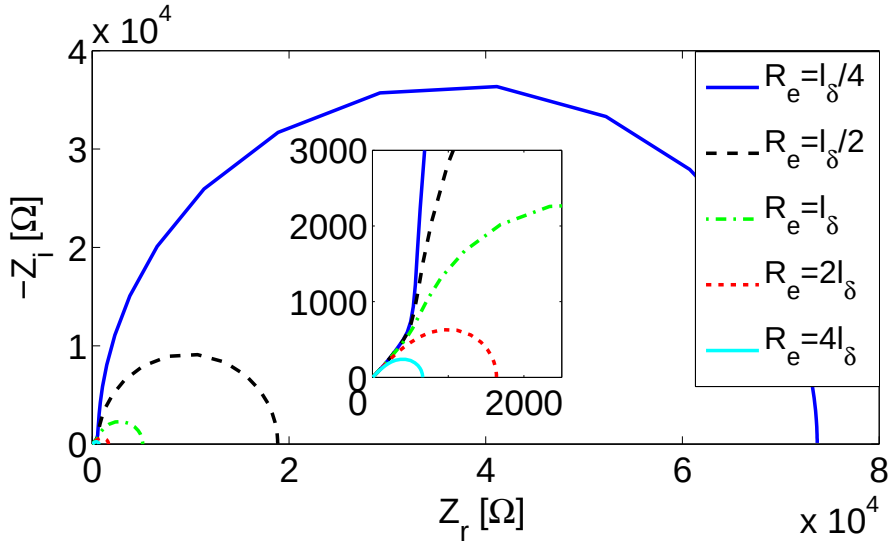

(a)

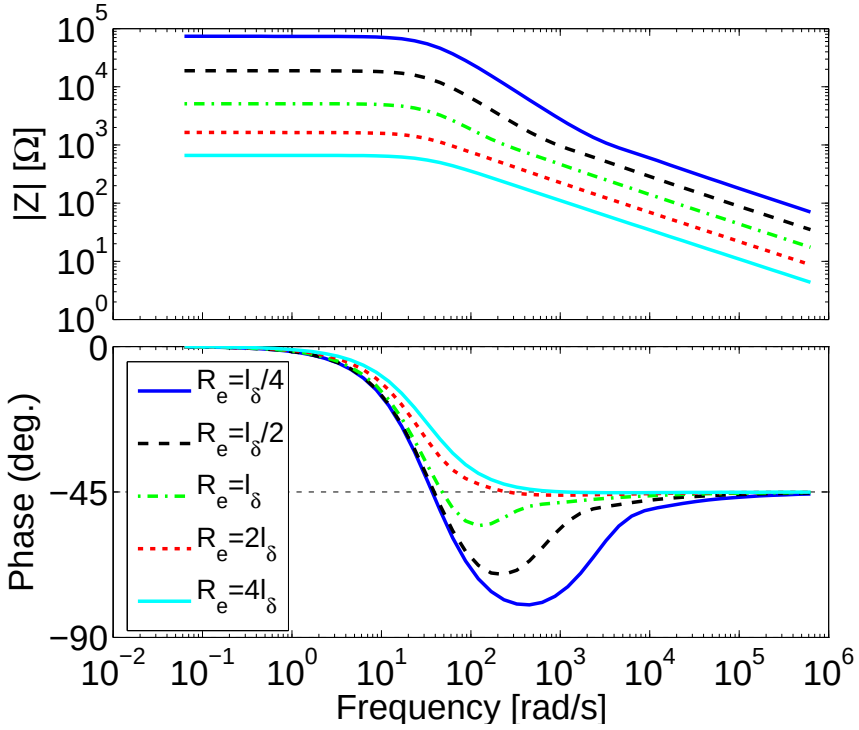

(b)

Figure 2-5: (a) Nyquist plot of *frequency-dependent* impedance response predicted for cylindrical geometry ($\epsilon = 1.6$ eV, $u_0 = -0.21$ eV with $\theta = \frac{1}{2}$, $l_\delta \approx 1$ μm). The inset is a detail of the high-frequency region and shows the transition from the semicircular to the Gerischer-like response as the radius is increased. (b) Bode magnitude and phase plots of cylindrical impedance element. The phase angle plot shows the frequency at which the loci in the Nyquist plot departs from 45°, and suggests the shape of the Nyquist plot.

electrode close to the triple phase boundary participates in delivering oxygen ions to the electrolyte - for these semi-infinite electrodes, the situation approaches that for which the Gerischer model applies, and indeed, the impedance expression attains such a form. For $l_\delta \rightarrow \infty$, the entire electrode surface participates in the ORR. Coverage on the surface is then everywhere uniform, as diffusion occurs infinitely fast relative to sorption to smooth out any irregularities. And the ORR rate is then controlled by sorption. The impedance response in this limit appears capacitive, with a semicircular Nyquist plot. When the utilization length is on the same scale as the electrode dimensions, $l_\delta \backsim R_e$, an intermediate case appears; this is identified graphically in the Nyquist plot by the 45° line in the high-frequency limit characteristic of the Gerischer response, along with a semicircular tail at lower frequencies. In fact, the high-frequency region of the Nyquist plot will always rise from the real axis at 45° for the ideal system, but the transition between "Gerischer" and semicircular shapes is more apparent when $l_\delta \backsim R_e$.

The details of the transition between "Gerischer" and "semicircular" shapes are apparent from the Bode phase plot in Figure 2-5b, where, since the real offset (i.e. $R_{ct} + R_{ysz}$) has been zeroed, the angle seen in the Nyquist plot is visible exactly. Impedance spectra which will appear semicircular display a phase angle of magnitude greater than 45°. As l_δ is increased, more and more of the higher frequencies fall along the 45° line. For $l_\delta \gg R_e$, the phase plot displays an angle $\leq 45°$ everywhere. Further, the corner frequency in the phase plot begins to shift slowly upward again, perhaps asymptotically.

Some properties, like the lower corner frequency in the Bode plots, are expected to be independent of R_e. The figure does not show the spread in the high-frequency real-axis intercept in the Nyquist plots; this is to help reinforce an understanding of the effect of utilization length on the overall spectrum shape. Also, the ohmic resistance through the electrolyte, R_{ysz}, changes with R_e in a nontrivial fashion, and so we are not in a position to understand scaling of the high-frequency intercept with electrode radius given the work presented so far.

It should be noted that the electrochemistry at the Pt-YSZ interface has been

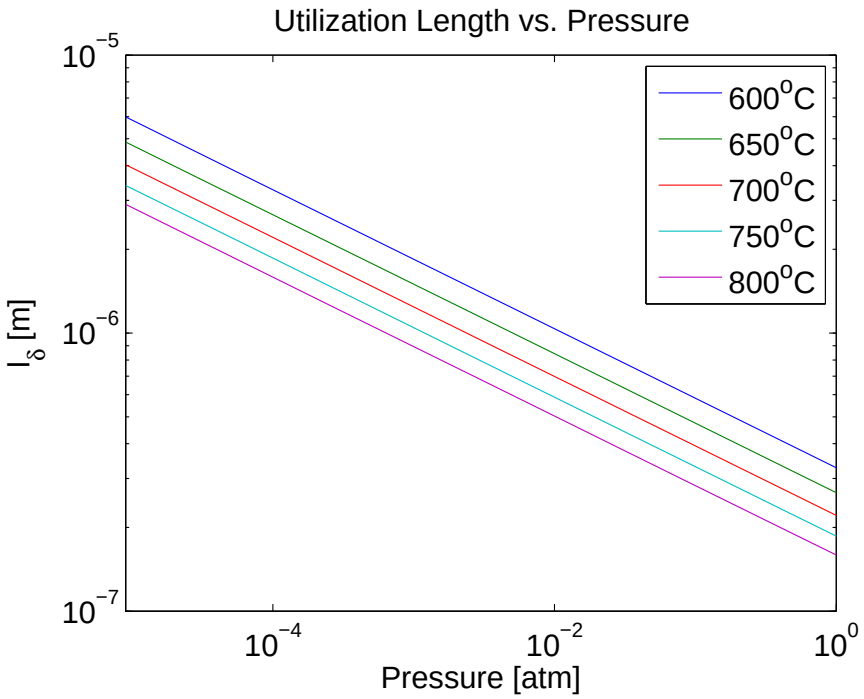

Figure 2-6: Utilization length determined from theory. Binding and interaction energies as well as sticking coefficients found from [56]; vibrational frequencies for adsorbed oxygen from [48]. Diffusion coefficient parameters from [4]. All parameters are appropriate for the {111} family of surfaces of Pt.

left out of this discussion. The present study, in fact, is not designed to examine the charge transfer steps at the interface, and least of all in the high overpotential regime (this study only examines perturbations about zero overpotential). However, there is a growing body of evidence that in the temperature range from 600℃ to 800℃, sorption and transport are the more important processes [2], so that the simplified picture of charge transfer included in the model may be admissible.

2.4.4 Utilization Length

Having established the meaning and importance of the utilization length, we are now in a position to discuss how it might be determined from the present work. Figure 2-6 displays the utilization length predicted by the theory described above over a number of temperatures and pressures.

Using the expressions for D and α listed above and assuming that the sticking

coefficient, $S = S_0(1-\theta)^2$ [17, 54, 58] (see Appendix F)[13], results in the following relation for the utilization length:

$$l_\delta = \sqrt{\Gamma \frac{D_0 h}{2 S_0 \sqrt{P}} \frac{z_{v,ads}}{\sqrt{z_{v,r,gas}}} \sqrt{\frac{\lambda}{k_B T}}}. \tag{2.40}$$

To first order in βu_0, l_δ does not depend upon interaction energies between adsorbates. It's pressure dependence is $P^{-1/4}$; the dependence on temperature hinges on the relative values of the activation energies for the zero coverage diffusion and sticking coefficients.

For comparison, we can analyze Mitterdorfer and Gauckler's data from [37][14]; this places the utilization length for *polycrystalline* Pt at around 100-200 nm for a temperature of around 730℃, increasing with oxygen partial pressures for P between 10^{-3} and 1 atm. Based on this, Adler estimates the utilization length to typically lie between 50 and 500 nm [2]. The numbers from Figure 2-6 range from 200 nm to 6 μm in the temperature and pressure range of interest, and *decrease* with pressure. It should be noted that the plot reflects properties of the Pt(111) surface, and Mitterdorfer and Gauckler's study analyze polycrystalline Pt. Nevertheless, the differences are dramatic, particularly the opposite trends with pressure.

The fact that the impedance shape depends upon the ratio of R_e/l_δ allows for a simple estimation of l_δ. If a number of spectra have been obtained under identical conditions but for differently-sized electrodes, then l_δ might be determined by finding the electrode size at a given set of experimental conditions at which the impedance transitions from a Gerischer to a finite-length, semicircular shape. Performing this analysis on data from previous studies of square electrodes by Dr. S. Naci Koc[15], we see a much larger utilization lengths, with l_δ between 10 and 200 μm, and *increasing* with oxygen partial pressure[16]. Figure 2-7 demonstrates this crossover for

[13]Hopster et al. suggest a more complicated $S(\theta) \propto \exp -A\frac{\theta^{3/2}}{k_B T}$ dependence, though their view is not popular in the literature

[14]Appendix Section C.10 shows that, using the Langmuir isotherm from [37], $\alpha = 2\Gamma\sqrt{k_a k_d P}$, where k_a and k_d are the adsorption and desorption kinetic rate constants.

[15]formerly a member of the Electrochemical Energy Laboratory, now an associate professor at Istanbul University

[16]To get an idea of why the same general characteristics of the impedance spectra are shared by

the temperature of 700℃ and an oxygen partial pressures of 10^{-5} and 1 atm, and shows an increase in utilization length from the lower to the higher partial pressure. Continuing this analysis on the data set also suggests that utilization length falls with increasing temperature, as predicted by the theoretical picture above. However, the temperature dependence from the data set seems stronger than than predicted from theory (l_δ falls by a factor of 3 to 6 in the dataset at various pressures between 800 and 600℃, whereas theory would suggest a dropoff by a factor of only 2 to 3).

Technological Impact Revisited: Catalyst Design and the Utilization Length

For $l_\delta \gg R_e$, the impedance response is no longer dependent upon electrode size; the "active" region of the electrode which participates in capturing and funneling oxygen to the triple phase boundary is smaller than the electrode, itself. This suggests a design principal: for catalysts that are not mixed conductors, no point on the catalyst should be more than two to three utilization lengths from the triple phase boundary. Any other catalyst surface area beyond the active region is effectively "dead weight" and could be better utilized as a thin extension of the electrode, or as a separate electrode. The idea that an electronically (but not ionically) conductive catalyst is more effective with a longer triple phase boundary was established at least as early as the 1920s [2]; the concept of the utilization length gives an idea of the extension of useful catalyst away from the triple phase boundary, and puts an upper bound on catalyst width to accompany the design imperative of maximizing triple phase boundary length[17].

---

the square and circular electrode geometries, visit Appendix C.

[17]The utilization length does not provide an idea for the length scale of activities specific to the triple phase boundary, itself (charge transfer, incorporation). The width of the triple phase boundary was assumed by Mitterdorfer and Gauckler to be 10 nm [37]. Bright regions around the Pt-YSZ TPB in secondary ion mass spectrometry images are between 4 and 5 μm wide [23]. For the purposes of this paper, the triple phase boundary is assumed to constitute a boundary line, and has no width; the electrode dimensions pertaining to the experiments described in the next chapter are sufficiently larger than either of these estimates of TPB extension to bear out this simplification.

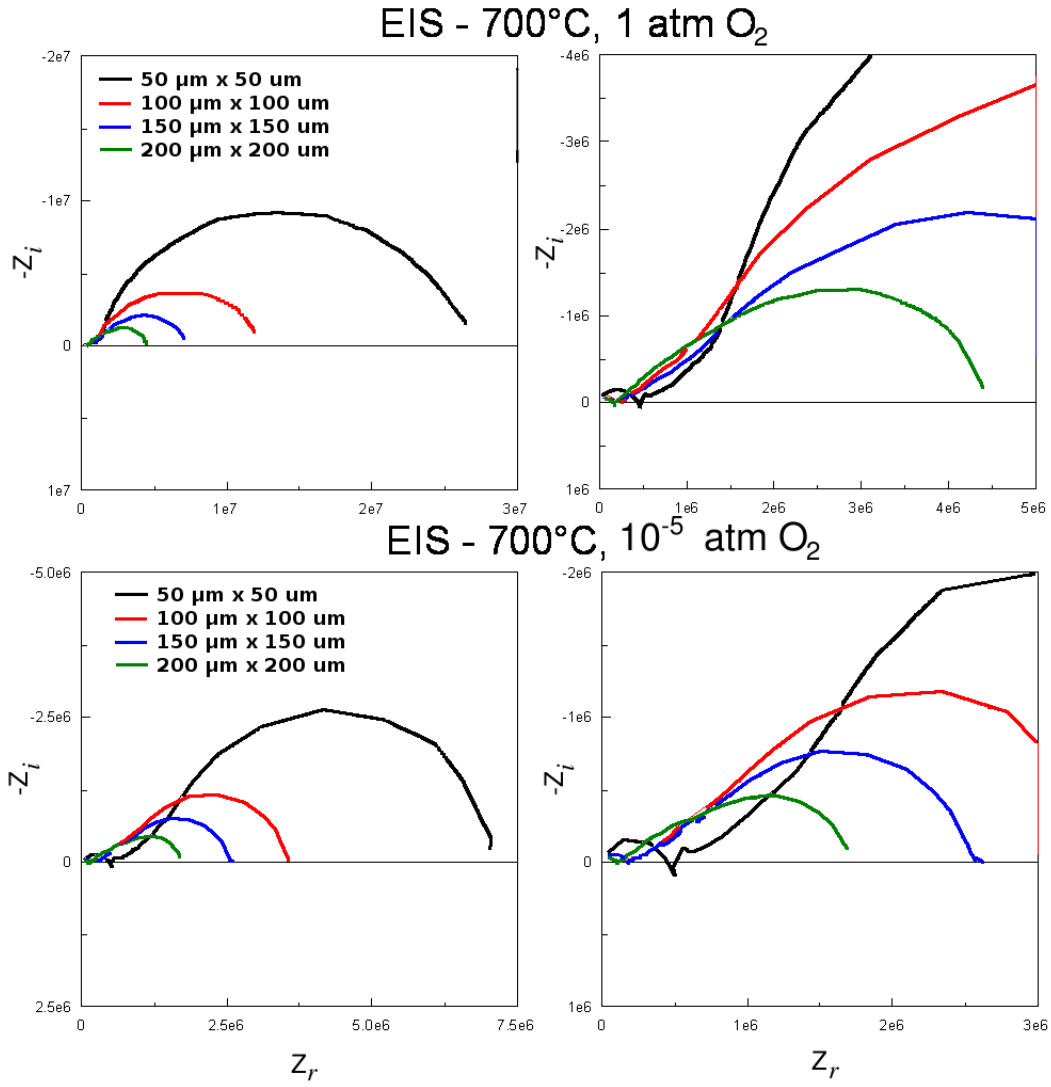

Figure 2-7: Data obtained by Dr. Serkan Naci Koc using square-shaped thin-film Pt electrodes and a long in-plane counterelectrode. The Pt is deposited on top of a thin-film of polycrystalline YSZ ($\backsim$200 nm thick). Top spectra were measured at 700°C at an oxygen partial pressure of 1 atm; bottom spectra at 700°C and $P = 10^{-5}$ atm. Right spectra show blow-up of high-frequency region. Used with Dr. Koc's permission.

2.5 Assumptions

A number of simplifying assumptions are employed in this model. In particular, it is assumed that

1. there is only one species on the surface,
2. the coverage variation during EIS is a small perturbation about the steady-state value,
3. all parameters (including diffusion coefficient) may be evaluated at the steady-state value,
4. the charge transfer and incorporation of oxygen ions into the electrolyte is a single-step process well-described by the reaction in 2.14.

In the following, the validity of these assumptions is discussed. The scale of coverage variations is left to the next chapter, where the experimental capabilities are introduced. The single-step charge transfer reaction is treated in Section 2.6.1.

2.5.1 One Species on Surface

A number of studies show that molecular-precursor-mediated adsorption is an important pathway to oxygen dissociation on Pt [14, 17, 18, 54]. The first assumption does not necessarily conflict with this view; rather, it pertains to a certain limit where dissociation proceeds so rapidly that no physisorbed or chemisorbed [14] molecular oxygen precursors stay on the surface long enough to interfere with further adsorption. As such, only monatomic oxygen sits on the surface. The existence of this limit is verified in experimental studies [17, 18, 54] and employed in theoretical work [25]. It is conceivable that multiple monatomic oxygen species may develop, differentiated perhaps by charge state [2], especially when comparing adsorbed oxygen upon different Pt surfaces. However, for polycrystalline Pt, the multiplicity of grains should provide for a single average surface species to be sufficiently representative of all possible configurations.

2.5.2 Evaluating Parameters at Steady-State Coverage

In Section 2.2.1, basic theoretical calculations of D suggested that D varies rapidly over a narrow transition between lower and middle to high coverage; this may be visualized from Figure 2-2. Mitterdorfer and Gauckler's EIS study for ORR on Pt-YSZ also suggested very strong dependence of D on θ for $\theta <\backsim 0.25$, where D falls almost an order of magnitude with increasing coverage. The same behavior is seen in the study by von Oertzen et al.[53] The relevant question here is whether the diffusion coefficient may be safely approximated at a single value for the coverage fluctuations induced by the EIS experiment. If coverage fluctuations are as large as the upper bound listed in Section 3.5, then most likely the single-valued estimate for D will be inaccurate for coverages lower than 0.25. This means that D will vary appreciably both with position and time, resulting in distortions in the current waveform from the fundamental frequency, as well as errors in physical parameter estimates.

2.6 Major Shortcomings of the Model

The basic physical processes described above are standard in the literature for non-mixed-conductor electrodes in general, and the Pt-YSZ system in particular [2, 36, 39], and are generally able to provide qualitative insight into understanding electrochemical spectra for Pt-YSZ. Despite this, there are several weaknesses in the scheme used to transcribe the qualitative physical description to a quantitative model. And from the opposite perspective, it is also possible that the correct impedance relation was derived from an incorrect physical understanding. In the following, some of the potential difficulties with the model scheme are discussed.

2.6.1 Single-step charge transfer

Charge transfer is treated here in 2.14. This scheme assumes a single-step charge-transfer process whereby oxygen picks up additional charge while it is simultaneously incorporated into the electrolyte. It is doubtful that this process truly occurs in one

step, but the actual kinetics of the process are not well understood [2, p. 4802]. Allowing that the one-step approach is valid for an individual set of experimental conditions, it is conceivable that the charge-transfer process which is rate-limiting at one state may be different from that which is limiting at another state.

Having chosen to focus on the electrode surface rather than the electrode-electrolyte interface, we are allowed some latitude in the specific charge-transfer processes so long as the one-step approach is still admissible. In this case, we look to the connection between the surface processes and the interface for potential problems. That connection took the form of equating the flux from Fickian diffusion with that that constituting current into the YSZ. Suppose that some of the oxygen does not enter the electrolyte at the boundary, but spills onto the electrolyte surface, forming an oxygen reservoir. Such a situation would appear as a capacitive contribution to the electrochemical impedance. Perhaps this reservoir is drained at higher overpotentials than that at the YSZ boundary, contributing to nonlinearities in the I-V relationship. While this conjecture may not be accurate, other activities at the electrode-electrolyte interface and surrounding area, especially relating to the electrolyte, may cause deviations from the picture presented previously.

2.6.2 Oxide formation

At the high temperatures of these experiments, we should expect some subsurface oxide formation on the Pt [17, 18, 54]. Because the model employed here is not material-specific, but process-specific, oxide formation only presents a problem if the three physical processes employed in the model, as well as the assumptions upon which the model is built, do not effectively describe the oxygen reduction reaction on the oxide. However, if oxide formation proceeds *during* experimental runs, it contributes to nonstationarity in physical the properties of the system. In this case, comparisons between different spectra or with literature data for Pt and YSZ lose their meaning. Further, oxidation might constitute a parallel distributed reaction on the surface, operating in tandem with sorption. This would contribute anomalous features to the spectra not anticipated by the models given above.

2.6.3 Nonuniformity of Surface

It is a fundamental assumption of this model that, at equilibrium, the Pt surface is everywhere uniform, so that the same surface properties and coverage exists everywhere. There are several reasons why this is may not be true. Firstly, it is conceivable that temperature and pressure may vary over the surface of the electrode; indeed, measurements of temperature via a thermocouple along a surface in the experimental setup indicate fluctuations in the mean temperature of as much as 20°C over the 0.5 cm × 0.5 cm area of a sample YSZ slab (much larger than the area of a single microelectrode), and 10 to 15 degree temperature swings at a single location over time.

Another factor contributing to nonuniformity is the fact that the Pt surface presents many different types of adsorption sites. Indeed, even a single crystal facet may present different adsorption sites [14, 53]; the presence of these multiple site varieties has important consequences regarding sorption and diffusion [50, 53]. Similarly, the presence of steps and defects on the surface also results in significant changes in surface properties [17, 20]. These issues may, in fact, be somewhat mitigated if a polycrystalline surface is used in view of the idea that this surface might effectively randomize all of the defects and nonuniformities on a scale sufficiently smaller than the microns to tens and hundreds of microns of interest here. On the other hand, processing nonuniformities may exceed this scale boundary and again render inaccurate the uniformity assumptions (see the next chapter for a discussion on the processing used in microelectrode fabrication).

2.6.4 Alternative Explanations

Other pathways may be envisioned for the ORR. For example, we might imagine that oxygen adsorbs and diffuses along the exposed solid electrolyte surface rather than the Pt electrode, while still undergoing charge transfer and incorporation at the triple phase boundary interface. Another scheme might involve oxygen travelling inward from the TPB along the interfacial area between the Pt and YSZ. In this case,

charge transfer is now a distributed reaction across the interfacial area and sorption at the TPB constitutes a boundary condition on oxygen coverage[18], where before, sorption was taken to be the distributed reaction with charge transfer and incorporation imposing a boundary condition. Because these alternative explanations still propose similar generic mechanisms - a distributed reaction, transport by diffusion, and a single-step reaction at the boundary - they may result in the same generic forms of impedance relations. How, then, might we identify one model from the other as correct?

The question is resolved to some degree by noting that we have the ability to predict trends in the impedance spectra with temperature, pressure, electrode geometry, and so forth. These trends vary from model to model. For example, Section C.9 demonstrates that the lower corner frequency from the impedance in 2.29 is closely tied to the distributed reaction in the model. If this distributed reaction is sorption, as assumed in the original derivation of 2.29, then the corner frequency ought to depend on pressure, and be fairly independent of the electrode-electrolyte interface properties. By contrast, if the distributed reaction is charge transfer and incorporation, the opposite should be true: the corner frequency should depend primarily on the properties of the interface and not on pressure.

Further, it is the hope of this study that the spectra may be collected so as to extract model parameters with quantitative accuracy; these may then be compared with literature values.

However, there will always be some uncertainty associated with the interpretation of EIS spectra, as these spectra are indirect means of probing the myriad physical processes which control them.

[18] *Distributed reaction* refers to a reaction taking place over the entire problem domain, whether this domain constitutes the electrode surface or the electrode-electrolyte interfacial area, or perhaps the electrode bulk for the case of mixed conductors.

Chapter 3

Procedure

3.1 Introduction

This chapter outlines the steps involved in setting up and performing the experiments and analyzing the resulting data. It first reviews the method and equipment used to fabricate the microelectrodes, and then discusses the apparatus for obtaining EIS data at various temperatures and pressures. Finally, a discussion is included which clarifies how the impedance expressions found in Chapter 2 might be used to extract physical parameters from the measured impedance spectra.

3.2 Fabricating Electrodes

Figure 3-2 outlines microelectrode fabrication visually. The first step in the process is to define the geometry. In this work, we select a circular geometry for each electrode, with radii of 12.5, 25, 50, 100, and 200 μm. Microelectrodes must be adequately spaced so as to avoid spurious data due to coupling between the microelectrodes (e.g. electromagnetic coupling, unwanted participation of neighboring microelectrodes, etc.). Toward this end, a design rule is implemented that no two electrodes are closer to one another than three of the larger of the two diameters. Using multiple radii helps to identify the pathway of oxygen reduction - whether the oxygen adsorbs onto the electrode and travels across its surface or through its bulk.

Since Pt is not an oxygen ion conductor, and since the Pt electrodes here are dense and not porous, we might expect a scaling of low- or high-frequency conductance with the *perimeter* of the electrode, which should be exactly the *triple phase boundary length*, ℓ, at which charge transfer occurs. However, the actual dependence of the high-frequency conductance, a quantity dominated by ohmic transport through the YSZ, is complicated even in the cylindrical geometry used here (see Section 2.4.3). Also, as discussed in Section 2.4.3, the scaling behavior of the low-frequency intercept - the limiting (real) impedance as $\omega \to 0$ - transitions between between R_e^{-1} and R_e^{-2} as R_e/l_δ is modified from $\gg 1$ to $\ll 1$. This transition is witnessed in Figure 2-5. Nonetheless, impedance ought always to decrease, and conductance to increase, as the electrode radius is increased, all else equal. As such, a basic test of the theoretical framework employed here is to verify this scaling behavior in the low- and high-frequency intercepts of the EIS spectra; this analysis is performed in Section 4.2. In addition, we have seen in Chapter 2 that, by reducing the electrode scale length to the size of the *utilization length*, l_δ, finite-length effects become apparent. This is advantageous in analysis as (a) it provides a crude way to estimate the utilization length via observing at what radius finite length effects appear, and (b) improving identifiability of model parameters. Previous unpublished work performed in this laboratory on square, dense Pt electrodes over YSZ begin to show finite-length behavior for electrode dimensions between 10 and 100 μm; this has motivated the selection of microelectrode radii listed above.

The design is drafted via Computer Aided Design (CAD) software package (e.g. SolidWorks, etc.); Figure 3-1 shows this actual CAD image created from this process.

The electrodes' substrate plays the role of electrolyte. For this task, we use 8%-molar single-crystal (100) yttria-stabilized zirconia (YSZ) wafers (MTI Corp., Richmond, CA)[1]. Ohmic ion conduction through the YSZ electrolyte will register as a

[1]Yttria-stabilized zirconia refers to cubic zirconia, ZrO_2, (the high-temperature form of the oxide crystal and popular diamond simulant) which is stabilized at room temperature by the addition of another oxide, yttria (Y_2O_3). The molar percentage given refers to the degree to which the zirconia is doped by the yttria, and the crystalline plane is that which is exposed on the surface of the substrate. YSZ is an oxygen ion conductor, and so it is a key element in many solid oxide fuel cells as the (solid) electrolyte [26].

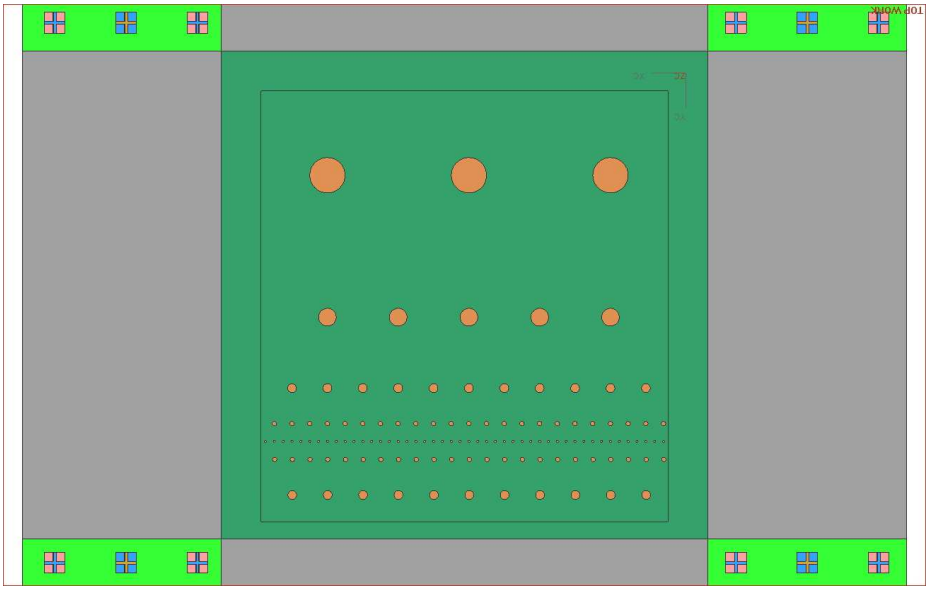

Figure 3-1: Geometry of microelectrodes. The largest microelectrodes are 200 μm in radius, the smallest are 12.5 μm, and the cell size is 0.5 cm $\times$ 0.5 cm. Design drafted in SolidWorks by Ethan Crumlin, Electrochemical Energy Laboratory, MIT.

component of the electrochemical impedance spectra. Calculating this contribution from theory is a challenging but solvable problem (in the author's opinion); however, it will be left to future studies. Instead, we will employ the approximation that the ohmic contribution to impedance is frequency-independent[2], and focus attention upon the frequency-dependent component of each electrochemical impedance spectrum. By obtaining spectra from several YSZ substrates of different thicknesses, we may gauge the accuracy of this assumption. It might also be possible to attempt to capture the dependence of the ohmic electrolyte resistance on the electrode radius, R_e, and YSZ thickness, t, beyond the $t/\sigma\pi R_e^2$ estimate; however, this investigation is not carried out in this work. We use three YSZ thicknesses: 250 (260), 500 (520), and 1000 (1040) μm (the numbers in parentheses are averages of three thickness measurements taken with a micrometer at different locations of the slab).

Before patterning the microelectrodes onto the substrate, the counterelectrode is

[2]valid for low-frequencies for which the YSZ may be envisioned as a good conductor, where the skin depth, $\delta = 1/\sqrt{\pi f \mu \sigma}$, is much larger than the flow dimensions, with f as the signal frequency, μ the magnetic permeability ($\approx \mu_0$), and σ the ion conductivity [52]. A quick estimate at the highest experimental frequency of 20 kHz using properties of YSZ gives $\delta \approx 10$ m, much bigger than the system dimensions.

created. Here, we desire a counterelectrode that constitutes a uniform ground plane on the underside of the YSZ substrates so that the oxygen ion flow-path is through the plane of the substrate. This maintains cylindrical symmetry for each electrode. At the same time, the counterelectrode's contribution to the impedance spectrum must be distinguishable or negligible so that the impedance properties of the patterned electrodes may be ascertained. To realize these goals, the YSZ slab undersides are first brushed with a Pt ink (66.4% Pt in terpineol matrix, BASF Part. No. 6082, BASF Catalysts, NJ) as uniformly as possible. Finally, the ink is set via firing at 1100℃ for 60 min. We have seen in Chapter 2 that electrochemical impedance scales inversely as the triple-phase boundary length; the microporous structure effectively creates a very large TPB length, resulting in low impedance. Finally, after casting the microelectrode geometry from a digitized form into a real mask for photolithography (Advance Reproductions Corp., North Andover, MA), microelectrodes are fabricated on top of the YSZ substrates by

1. spin coating negative photoresist (Clariant, Switzerland) upon the substrate,

2. exposing under a mask patterned with the desired geometry,

3. developing the resist,

4. sputtering Pt on top of the developed resist at 100 W for twenty minutes in a pure argon atmosphere, and

5. removing excess Pt by photoresist lift-off via dissolution in acetone.

The deposition of Pt electrodes follows the procedure described in [26, 27] regarding the deposition of Pt counterelectrodes.

Before and after experiments, microelectrodes are inspected carefully under an optical microscope (FS70, Mitutoyo, Japan).

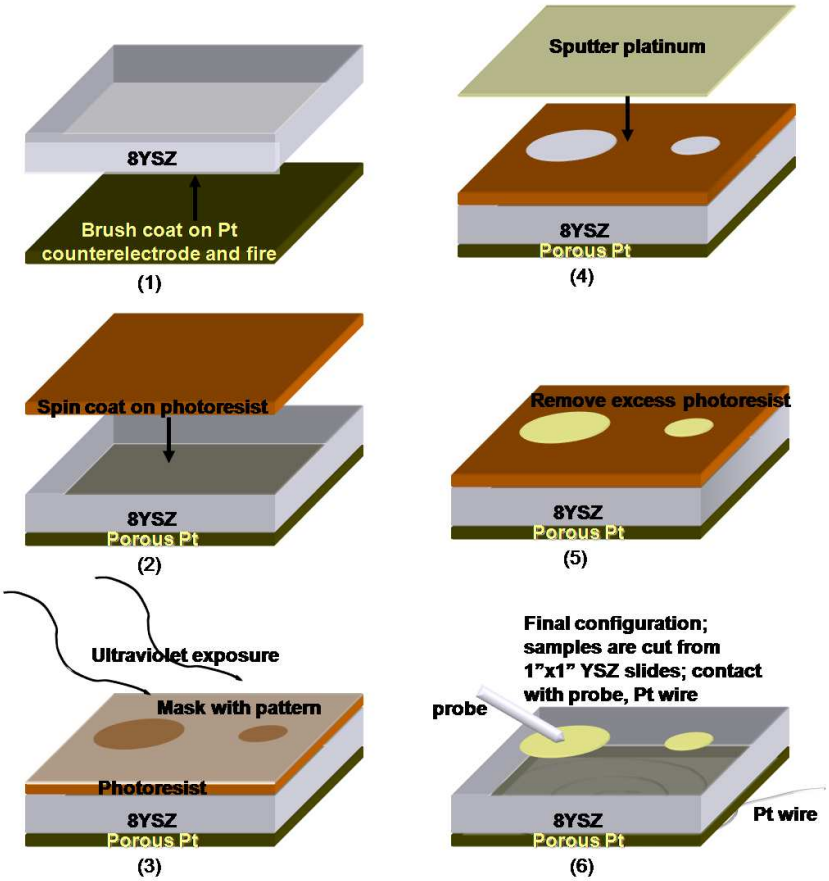

(a)

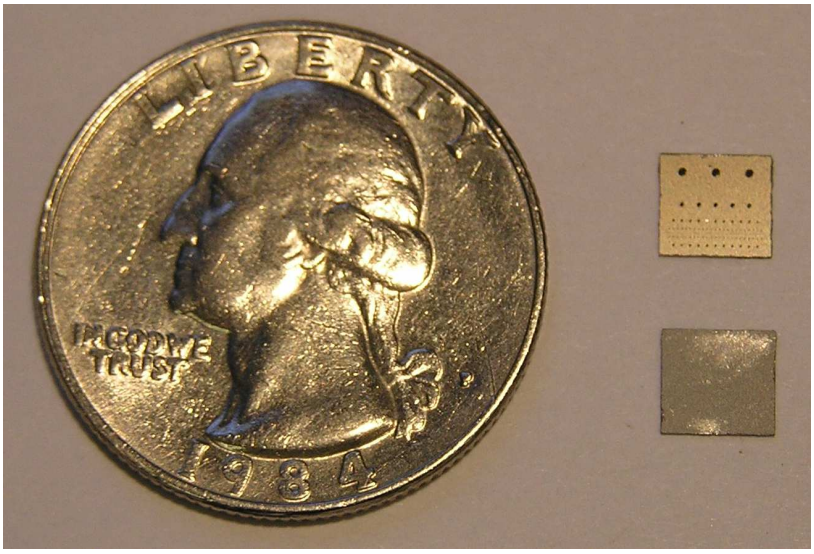

(b)

Figure 3-2: (a) Step-by-step procedure used in microelectrode fabrication. (b) Photograph of a patterned sample and porous Pt counterelectrode on the sample underside next to a US quarter. YSZ single-crystal thickness is about 0.26 mm.

3.3 Obtaining EIS Data

EIS spectra must be obtained in situ, as the test platforms must rest in environments with controlled temperature and O_2 partial pressure. The experimental apparatus used for carrying out these measurements in this study is the SUSS MicroTec PM5 150 mm Manual Probe System. The setup is as follows: test samples are placed within a small, temperature-controlled furnace (manufactured by Linkam with TMS94 controller); this sits inside a water-cooled, enclosed (but not air-tight), glass-topped chamber. Temperature gradients exist within the furnace; as such, temperature control is calibrated independently via a small thermocouple. Oxygen pressure control is achieved by pumping into this chamber a continuous flow of gas at fixed oxygen-argon mixes, displacing atmospheric air in the chamber. One additional set of data points can be taken from exposing the electrodes to atmospheric air. The electrodes and counterelectrode are contacted by Pt-coated tungsten microprobes (needles with tip radii of 0.6 μm when undamaged) which penetrate through the enclosure via small holes; the flowed oxygen-argon mixes escape through these holes, keeping the chamber's total pressure at approximately 1 atm. The roof of the chamber is a transparent glass and allows visual inspection and alignment with the help of the Mitutoyo FS70 optical microscope included in the PM5 Probe System. The probes are then positioned manually via SUSS PH150 High-Resolution Manual Probehead™ manipulators. Once connectivity is established, EIS spectra are obtained using a Solartron Sl 1260 Impedance/Gain-Phase Analyzer in conjunction with a Solartron 1296 Dielectric Interface, the latter of which makes possible measurements of very high impedance (>100 TΩ) and at very low currents (1 fA) [46]. To ensure consistency, multiple spectra are taken regularly for individual temperature and pressure points (thermodynamic states).

Figure 3-3 shows a probe contacting a 200 μm-radius electrode. There is an additional probe tip visible in the micrograph; this is used only to pin the sample in place.

Spectra are obtained at four decades of pressure, visiting oxygen contents both

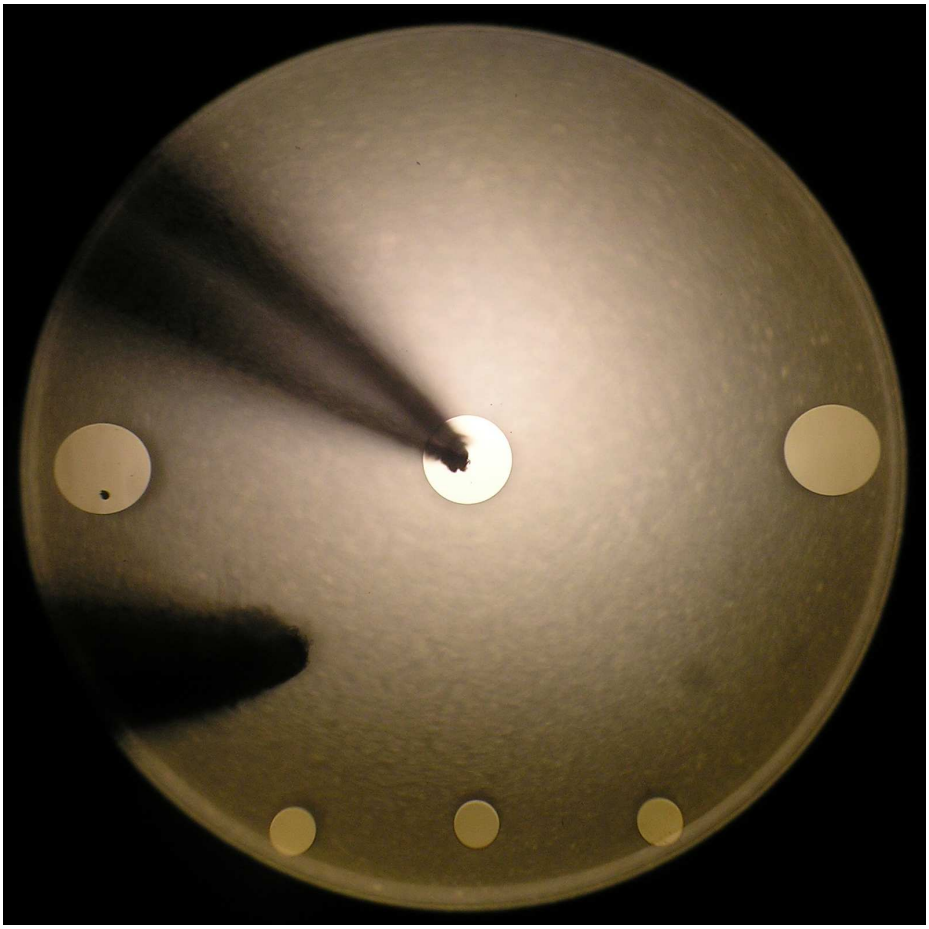

Figure 3-3: Optical micrograph of a probe contacting a 200 μm-diameter microelectrode. A second probe tip is visible underneath; it is used to help stabilize the sample.

above and below that at atmospheric conditions, and at roughly 50°C-increments between 475°C and 700°C. Lewis and Gomer find that 500°C marks the onset of a faster diffusion regime of O on Pt [30]; not surprisingly, impedance spectra at lower temperatures must probe at lower frequencies to capture the slower time scales of physical processes, requiring measurement times of several hours for each spectrum. Further, the higher temperatures are of more technological relevance: 650°C remains an ambitious and much-sought-after goal for SOFC technology, where operating temperatures are routinely at 800°C [26].

Frequencies are sampled between 1 mHz and 1 MHz with five data points per decade. Previous studies in EEL using square electrodes have shown that frequencies of interest for determining Faradaic processes are typically well below 10 kHz

for given materials and geometries; however, the higher frequencies are useful in separating other simultaneous processes from the data, including double-layer effects [5]. Measurements may be made by specifying a fixed number of cycles over which impedance points are integrated, or by specifying a fixed integration time. Bias errors may be reduced by integrating over multiples of the excitation period, but a fixed integration time allows for an averaging of wide-spectrum random noise that is uniform for all data points. I generally prefer the former method to avoid bias, but the latter is also effective. Measurement errors are gauged experimentally by repeated EIS measurement at a single temperature and pressure; however, a more complete, if less detailed, error estimate is provided in the Solartron literature for the 1296 analyzer, and suggests impedance errors on the order of one degree in phase and one percent in magnitude [45, 47].

3.4 Data Fitting Procedures

3.4.1 Total Impedance and Unique Parameters

The impedance expression for polar (cylindrical) geometry is (see Appendix C and Equation 2.29)

$$Z_{cyl} = R_{ct}\left[1 + \frac{\frac{\partial I}{\partial \theta}}{nq_e\Gamma\ell\sqrt{D(j\omega+\alpha)}}\frac{\mathrm{M}_0\left(R_e/\xi\right)}{\mathrm{M}_1\left(R_e/\xi\right)}\right]. \tag{3.1}$$

However, there are other contributions to impedance besides the Faradaic sources described in this equation. Certainly, there will be an ohmic contribution from ionic conduction through the electrolyte, as well as capacitive contributions resulting from the Pt/YSZ interface and electrode-counterelectrode coupling. Further, some of the model parameters are not uniquely identifiable from a single EIS spectrum because they are mixed together in products.

Figure 3-4 shows a more realistic circuit diagram useful for fitting; the shaded boxed component is the Faradaic (cylindrical) impedance. This particular circuit

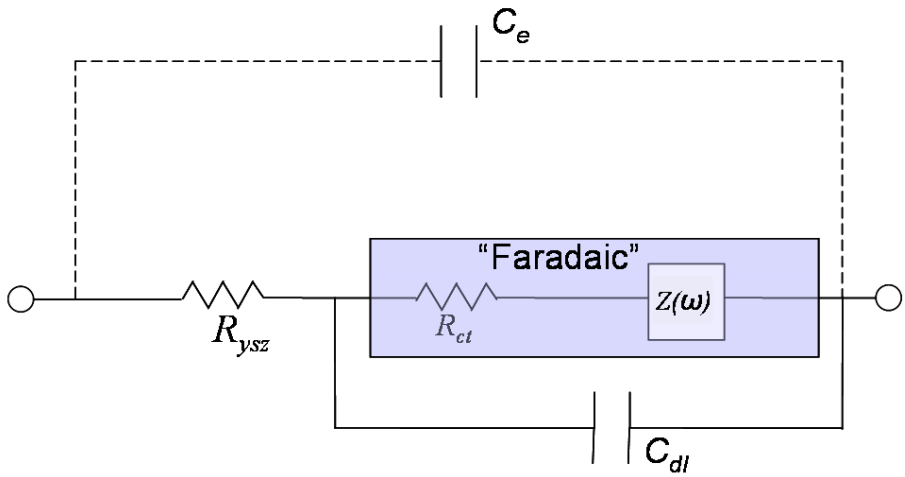

Figure 3-4: Randles circuit capturing major contributions to total impedance. R_{ysz} is the ohmic impedance of the YSZ electrolyte; C_{dl} is a parallel capacitance often attributed to the double layer, and $R_{ct} + Z(\omega)$ is the Faradaic capacitance (e.g. Z_{cyl}). The dashed lines are not part of the typical Randles circuit; they show the additional capacitance due to electromagnetic coupling between the electrode and counterelectrode.

topology is known as a *Randles circuit* and is commonly employed in electrochemical fitting analysis (see [2, p. 4797-8] and [34, p. 74], for example). In order to properly extract the Faradaic impedance, Z_F, from an impedance spectrum, the ohmic electrolyte resistance, R_{ysz}, and the double layer (and electronic) capacitance must be known. Methods exist for extracting each of these parameters from one or multiple spectra [5, e.g. for C_{dl}]. Further, R_{ysz} may be calculated numerically (and perhaps analytically) using known YSZ ionic conductivity[3].

By careful experimental design, the capacitive contribution to the impedance may be minimized. The value for the specific double layer capacitance for the Pt/YSZ interface is 10^{-6}-10^{-5} F/cm^2 [2, 37]. The maximum proposed electrode radius is 200 μm, corresponding to an area of 1.26×10^{-3} cm^2. This gives a maximum double layer capacitance of around 1×10^{-8} F. At the 20 kHz upper bound of the frequency band most important for data analysis[4], this results in an imaginary impedance of approximately $Z_c = 1/(j\omega C) \approx -j630\Omega$. However, the smallest electrodes, with

[3]The boundary conditions in this mixed-conductor problem are an interesting topic by themselves.

[4]Previous studies in EEL with similar configurations have shown that Faradaic effects are well-characterized by frequencies below this limit - see previous discussion on frequency range.

radius 12.5 μm (200/16), have area $\backsim 5 \times 10^{-6}$ cm^2, so that the capacitive impedance at 20 kHz would be 16^2 times larger, or $\backsim$ 160 kΩ, likely large enough to be neglected.[5]

The electronic capacitance should be smaller than the double layer capacitance - if the dielectric constant $\epsilon_r \approx 10$ for ceramic YSZ [6], then for a 100 μm-thick YSZ wafer, the electronic capacitance might be estimated as $C_{specific} = 10 \times 8.85 \times 10^{-12}$ F/m /(10^{-4}m) $\approx 10^{-10}$ F/cm^2. Since the electromagnetic displacement current offers an alternate pathway between electrode and counterelectrode than ionic conduction through the YSZ, electronic capacitance appears in parallel to the empirical Randles configuration in Figure 3-4. However, because it is very small, it is not expected to appear prominently in impedance spectra except at very high frequencies (as, perhaps, a small, high-frequency semicircle appended to the tip of the spectrum).

For the moment, it is an open question as to whether capacitive impedance is small enough to participate in the parallel combination shown in Figure 3-4. However, it would appear that larger electrodes may display a capacitive character in their impedance spectra, while the very smallest electrodes may be less affected.

The total impedance, Z_t, might be captured in terms a set of fit parameters, $\boldsymbol{\gamma}$, uniquely identifiable by fitting to a single EIS spectrum as

$$\begin{aligned} Z_t &= R_{ysz} + \frac{Z_F}{Z_F(j\omega C_{dl}) + 1} \\ Z_F &= \gamma_1 + \frac{\gamma_2}{\sqrt{j\omega + \gamma_3}} \frac{\mathrm{M}_0\left(\gamma_4\sqrt{j\omega + \gamma_3}\right)}{\mathrm{M}_1\left(\gamma_4\sqrt{j\omega + \gamma_3}\right)}. \end{aligned} \tag{3.2}$$

The correspondence between the fit parameters, $\boldsymbol{\gamma}$, and the model parameters is as

[5]Faradaic conductance scales with triple phase boundary length, and therefore electrode radius, as opposed to double layer capacitance, which scales with the Pt/YSZ interfacial area as the square of the radius.

[6]This is a conservative estimate; in reality, the relative permittivity is perhaps around half this value.

follows:

$$\begin{aligned}
\gamma_1 &= R_{ct} = \left[nq_e\ell\Gamma\left(b_{-1}k_{-1}\mathrm{O}_{\mathrm{O}}^{\times}\left(1-\bar{\theta}\right) - b_1k_1\mathrm{V}_{\ddot{\mathrm{O}}}\bar{\theta}\right)\right]^{-1} \\
\gamma_2 &= R_{ct}\frac{\partial I/\partial\theta}{nq_e\Gamma\ell\sqrt{D}} = R_{ct}\frac{k_1\mathrm{V}_{\ddot{\mathrm{O}}} + k_{-1}\mathrm{O}_{\mathrm{O}}^{\times}}{\sqrt{D}} \approx \frac{1}{nq_e\ell\Gamma\frac{q_e}{k_BT}\bar{\theta}(1-\bar{\theta})\sqrt{D}} \\
\gamma_3 &= \alpha = S(\bar{\theta},T)\left[a_s\frac{\lambda}{h}\left(\frac{\partial\theta}{\partial P}\right)^{-1}\right] \\
\gamma_4 &= \frac{R_e}{\sqrt{D}}
\end{aligned} \tag{3.3}$$

R_{ysz} is the ohmic resistance of the YSZ electrolyte - it is typically taken from high-frequency impedance data as the limiting impedance. The expression for γ_3 is explained in Section C.11 in the appendix and will be discussed below. The diffusion coefficient, D, has been included in two separate fit parameters in anticipation of the limit where $\mathrm{M}_0\left(\gamma_4\sqrt{j\omega+\gamma_3}\right)/\mathrm{M}_1\left(\gamma_4\sqrt{j\omega+\gamma_3}\right) \to 1$, which ought to occur for the larger electrode radii for which the impedance expression approaches that of the Gerischer form seen in Equation C.38. In this particular regime, identification of D becomes challenging; however, because the diffusion coefficient is, at this scale, a property of the surface and not of the electrode radius, the parameter might be bootstrapped from calculations done with the smaller radii, for which the sensitivity for γ_4 should be greater.

3.4.2 Fitting Procedure

The problem of fitting parameters of a curve to data ultimately reduces to one of minimization. There are multiple ways of approaching this task; they are often distinguished by the scheme used to map the vector quantity of residuals to a scalar norm. The problem is then to minimize this norm. Classic methods involve minimizing residuals in a least-squares sense. From the perspective of fitting a curve to data, it becomes important to be sensitive to errors in measurement. One way to accomplish this is through the chi-square minimization [43]. Define $\mathrm{G}(\mathbf{x};\boldsymbol{\gamma})$ to be a function of the n-component vector, $\mathbf{x}$, which defines the "input" at each data point,

but parameterized by the k-component vector, $\boldsymbol{\gamma}$, with $k < n$. Next, let $\mathbf{y}$ be the vector of data points, and $\mathbf{w} = \{w_1 \cdots w_n\} = \{1/\sigma_1^2 \cdots 1/\sigma_n^2\}$ be the vector of inverse variances corresponding to measurement errors at each of the n data points. Then the goal of the minimization is to pick the elements of $\boldsymbol{\gamma}$ such that $\mathrm{G}(\mathbf{x};\boldsymbol{\gamma})$ approaches $\mathbf{y}$ as closely as possible. The chi-square scheme defines "as closely as possible" in the following way: choose $\boldsymbol{\gamma} = \{\gamma_1, \gamma_2, \cdots, \gamma_k\}$ such that χ^2 is minimized, where

$$\chi^2 \equiv \sum_{\nu=1}^{n} w_\nu \left[y_\nu - \mathrm{G}(\mathbf{x};\boldsymbol{\gamma})\right]^2 \tag{3.4}$$

The particular $\boldsymbol{\gamma}$ for which this condition is satisfied is denoted by $\boldsymbol{\gamma}^*$.

It is natural to try to find $\boldsymbol{\gamma}^*$ by solving the k-component vector equation,

$$\frac{\partial \chi^2}{\partial \gamma_i} = 0, \tag{3.5}$$

i from 1 to k. However, the requirement that $\boldsymbol{\gamma}^*$ be at a global minimum does not make such a problem definition general (i.e. it does not pick out global minima from local minima, nor does it ensure that the critical point found is, indeed, a minimum, nor does it determine minima at domain boundaries). Nonetheless, it is a useful starting point, and one that will be employed herein.

The reader may be familiar with least-squares formalism - that is, choosing the parameters such that the sum of the square of the residuals is minimized. The chi-square scheme introduced here is a kind of least-squares minimization. Its key feature is that the residuals are weighted by the inverse of the variances associated with measurements at each of the n data points. The result is to give preference in fitting the theoretical curve to those data values with the smallest error in measurement. It is important to note that this scheme is based on the assumption that measurements are associated with a normal distribution about the "true" value of the measured quantity - a non-normal distribution requires an alternative setting of the problem [43].

Due to the fact that impedance magnitudes vary by many orders of magnitude

between low and high-frequency data points, the low-frequency, larger-impedance data is given undue weight in the fitting. For this reason, each residual is normalized by the magnitude of the impedance; this normalization is carried out through the σ parameter.

For a single EIS spectrum, $\mathbf{x}$ is identified as the frequencies, ω, sampled. $\mathbf{y}$ is the vector of (complex) impedance measured at each data point. $\mathrm{G}(\mathbf{x};\boldsymbol{\gamma})$ is the parameterized total impedance in 3.2, $Z_t(\omega;\boldsymbol{\gamma})$. Because each impedance measurement is a complex quantity, there are multiple (two) data points corresponding to each y_ν in Equation 3.4. One way to handle these additional data values is to include in the sum of 3.4 one residual for the real part of the impedance and one for the imaginary; this is carried out in the present work.

Determination of $\mathbf{w}$ is possible to some degree via instrumentation documentation [45, 46, 47], where the dependence of uncertainty upon both frequency and impedance magnitude is given. But we will instead approximate variances by taking repeated measurements at a single set of experimental conditions and determining a separate impedance distribution for each sampling frequency.

Further details regarding the fitting procedure are given in D, including expressions for the Jacobian matrix for the Faradaic impedance, a definition and evaluation of the Hessian matrix in the context of error propagation and estimation, and a useful approximation for the ratio of Bessel functions given large arguments.

3.4.3 Extracting the Diffusion Coefficient and Coverage Isotherm

It is the stated goal of this thesis to obtain (a) the diffusion coefficient and (b) a coverage isotherm for this system at a number of thermodynamic states. Provided the ratio of Bessel functions is appreciably greater than unity in Equation 3.2, its presence allows for a straightforward extraction of D as[7] $D = (R_e/\gamma_4)^2$. The coverage is somewhat less accessible, but as discussed in Section 2.3.2, a useful simplification arises by taking the current to be nominally zero for perturbations about equilibrium.

[7] This is an improvement over other studies and is due to the cylindrical geometry employed here - see Appendix C.

In particular,

$$\gamma_2|_{I=0} = \frac{1}{nq_e\ell\Gamma\sqrt{D}\frac{q_e}{k_BT}\bar{\theta}(1-\bar{\theta})} \tag{3.6}$$

so that

$$\bar{\theta} = \frac{1}{2} \pm \sqrt{\frac{1}{4} - \frac{1}{nq_e\ell\Gamma\sqrt{D}\frac{q_e}{k_BT}\gamma_2}} \tag{3.7}$$

Both solutions are admissible since $\bar{\theta}(1-\bar{\theta})$ is symmetric about $\frac{1}{2}$. However, it should be possible to eliminate one based on considerations of pressure, as the coverage should be monotonically increasing with pressure.

But γ_3 provides a second means of estimating the coverage. From Section C.11,

$$\gamma_3 = S(\bar{\theta}, T)\left[a_s\frac{\lambda}{h}\left(\frac{\partial\theta}{\partial P}\right)^{-1}_{T,\bar{\theta}}\right] \tag{3.8}$$

where S is the sticking probability alluded to in the literature of oxygen adsorption over Pt [17, 54, 20, 25], λ is the thermal wavelength, h is Planck's constant, and $a_s = \frac{1}{\Gamma}$ is the area per adsorption site. The quantity, $\frac{\partial\theta}{\partial P}$, might be estimated from the coverage isotherm obtained in Appendix B,

$$\left(\frac{\theta}{1-\theta}e^{\beta u_0\theta}\right)^2 = e^{2\beta\epsilon}\frac{z^2_{v,ads}}{z_{v,r,gas}}\frac{P\lambda^3}{k_BT}, \tag{3.9}$$

as

$$\frac{\partial\theta}{\partial P} = 2e^{2\beta u_0\theta}\frac{\theta(1+\beta u_0(\theta-\theta^2))}{(1-\theta)^3}\frac{\lambda^3}{k_BT}. \tag{3.10}$$

In conjunction with 3.8 and with an approximation of the sticking probability as proportional to the square of the number vacancies $S(\theta, T) \approx S_0(T)(1-\theta)^2$ [54][8], this gives an implicit equation for θ,

$$2\gamma_3\bar{\theta}(1+\beta u_0(\bar{\theta}-\bar{\theta}^2))e^{2\beta u_0\bar{\theta}} = (1-\bar{\theta})^5 S_0 a_s\frac{\lambda}{h}, \tag{3.11}$$

[8] since two vacancies are needed per oxygen molecule adsorption/dissociation event

which might be solved numerically. In fact, computing the derivative directly gives an equivalent expression which is *explicit* in θ,

$$\bar{\theta}^3 - 2\bar{\theta}^2 + \bar{\theta}(1 - \frac{1+A}{\beta u_0}) + \frac{1}{\beta u_0} = 0 \tag{3.12}$$

where

$$A \equiv \frac{\gamma_3}{2S_0 a_s \frac{\lambda}{h} P} \tag{3.13}$$

Data exists in the literature for S [54, 17, 20] and, in an indirect form, for u_0 [49], allowing an estimate for $\bar{\theta}$ from Equation 3.11 which might be compared to that of 3.7. Alternatively, an estimate for $\bar{\theta}$ may be taken from this relation and used in 3.7 to check the value of D against that obtained from γ_4.

The key point of this development is that we *have a means for estimating D and θ from each individual EIS spectrum.* In particular, through the use of $D = (R_e/\gamma_4)^2$ and Equation 3.7, these two important quantities are extracted *without assuming anything with regard to their functional dependence on experimental parameters.* The extracted dependencies may then be independently compared with those expected from theoretical considerations (see Equations B.29 and B.48).

3.5 Small-Scale Fluctuations in Coverage

The formal requirements for the validity of the perturbative limit were recorded in Section 2.2.2. This section begins to address the degree to which these requirements are satisfied for the EIS experiments outlined in this chapter.

To determine the validity of the perturbation assumption in coverage, it is useful to estimate (a) the variation in current and (b) the resultant variation in coverage - we desire a coverage variation on the order of 10^{-2}. The Solartron 1296 dielectric interface, in conjunction with the 1260 frequency analyzer, has a variable voltage amplitude with an output range between 0 and 3 V, and a 1 fA input current resolution. For the present, we'll assume a 1 mV voltage amplitude, $\tilde{v}$, about a zero-voltage mean. In EIS spectra from previous tests with 200 μm square Pt microelectrodes,

the smallest zero-frequency impedance approached 375 kΩ, which appeared at atmospheric pressure and a temperature of 800℃. This corresponds to a normalized current variation of $\tilde{I}/\ell = \tilde{v}/(R\ell) \approx (1\text{mV}/375\text{k}\Omega)/(4 \times 200 \times 10^{-6}\text{m}) = \frac{1}{3} \times 10^{-5}\text{A/m}$, or about 3.3 μA/m. Even for the smallest microelectrodes used in this study, with $\ell = \pi(12.5\mu\text{m}) \approx 40\mu\text{m}$, this results in a current well within the femtoamp tolerance. This represents an oxygen flux of

$$\tilde{\phi_O} = \frac{\tilde{I}}{nq_e\ell} = \frac{1}{3}\frac{10^{-5}\mu\text{A}}{2 \times 1.6 \times 10^{-19}\text{C}} = 1.04 \times 10^{11}\frac{\#}{\text{ms}}.$$

This may seem like a lot, but the actual variation in coverage is, in fact, small, since $\theta = \#adatoms/\Gamma$, where $\Gamma \approx 10^{19}\text{m}^{-2}$ is the number of oxygen sites per square meter of Pt surface, and the normalized flux (per site) is

$$\frac{\tilde{\phi_O}}{\Gamma} = \frac{1.04 \times 10^{11}\frac{\#}{\text{ms}}}{10^{19}\text{m}^{-2}} = 1.04 \times 10^{-8}\frac{\text{m}}{\text{s}}.$$

To estimate variations in surface coverage, we return to the solution for coverage on the surface in 2.27 and C.32,

$$\tilde{\theta}(r) = a_0\text{M}_0(r/\xi)$$

where a_0 is a constant defined from application of Fick's law at the electrode boundary as

$$a_0 = \frac{\tilde{I}}{nq_e\Gamma\ell D/\xi\text{M}_1(R_e/\xi)} \tag{3.14}$$

with ξ defined again as

$$\xi \equiv \sqrt{\frac{D}{j\omega + \alpha}}. \tag{3.15}$$

Time-varying fluctuations may then be approximated directly from the solution for θ by using the phasor formalism,

$$\theta = \Re(e^{j\omega t}\tilde{\theta}) \tag{3.16}$$

as

$$\begin{aligned}\frac{\partial\theta}{\partial t} &= \Re(j\omega e^{j\omega t}\tilde{\theta}) \\ &= \Re(j\omega e^{j\omega t} a_0 \mathrm{M}_0 \left(R_e/\xi\right)).\end{aligned} \tag{3.17}$$

The phasor, $\tilde{\theta}$, is the (complex) magnitude of an assumed sinusoidal θ solution. Variations are greatest at the electrode boundary, $r = R_e$, so the quantity in 3.17 will be evaluated there for the smallest electrodes ($R_e = 12.5$ μm). Such a calculation requires estimation of the parameters, D and ξ, at an appropriate frequency, ω, and triple phase boundary length, ℓ. $\omega = 0$ is a convenient value which is conservative in that it is the lower frequency bound, where fluctuations in θ are greatest. An estimate for α at T=800℃ from previous experiments with square Pt electrodes is around 30 rad/s. [9] Finally, we want to choose a large value of D. An appropriate estimate at T=800℃ is $D = 1.57 \times 10^{-7}$ m^2/s [53][10]. With $\tilde{I}_F/\ell = (1/3) \times 10^{-5}$ A/m, we find

$$a_0 = 0.00553;\ \xi = 7.23 \times 10^{-5};\ \tilde{\theta} = 0.00558$$

This value is adequately small for our perturbation assumptions[11]. However, at T=600℃, with $\alpha \approx 0.03$ and a smaller current response, these values become

$$a_0 = 0.0833; \xi = 1.50 \times 10^{-4}; \tilde{\theta} = 0.0834,$$

for which the coverage variation at the edge is not acceptable given the perturbation requirements. As such, it would be best to reduce the perturbation voltage from 1 mV to 0.1 mV. With DC resistances as high as $10^9\Omega$ for $\ell \approx 78.5\mu$m, DC current amplitudes would then fall to 10^{-13}, still within the 10^{-15} tolerance of the instrumen-

[9] It may seem inappropriate to take this parameter from a different experimental setup. However, it turns out that this same parameter is ubiquitous across the solutions of the governing PDEs for various geometries (see Appendix C). It corresponds to the corner frequency of the response, and contains information about the relative rate of the adsorption process (the distributed reaction).

[10] In fact, a Taylor expansion of $\tilde{\theta}$ at $\xi \to \infty$ gives $\tilde{\theta} \backsim \frac{2\tilde{I}}{nq_e\ell\Gamma\alpha R_e}$ to first order in $R_e/\sqrt{D/\alpha}$, so that $\tilde{\theta}$ is independent of D in this limit.

[11] though less so at low coverage, not because $\tilde{\theta}/\bar{\theta} \gg 1$, but because at low coverage ($\theta < 0.2$), D is very sensitive to θ, varying by a factor of six between $\theta \approx 0.02$ and 0.2 [37]

tation.

In practice, the voltage amplitude ought to be selected such that only the fundamental frequency of the voltage signal appears in the current signal[12], and the impedance response does not vary with the sinusoidal voltage amplitude, in which case the coverage signal may be adequately modeled as a perturbation about the mean. If, in adjusting the voltage amplitude such that the higher-order harmonics vanish, the current signal dips below 1 fA, then these data are of dubious quality. We have seen that the low-temperature measurements are potentially problematic in this respect, and so discretion must be used in their analysis.

[12]or the amplitudes of non-fundamental Fourier components are appreciably small, say 5% or less of the amplitude of the fundamental frequency

Chapter 4

Results and Discussion

4.1 Comments on Fabrication and Measurements

Layers of porous platinum were measured to be approximately 15 to 40 μm thick. The pore structure is discernible from Figure 4-1. Crude estimates of density of the film run between about 5 and 10 g/cm^3; by comparison of the density of platinum near room temperature, 21.45 g/cm^3, we conclude that Pt takes up between 20 and 50 percent of the space in the film.

To ensure that the porous Pt layer contributes only a small impedance to the total spectrum, EIS tests were performed on YSZ slabs coated on either side with porous platinum. The resulting spectra were characterized by a fairly low impedance dominated by the ohmic contribution of oxygen ion flow through the YSZ, as verified through proper scaling of impedance with YSZ thickness and area. This suggests that the porous platinum achieved the stated design goals. However, it is troubling that the activation energy of the YSZ ionic conductivity extracted from these measurements is around 0.55 eV, where the literature records an activation energy of about 1.2 eV for (100) single-crystal YSZ [19]. The discrepancy may be caused in part by a vertical gradient in temperature through the YSZ bulk (about 25-30°C per millimeter thickness).

Data was taken at oxygen partial pressures of 10^2, 10^3, 10^4, and 10^6 ppm, and at temperatures between approximately 475 and 700°C, as determined by a calibration

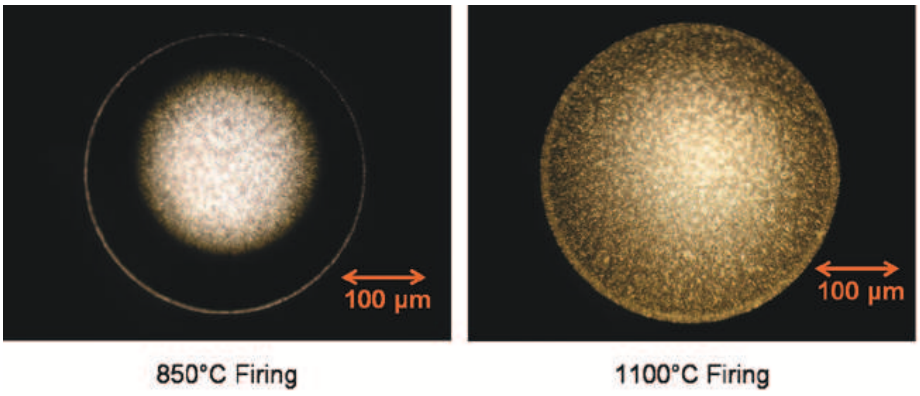

Figure 4-1: Optical micrographs of porous platinum counterelectrode, 100× magnification. Left: firing temperature of 850 ℃; Right: firing temperature of 1100 ℃. In the present study, samples fired at 1100 ℃ are used.

via a thermocouple independent from the thermostat. Unless otherwise noted, all data referred to in this chapter was taken from samples with a YSZ thickness of approximately 0.25 mm.

4.1.1 Instability at High Temperatures

While the use of patterned, dense, thin film electrodes allows for precise control of geometry, it is also prone to nonstationarity which destroys this precision. In particular, the dense Pt electrodes are unstable at high temperatures, and tend to pit, perhaps as they transition toward a porous structure. The time scale of this degradation process depends upon temperature and processing conditions, but visible signs begin to appear within an hour of exposure to 800℃. An EIS measurement typically takes between ten minutes and one hour, depending upon temperature and pressure, to sufficiently probe the frequency range of interest.

This kind of electrode degradation presents several difficulties to data analysis. If a pore forms that reveals the underlying electrolyte, then additional triple phase boundary will have been created, and no longer can the perimeter of the electrode be used as an estimate for the total triple phase boundary length. Ideally, there would not be any sufficient changes to surface characteristics, so that the deviation in EIS response from an undegraded sample would be purely due to geometry. Indeed,

practical catalysts for SOFCs, including Pt, are porous, and the technical utility of this study hinges upon its ability to capture the properties of Pt in this configuration. However, it is more likely that the additional surface roughening does alter the diffusivity and adsorption parameters (perhaps due to the increased concentration of surface defects) at least to the point where quantitative comparison between different spectra may not be possible. This is particularly problematic in that it implies that errors due to degradation begin to appear as soon as the electrodes reach high temperatures, and before any deep pits form.

Figure 4-2 displays optical micrographs that show the evolution of degradation after exposure to 800℃. Microelectrodes are not raised to this temperature during experiments, and the sample is changed long before any of the larger pits seen in the optical micrographs form. Nonetheless, this degradation puts an upper temperature bound on the EIS experiments which is below temperatures used in the current iteration of SOFC technology.

4.1.2 Temperature Gradients on Sample Surfaces

The setup of these experiments rendered isolating temperatures a very difficult task. Variations between electrodes within a single row were typically less than ±10℃ from the mean, but global differences on the sample could reach as high as 30℃ or more. While imperfect, these "near isotherms" may be more informative than a three-dimensional rendering, and perhaps no less accurate than attempts to extrapolate a true isotherm.

Again, vertical temperature gradients through the YSZ were also present - they were measured at approximately 25-30℃ per mm YSZ. Such gradients render difficult accurate measurement of YSZ properties from EIS spectra. However, the contribution to impedance by YSZ is a constant real resistance, and since all parameter extraction was carried out for samples with a uniform thickness of 0.25 mm, these gradients are not expected to impact this investigation.

Table 4.1 shows the mean, minimum and maximum temperatures for the isotherms used in Section 4.3.

(a)

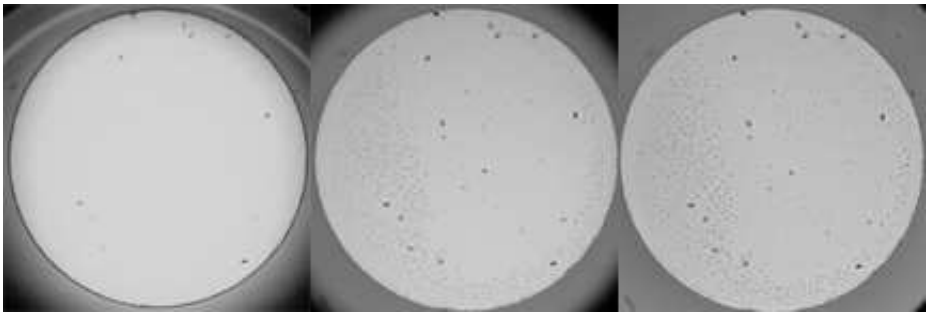

(b)

(c)

Figure 4-2: Optical micrographs showing the degradation of a 400 μm-diameter microelectrode. Middle and right-most images are after one and two cycles from room temperature to 800℃ at 17℃/min. Note that the electrodes were not deposited in the same batch, and may be of different thicknesses, so difference in degradation may not be due thin polycrystalline YSZ film. (a) Electrode deposited directly on single-crystal YSZ. (b) Electrode deposited on polycrystalline YSZ (grayscale). (c) A damaged 400 μm-diameter electrode; pitting is a result of prolonged exposure to high temperatures, and the gash is due to contact with a probe tip - the gash is atypically large. Testing on this electrode was stopped well before this level of damage had accrued.

Table 4.1: Mean, minimum, and maximum temperatures for every isotherm series.

Mean Temperature (℃)	# Data Points	Minimum (℃)	Maximum (℃)
476	1	476	476
531	2	524	537
560	3	557	564
605	4	603	610
646	4	638	655
689	2	680	698

It should be noted that the probe tip, itself, acts as a heat sink applied directly to the electrode surface. Temperature calibration was performed using a separate, external thermocouple which did not take this fact into account, though temperature gradients around probe tips were observed during calibration.

4.1.3 Triple Phase Boundary

It is a fundamental assumption of this work that the triple phase boundary length is the perimeter of the electrode. This perimeter may be estimated from the design parameters of the electrodes, but due to processing limitations and edge roughness, the actual perimeter ought to differ from this estimate. To address this disparity, scanning electron micrographs were taken of several 50 μm-radius electrodes. With the help of edge filtering algorithms, the perimeter was then estimated for these electrodes; the electrodes' radii were also estimated by fitting a circle to the extracted electrode edge points. Figure 4-3 briefly illustrates how this was accomplished. It should be noted that noise in the pixelated perimeter causes a tendency to overshoot the actual perimeter. On the other hand, the presence of microstructural features on a scale below the resolution of the image would suggest that the estimated perimeter is too small. As such, it is hard to say whether the method used to extract the electrodes' perimeters underestimates or overestimates the value.

It is conceivable that thermal and electrochemical cycling may affect the triple phase boundary length. To address this possibility, high-resolution scanning electron micrographs were obtained for two microelectrodes on the sample YSZ substrate, one

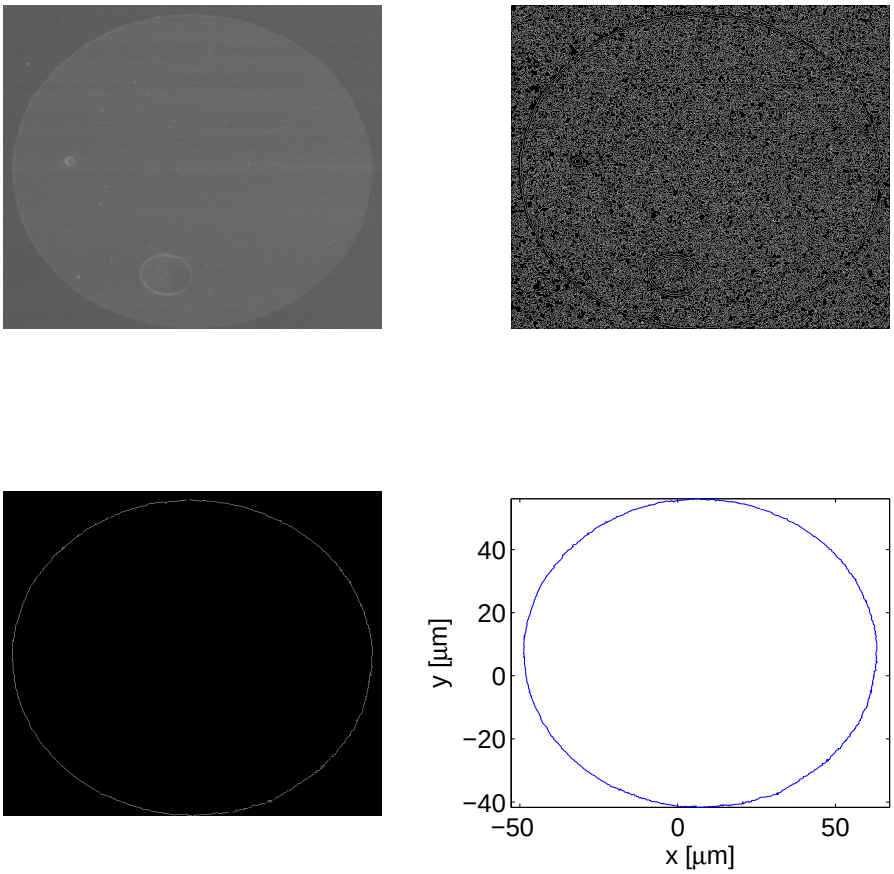

Figure 4-3: Steps of extracting the perimeter of the electrode from digital scanning electron micrographs. The original image is run through an edge filter; the edge of the microelectrode is extracted from this display manually, and the outer points are then selected as representative of the electrode edge.

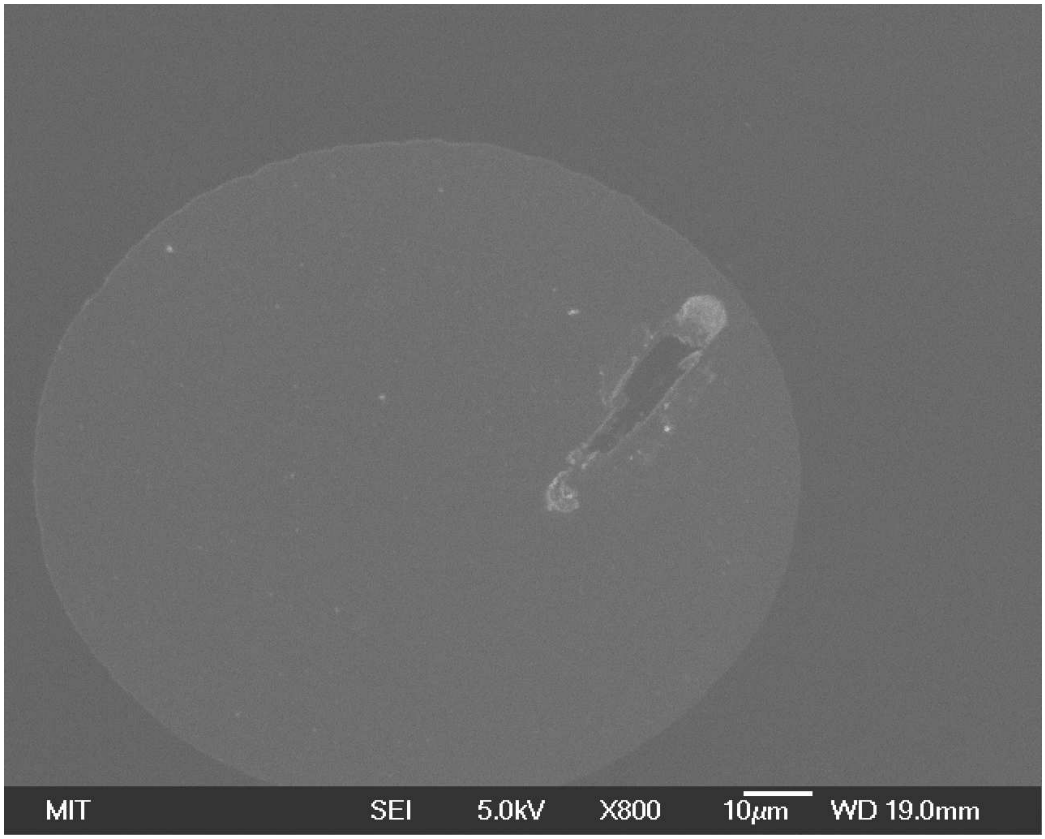

Figure 4-4: A 100 μm-diameter (50 μm radius) electrode at 800× magnification after an electrochemical impedance spectrum has been obtained. The measurement was run at about 700°C, and the surface was exposed to atmosphere. The gash in the surface is left by the probe tip, and is large relative to usual damage caused by the probe; its Pt-YSZ contact length is about 19 μm, or about five percent of the electrode perimeter.

exposed to a thermal cycle but never having undergone an EIS measurement, and the other submitted to an EIS test during the thermal cycle. Table 4.2 shows the perimeters and radii extracted from this set of images. The change in perimeter and radius is probably negligible in either case, though it is perhaps noteworthy that the best-fit radius, a parameter more insensitive to noise because it averages over all edge data points, increases slightly in both measurements after a thermal cycle. Further, both electrodes are characterized by an actual radius slightly larger than the design goal of 50 μm, and by a perimeter about 10 to 15 % larger than that of an ideal circle with the best-fit radius.

While the perimeter of the electrodes did not change appreciably after one thermal

Table 4.2: Actual perimeters and radii of two ∼50 μm-radius electrodes.

	Before Cycle [μm]	After Cycle [μm]
One thermal cycle, no EIS measurements		
Radius	51.8	52.3
Perimeter	377	374
Thermal Cycle, one EIS measurement		
Radius	51.9	52.8
Perimeter	359	362

cycle, the gash in the Pt thin film left by the probe tip constitutes a marked difference in the surface. The gash does not form immediately as the probe tip is placed down; the SUSS manual probeheads allow sufficient vertical resolution such that the probe might be extended until contact is observed, and then retracted quickly without significantly damaging the surface. Rather, the gash forms over the duration of the EIS measurement (usually 10 to 20 minutes). Probe tip vibration or creep might be speculated as the mechanisms behind this slow destruction; regardless, it surely contributes to bias error within a single electrochemical impedance spectrum, and makes the lower-frequency data (which are measured last and take the longest time to gather) less reliable.

Figure 4-4 shows a scanning electron micrograph of a 50 μm-radius electrode after a single EIS run at around 700°C. The gash is clearly visible in the upper-right-hand corner of the electrode; its Pt-YSZ contact length is about 19 μm, equivalent to roughly five percent of the electrode's external perimeter as measured from the technique described above.

4.2 Basic Scaling Analysis

Scaling analysis is a fundamental and essential technique to examine the behavior of the spectra, and can be used to rapidly assess the validity of the proposed model. Further, the use of microlithography to create solid, non-porous electrodes allows for accurate knowledge of electrode geometry. This makes conclusions drawn from scaling more reliable relative to those drawn from experiments using electrodes created from

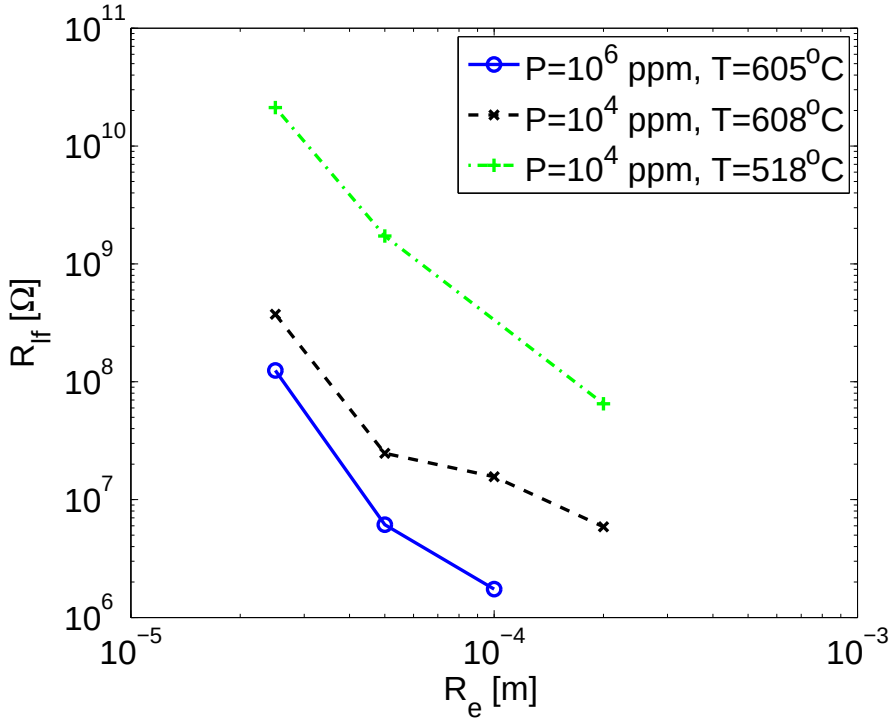

Figure 4-5: Scaling behavior of the low-frequency intercept in the complex impedance plane for three thermodynamic states.

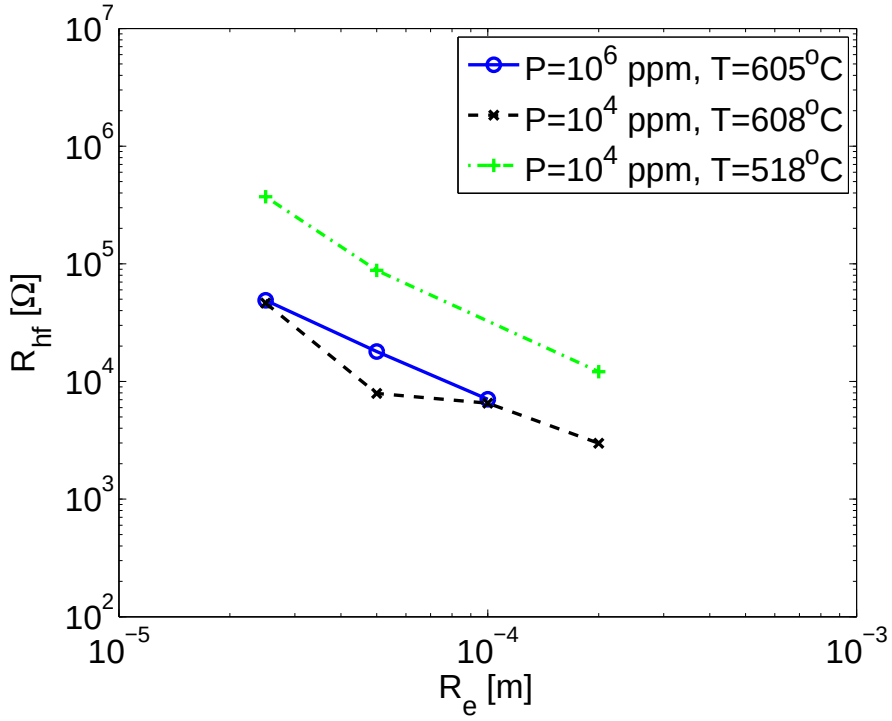

Figure 4-6: Scaling behavior of the high-frequency intercept in the complex impedance plane for three thermodynamic states.

platinum paste (as in[37], for example).

The theoretical picture presented in Chapters 2 and 3 supply expected behaviors of the spectra with respect to electrode size. One convenient way to probe the success of this picture in predicting data is to analyze the scaling dependence of the limiting low- and high-frequency intercepts of the spectra with the real axis in the complex plane. Some care is needed to extract the value of these intercepts. Here, the low-frequency intercept of the spectrum with the real axis, R_{lf}, is estimated by fitting a circle to the data in the complex plane - a reasonable empirical fit in the low-frequency regime. The high-frequency intercept, R_{hf}, is found by extending a line at 45° from the real axis to the impedance point of smallest real value (the high-frequency intercept of the cylindrical impedance contribution is masked by electromagnetic capacitance and interfacial capacitance - see Section 4.3.1).

As expected, both the low- and high-frequency intercepts decrease monotonically with electrode radius. Notice that the high-frequency intercept does not depend strongly on pressure, but does decrease significantly as temperature is increased. This is consistent with the view that the low-frequency intercept is dominated by the contribution from the ohmic resistance of the electrolyte.

R_{hf} follows the electrode radius between $R_e^{-1.2}$ and $R_e^{-1.6}$. As discussed in Section 2.4.3, such variation is not unexpected due to the complicated problem presented by ohmic conduction across the Pt/YSZ interface and through the YSZ bulk[1].

The observed scaling of R_{lf} with R_e is more-pronounced than that measured for R_{hf}. Best fits of $R_{lf} \propto R_e^a$ show a between -1.9 and -3.1. In Section 2.4.3, a was predicted to fall between -1 and -2 depending on the ratio, R_e/l_δ, which defines whether the system is in the "Gerischer" ($R_e/l_\delta \gg 1$), transition ($R_e/l_\delta \approx 1$), or semicircular ($R_e/l_\delta \ll 1$) regimes. As such, the observed dependence of R_{lf} on R_e seems too strong in some cases. However, a transition between a steeper size dependence for

[1]It might be helpful to envision a cone of ion conduction extending down from a point on the perimeter of the electrode to the semi-infinite counterelectrode; the three-dimensional geometry through which the ions flow might then be estimated by revolving this cone around all points on the electrode perimeter. Thinking in this way, as the ratio of electrode radius to thickness, R_e/t, is increased, the ohmic resistance ought to appear as transitioning from being fairly independent of R_e to suddenly becoming strongly dependent, before leveling off to $\propto R_e^{-1}$. With this in mind, the observed dependence on R_e is reasonable.

small R_e (i.e. $R_e \ll l_\delta$) to a shallower size dependence for larger R_e (i.e. $R_e \gg l_\delta$) is recognizable, especially for the 600℃ and 10^4 ppm data series, and occurs on a length scale between 10 and 100 μm, slightly smaller but on a similar scale as observed in Dr. Koc's data in Figure 2-7 for the larger temperature of 700℃. Again, the electrode size at which the transition between scaling dependencies occurs is indicative of the scale of the utilization length, l_δ. The scale of l_δ for solid, sputtered thin-film Pt observed here, consistent with data collected for square electrodes by Dr. Koc, is two to three orders of magnitude larger than that reported elsewhere for porous Pt [2].

It is also of note that R_{lf} depends strongly on both temperature and pressure, providing evidence to the importance of sorption in the determination of the impedance for this frequency range.

4.3 Results of Fitting

Fitting was carried out in two steps. In the first pass, the trial function included a double-layer capacitance in parallel and electrolyte resistance in series with the Faradaic impedance. Based on the least-squares fits for C_{dl} and R_{ysz}, the Faradaic impedance was extracted from the raw data, and a second pass fit was carried out for only the Faradaic impedance parameters using the values from the first pass as initial guesses. For most spectra, the double-layer capacitance was small enough to be ignored.

Initial guesses were painstakingly determined by hand via trial and error; typically, least-squares minimization of these initial guesses resulted in stable solutions, but occasionally, multiple local minima were found for multiple initial guesses within the same vicinity of one another. Further, for many spectra, the low-frequency corner-frequency, controlled through γ_3, was fixed, as this parameter is readily identified from a Bode plot of the spectrum. In some cases, the initial guesses better captured the corner frequencies and general shape of the impedance spectrum, even though the least-squares solution resulted in a lower norm of residuals. Because it is assumed that the corner frequencies of the Bode plot are more reliable than individual data

points and therefore deserve a greater weight in the fitting, in these cases, the initial guess were retained as best fit.

4.3.1 Double layer and Electromagnetic Capacitance

Double layer capacitances were as large as 9.5 nF, corresponding to about 1.2×10^{-4} F/cm^2 for this particular 50 μm-radius electrode, but typically much smaller by several orders of magnitude so as to be negligible. This maximal capacitance value has also been captured in EIS experiments elsewhere [2]. Again, there is significant scatter in reported double layer values [2]; this may be due to the fact that, strictly speaking, the measured parameter is the *interfacial* capacitance, which depends not only on double layer effects, but on chemical processes, as well [19].

Figure 4-9 illustrates how the double layer capacitance appears in the impedance spectrum. The Nyquist plot shows a bulge at the high-frequency end which increases the curvature of the locus of impedance points such that the angle at which the locus intersects the real axis is no longer 45°. The effect is distinct from the semicircular limit of the cylindrical-geometry Faradaic impedance model because this model will produce a Nyquist plot where the locus of impedances *always* intersect the real axis at 45° if high-enough frequencies are probed.

If the basic Randles circuit accounted for all impedance contributions, then the impedance spectrum ought always to intersect the real axis at an angle of 90° on the Nyquist plot at high-enough frequencies, as the double layer capacitance will eventually short out the Faradaic component[2]. However, the electromagnetic capacitance - caused by field, or "displacement current", coupling of the electrode with the counterelectrode - introduces another semicircle in the Nyquist plot, as visible in Figure 4-10 for the lowest-temperature series. While the total impedance is not exactly a superposition of the two semicircles, they nonetheless combine in a transition region which modifies the high-frequency intercept angle[3]. Unfortunately, in the presence

[2]though at some point, modeling the double layer's effect as a capacitor will no longer be accurate

[3]In fact, the impedance locus does not really intercept the real axis in this transition region, though it comes close to doing so.

of these additional contributions to impedance, it becomes difficult to extract any information about Faradaic processes from the highest-frequency data.

The fact that these small secondary capacitances are more visible at low temperatures is a consequence of a higher Faradaic impedance magnitude at these temperatures. The shunt paths these secondary capacitances create between electrode and counterelectrode have high impedances for the frequencies under investigation. As such, they only modify the observed impedance spectrum in a sensible way when the Faradaic impedances are also very large.

Because the double layer exists over the entire area of the Pt-YSZ interface, the double layer capacitance scales as R_e^2, while the Faradaic impedance contribution scales as R_e. As such, double layer capacitance data might be analyzed for proper scaling in order to verify whether the understanding of this impedance behavior is correct. However, as these capacitive effects are not visible in every spectrum, double layer data is incomplete, and so such an analysis has not been carried out.

4.3.2 Representative Electrochemical Impedance Spectra

The following Nyquist and Bode plots in Figures 4-7, 4-8, and 4-9 demonstrate good fits to data in both the semicircular and Gerischer regimes. Figures 4-7 and 4-8 illustrate a spectrum which is primarily in the "transition" regime between the semicircular and Gerischer limits. In the Nyquist plot, 4-7, this is visible from the bulge in the spectrum at low frequencies and large impedances and the clear high-frequency asymptote along the 45° line. The detail of the Nyquist plot shows additional curvature in the locus at very high frequencies; this is due to the double layer capacitance.

The Randles-circuit fit to the data is able to capture most of the behavior of the spectrum. To provide a sense of how close initial guesses ought to be to ensure convergence, the initial guess is plotted alongside the data and least-squares fit. The Bode plot, Figure 4-8, provides more detail regarding the accuracy of the fit with respect to frequency. In particular, the phase plot shows where the model has trouble accommodating the measured spectrum. Further, the measured spectrum seems to be somewhere in between those of the initial guess and the least-squares minimum,

illustrating the difficulty and ambiguity inherent in the process of data extraction.

It should be noted that these plots show only the first-pass in the fitting procedure, for which the Randles circuit is used. In the next pass, the Faradaic impedance is extracted from the measured spectrum using the fitted double layer capacitance and electrolyte resistance values, and another least-squares pass on this Faradaic impedance is performed to produce the final set of parameter values.

With a temperature about 75℃ lower than in 4-7, but with the same pressure and electrode radius, the spectrum in Figure 4-9 appears much more Gerischer-like, with an elongated 45° high-frequency asymptote and no visible bulge. Alongside the raw data is shown the Faradaic impedance extracted after the first-pass fit; it appears even more Gerischer-like as some curvature at higher frequencies has been removed. The double-layer capacitance, C_{dl}, found in this case was 4.35 nF, corresponding to 5.54×10^{-5} F/cm^2 for this 50-μm-radius sample. Finally, the second pass fit is shown to satisfactorily describe the measured impedance spectrum.

It is worthwhile to comment on the differences between these two spectra. For the same electrode radius, the spectrum has shifted from a predominantly semicircular shape to that of a Gerischer (teardrop). In the language of the colimited ORR model presented here, this would be consistent with a shortening of the utilization length, $l_\delta = \sqrt{D/\alpha}$. The change was effected by lowering temperature while holding all other experimental variables constant. Whereas both dissociative adsorption and diffusion are thermally activated processes, both might be expected to be reduced after the temperature reduction; however, it is very plausible that the change in D is much more pronounced in α, as the activation energy of dissociative adsorption is significantly smaller than the adsorption energy (see [18], where the dissociation energy of 0.38 eV compares to and a binding energy of 2.6 eV]). Following the rule-of-thumb suggestion of Hopster et al. in estimating the diffusion barrier at one half the desorption energy [20], the observed transition toward a more Gerischer-like appearance in impedance spectra as the temperature is lowered, all else equal, is entirely consistent with the colimited ORR model and its concept of the utilization length.

To underscore this point, Figure 4-10 superimposes the high-frequency regimes

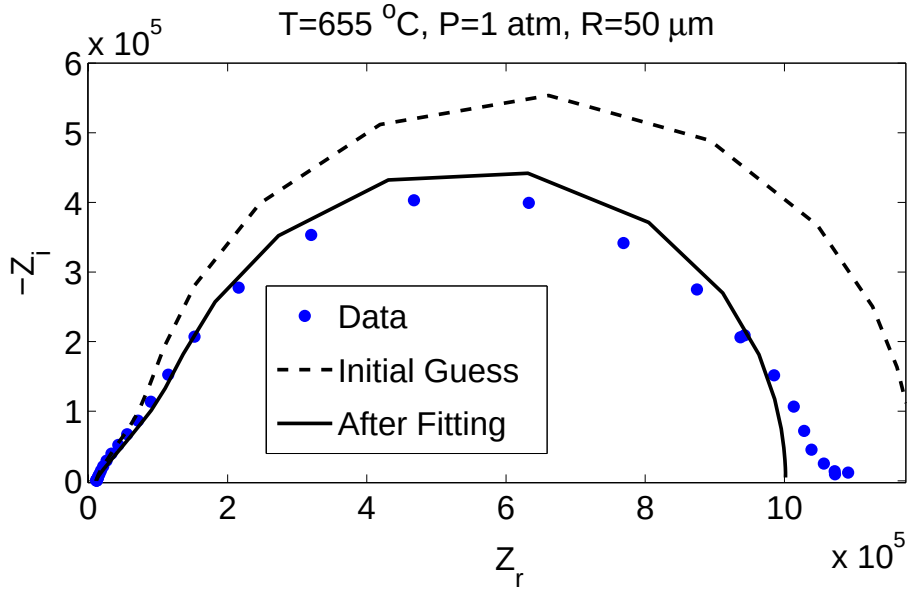

(a)

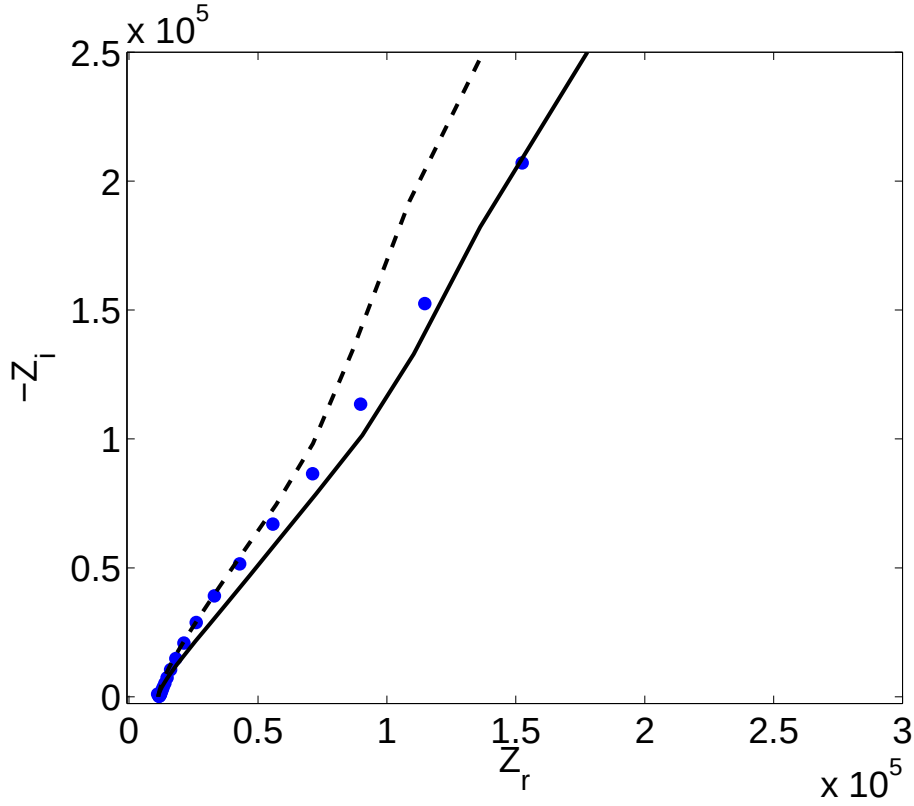

(b)

Figure 4-7: Nyquist plots of data taken at T≈640°C, P=1 atm, for an electrode with radius, 50 μm. The data is primarily in the semicircular regime, but still displays the characteristic high-frequency 45° asymptote. (a) Nyquist plot; (b) Nyquist detail.

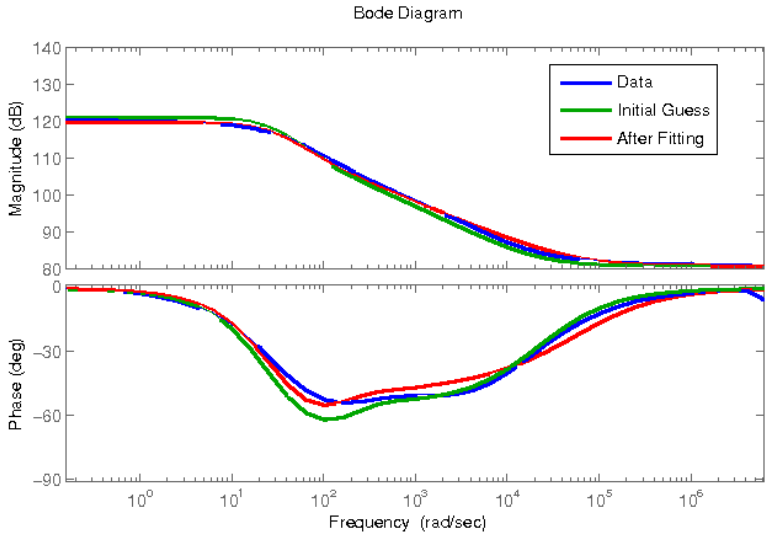

Figure 4-8: Bode plot of data taken at T≈640℃, P=1 atm, for an electrode with radius, 50 μm. Complements Figure 4-7.

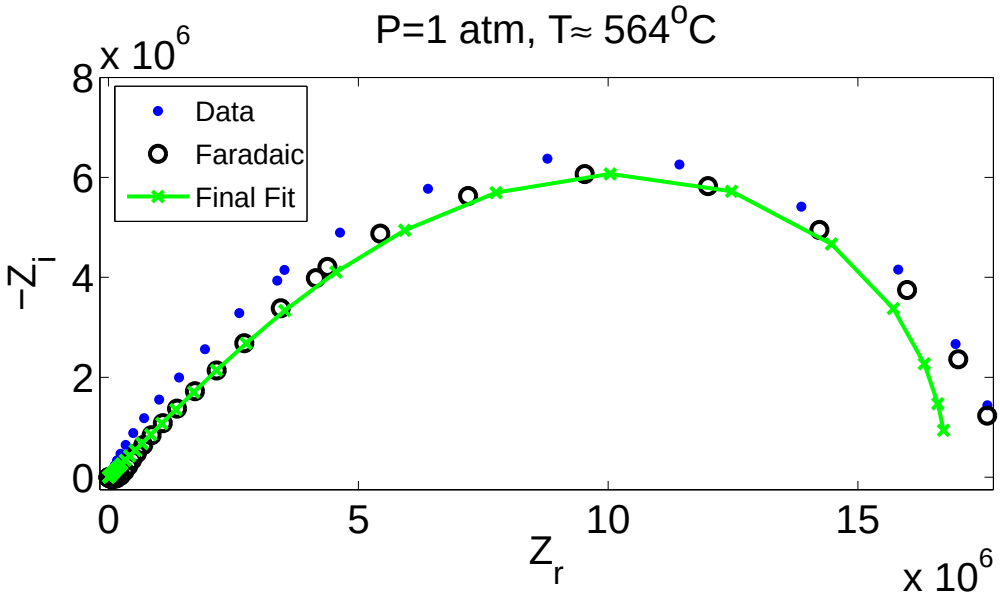

Figure 4-9: Nyquist plots of data taken at T≈564℃, P=1 atm, for an electrode with radius, 50 μm. An additional fitting step including the double-layer capacitance and electrolyte resistance is shown - the raw data is shown alongside the data after a best-fit contribution from C_{dl} and R_{ysz} are extracted. The spectrum is in the "Gerischer" regime.

of the Nyquist representation of several impedance spectra, each with a different temperature but with all other experimental conditions the same. Again, the spectra appear more Gerischer-like at lower temperatures, and more semicircular at higher temperatures. As discussed earlier, the figure also illustrates how the double-layer and electromagnetic capacitances modify the measured spectra, and shows these effects to be more pronounced in the lower-temperature series.

4.3.3 Estimation of Utilization Length by Visual Inspection

Figure 2-7 demonstrated the ability to extract the utilization length, l_δ, from EIS data by comparing spectra taken at the same temperature and pressure, but for different electrode radii; l_δ is estimated by identifying the electrode size marking the transition from semicircular to Gerischer-like forms. However, the same trend was not clearly identified here. Figures 4-11, 4-12, and 4-13 superimpose Nyquist and Bode plots of impedance spectra for multiple radii. The high-frequency real impedance intercept (asymptote) has been extracted from each spectrum; this is done so that the high-frequency phase angle matches the angle above the real axis in the Nyquist plot. The expected trend was shown in Figure 2-5, where the 45° portion of the Nyquist plot elongates (or the high-frequency corner frequency at 45° in the phase plot becomes smaller) as the Nyquist plots tend toward a Gerischer shape. This trend is perhaps viewed in the phase plot of 4-11, but not convincingly. Further, Figure 4-13 pairs the 25 and 200 μm as having approximately the same high-frequency corner frequency in the phase plot, as well as the 50 and 100 μm corner frequencies. The absence of the expected trend is not likely due to temperature differences between the measurements, as the 25 and 50 μm spectra show the opposite of the expected trend (the 50 μm spectrum has a smaller high-frequency corner frequency than the 25 μm sample).

On the other hand, the low-frequency corner-frequency remains largely invariant with respect to electrode radius, as expected (see Section C.44). Further, scaling trends in the low-frequency intercept seen in Figure 4-5 do potentially reveal the scale of the utilization length, placing the parameter between 10 and 100 μm for the

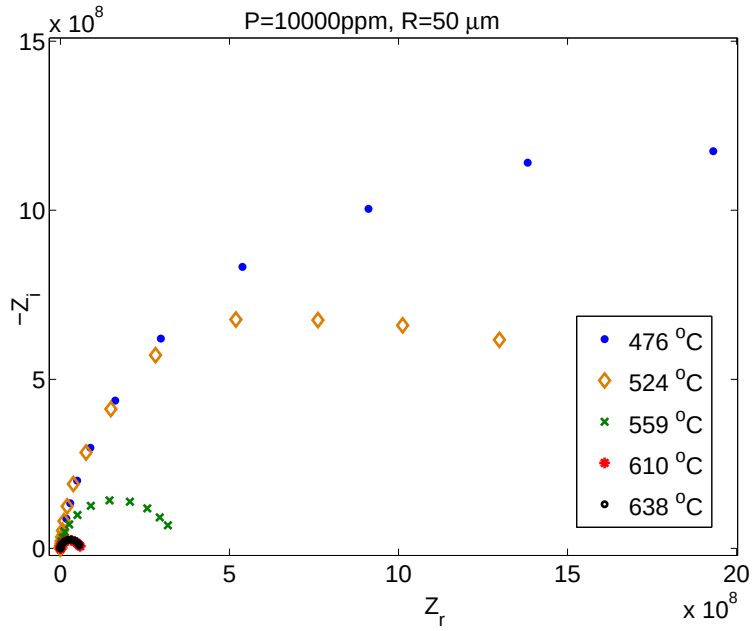

(a)

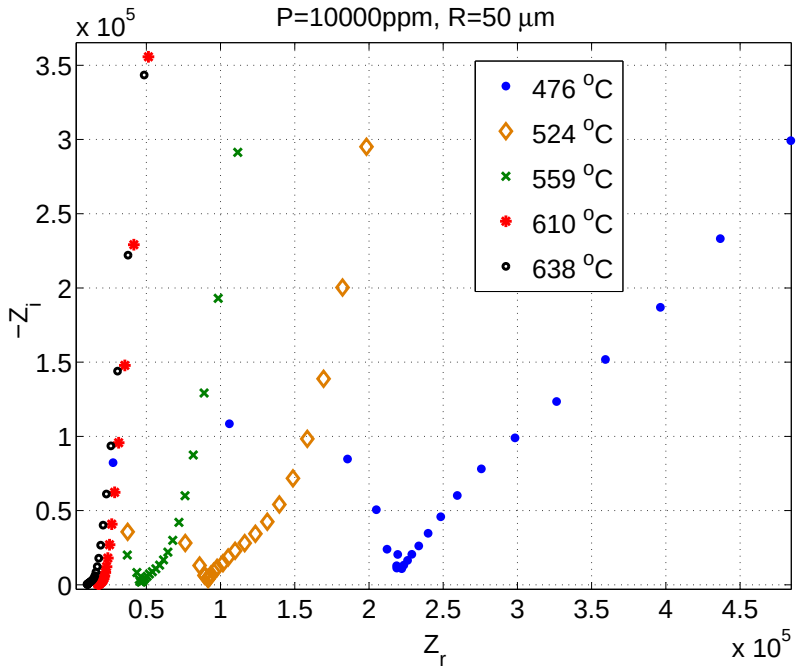

(b)

Figure 4-10: (a) Nyquist plots showing impedance spectra taken at several temperatures with a pressure of 10^4 ppm O_2. (b) Detail around high-frequency (HF) region. As temperature (T) increases, spectra become more semicircular, consistent with the idea that the active region on the electrode is extended due to a greater diffusivity. The C_{dl} tends to round out the 45° line in the HF region to a semicircular shape, and the electromagnetic capacitance creates a second, semicircular feature at very high frequencies; these effects appear prominently in the lowest T series.

temperatures and pressures shown.

4.3.4 A Note on Reproducibility and Error Estimation

In the following sections, error bars are displayed in the figures for each parameter of interest that has been extracted from the data. The method used to calculate this error is discussed in detail in Section D.2.2 in the appendix. Variances for each data point of the electrochemical impedance spectra were estimated by obtaining ten spectra consecutively from the same electrode and calculating the standard deviation at each frequency sampled; the resulting *normalized* standard deviation was then assumed to apply for any spectrum at any condition. Figure 4-14 shows EIS spectra from two different electrodes used to calibrate the error estimation. The color of the series distinguishes one electrode's data from the other's. The spectra demonstrate generally good reproducibility, both from a single electrode and between different electrodes. The Bode plot in Figure 4-14b confirms nearly identical corner frequencies for each spectrum. Figure 4-14a renders the data in a Nyquist plot; here, the solid lines link impedances measured at the same frequency, and roughly indicate the order in which the data was taken. Variation in the Nyquist plot is relatively random about a fixed mean, confirming the unbiased assumption; however, in the blue series, the final three to four data points for each frequency may witness a trend toward decreasing impedance magnitude with time. A detail at the high-frequency limit shows smaller percentage error in this regime; this is also confirmed by a decreased spread in the Bode plot for frequencies greater than about 1 kHz.

Due to contraction on the logarithmic axes in many of the plots, error bars are often so small as to be invisible. In general, however, the average normalized standard deviations, less extreme outliers, are as follows: for the linearized adsorption rate, α, $\pm 5\%$; for diffusivity, D, $\pm 5\%$; for the utilization length, l_δ, $\pm 3.3\%$. These error estimates might seem optimistic; however, it should be emphasized that they refer only to the unbiased error implied by extracting physical parameters given the inherent experimental variation in impedance spectra. Systemic inaccuracies in the models used to infer physical parameters indirectly from electrochemical impedance

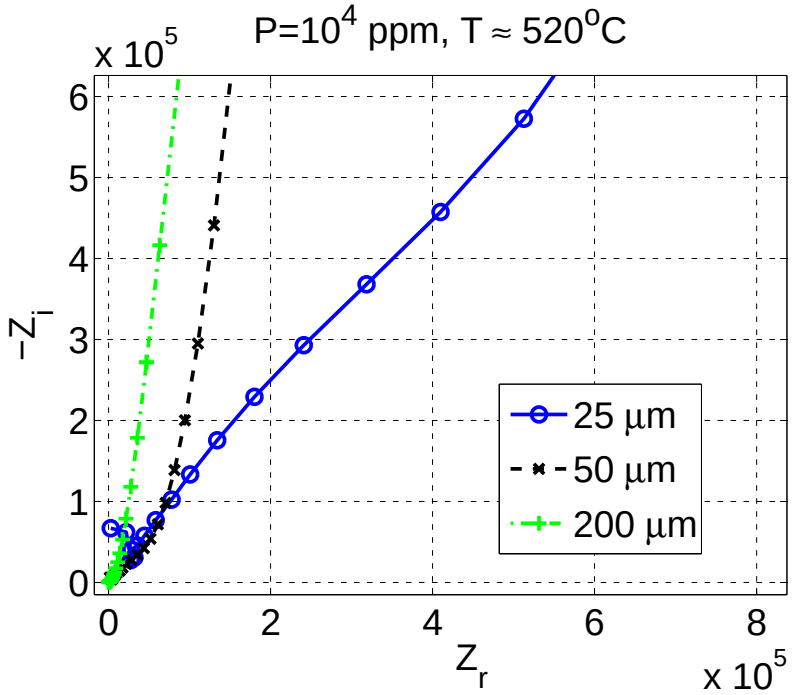

(a)

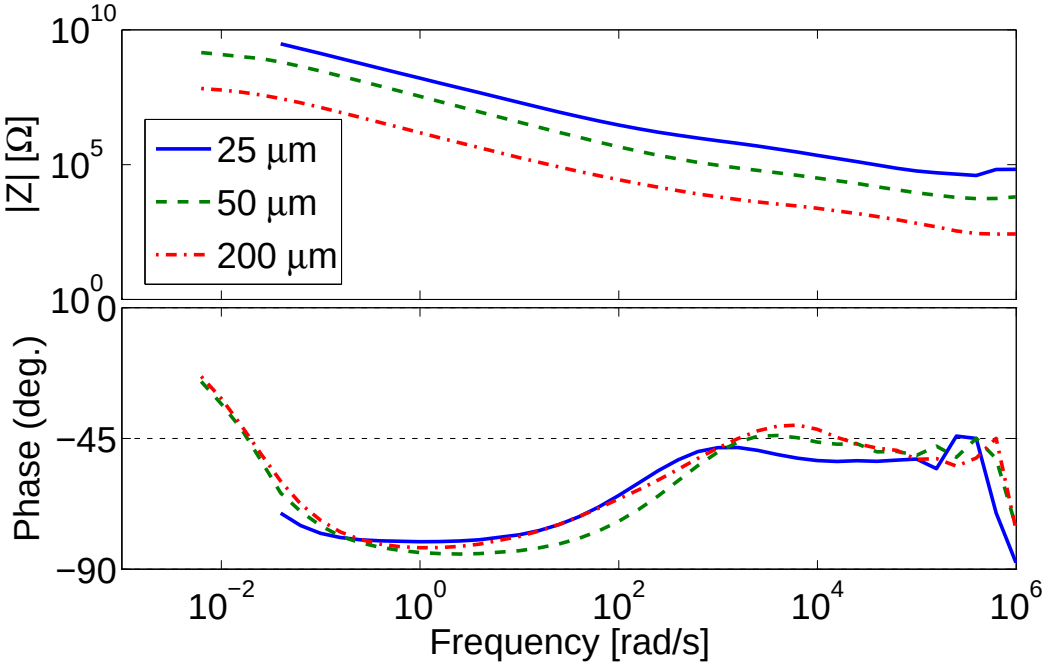

(b)

Figure 4-11: (a) Nyquist and (b) Bode plots of impedance spectra taken at $P = 10^4$ ppm O_2, T=512-524℃. Spectra from electrodes with three different radii are shown, but the expected trend as displayed in Figure 2-5 is not clearly exhibited.

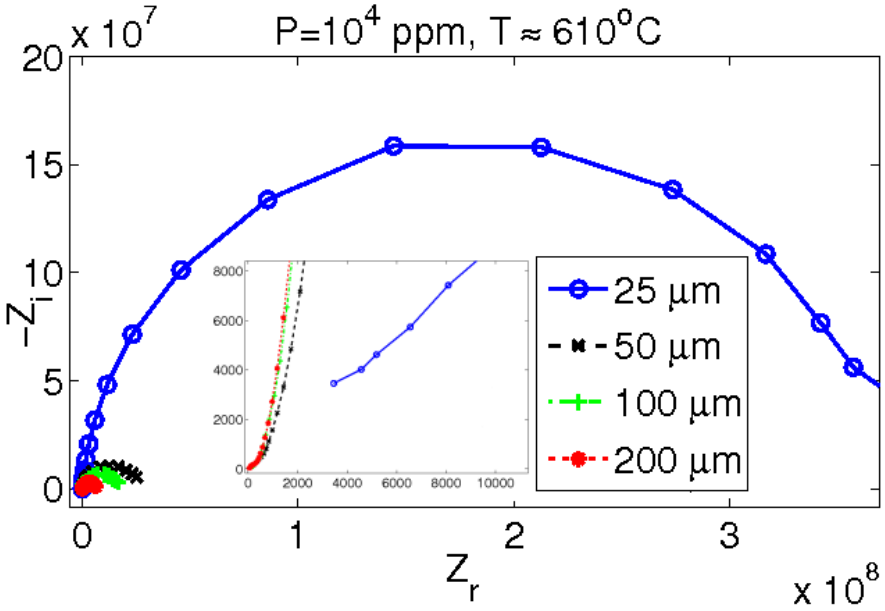

(a)

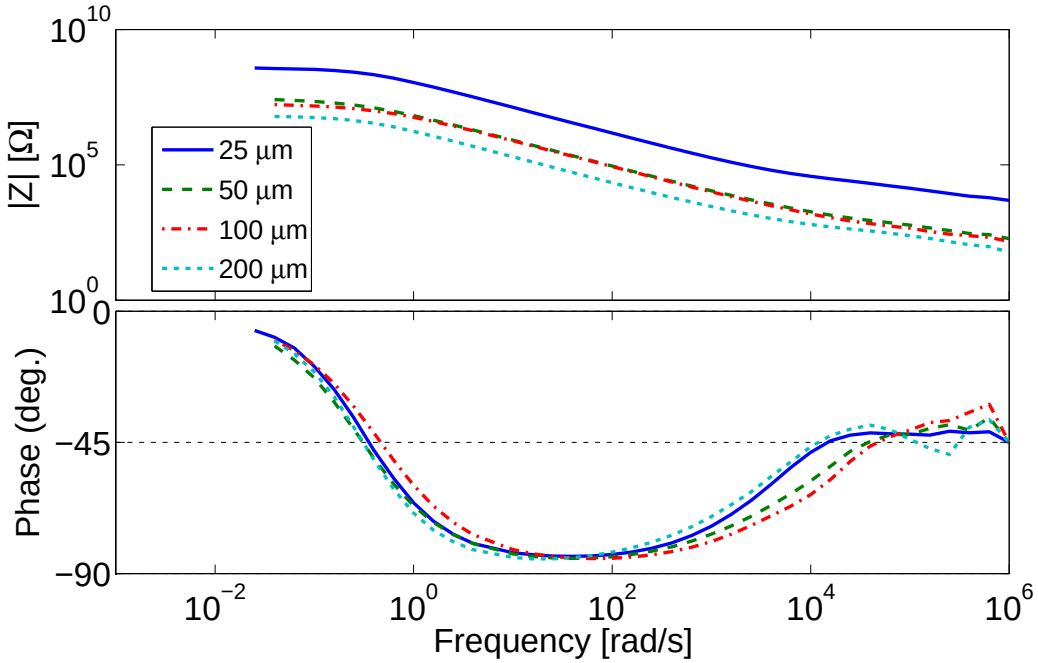

(b)

Figure 4-12: (a) Nyquist and (b) Bode plots of impedance spectra taken at $P = 10^4$ ppm O_2, T=597-616℃, for for different radii. The inset in (a) shows a detail of the high-frequency portion of the Nyquist plot.

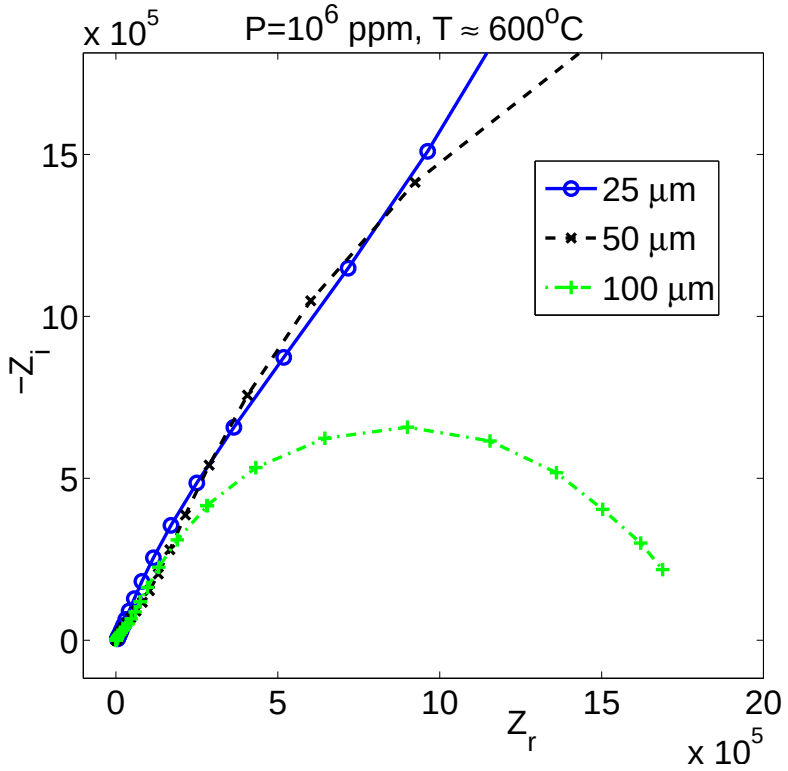

(a)

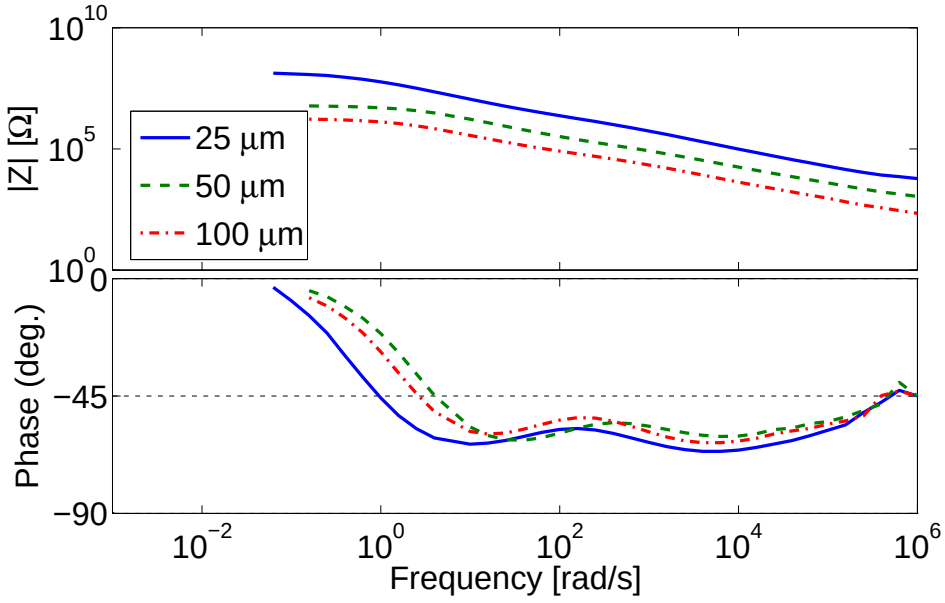

(b)

Figure 4-13: Nyquist and Bode plots of impedance spectra taken at $P = 10^6$ ppm O_2, T=597-612°C. Again, spectra from electrodes with three different radii are shown, and the expected trend as displayed in Figure 2-5 is not clearly exhibited.

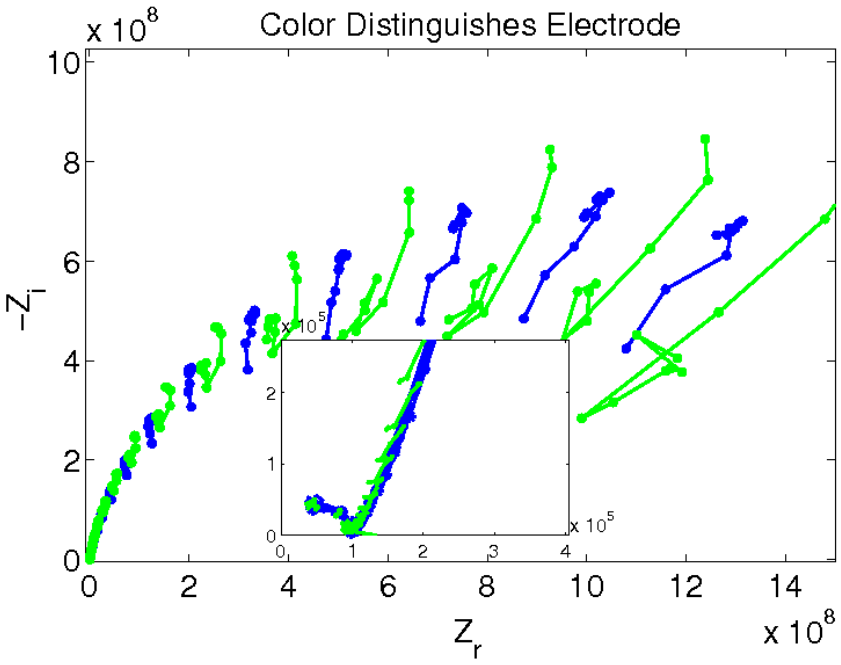

(a)

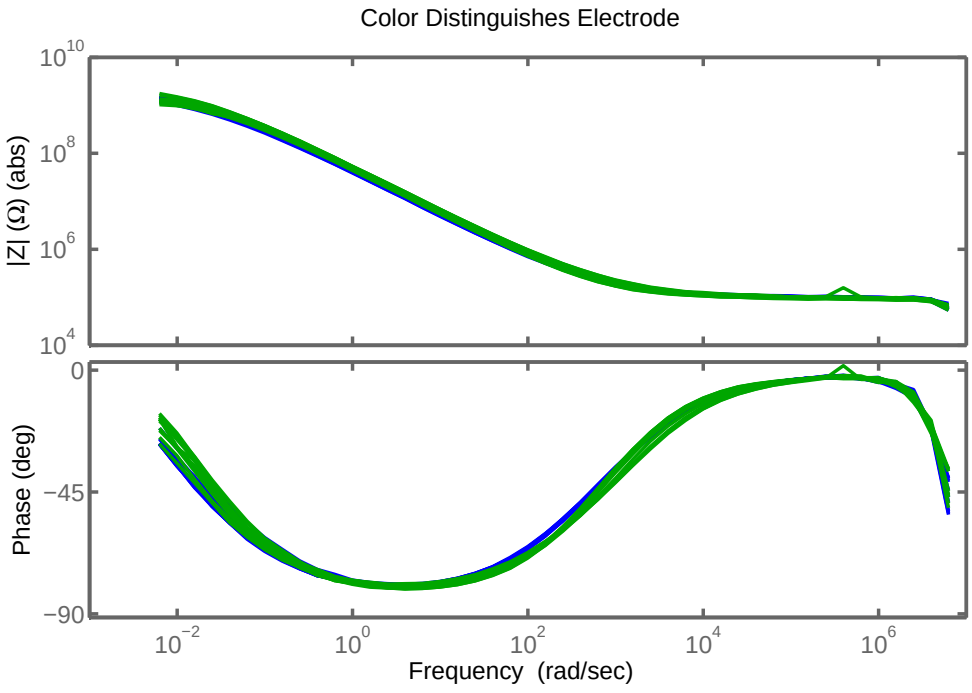

(b)

Figure 4-14: (a) Nyquist and (b) Bode plots of error calibration data. In each figure, ten spectra are shown for each of two different 100 μm-diameter electrodes. The electrodes were exposed to air, and the surface temperature was about 525℃. Green and blue color distinguishes one electrode's data from the other. In error calculations, standard deviations from *only the green* dataset are used.

spectra are not included, and neither are errors associated with uncertainty in the state variables, temperature and pressure, as well as in the triple phase boundary length. Variation between properties of different electrodes should also be expected due to non-idealities in materials processing. Nevertheless, the low error estimates demonstrate a natural robustness of EIS analysis which results from the fact that many frequency points are sampled in each spectrum, and each extracted parameter includes information from all of these measurements[4].

4.3.5 Coverage Isotherm

In Chapter 3, two methods were outlined for determining the coverage. While both are valid in theory, that described by 3.7 has the advantage of requiring fewer literature parameters, in particular regarding the adsorption process. It is also much simpler to implement.

The coverage obtained from this scheme is shown in Figures 4-15 and 4-16. Figure 4-15 displays both the lower and upper roots of 3.7. Those roots yielding a trend of generally increasing θ with pressure and decreasing θ with temperature, all else equal, were selected as the "true" coverage, and are displayed in 4-16. Certainly, there is a degree of interpretation in this selection process.

Also, the two points with coverage equal to $\frac{1}{2}$ are of dubious quality, as the roots of 3.7 included imaginary components (not shown). Further, the accuracy of this coverage data is limited by that of the parameter, Γ. Γ, the number of surface sites per unit area, is taken to be 10^{19} m^{-2}, as per [36, 37, 38], which is the approximate number of Pt atoms on a clean Pt(111) surface. This approximation is likely only accurate to an order of magnitude for polycrystalline Pt.

The isotherm with the cleanest shape is that at 605℃. The shape of this isotherm compares favorably with theoretical calculations. However, the lowest-temperature

[4]It is useful to remember that the standard error associated with the mean of a data series scales as $1/\sqrt{N}$, where N is the number of samples in the series; this is a consequence of the central limit theorem, and holds for any population of identically-distributed random variables with finite mean and variance. As such, accurate information may be obtained even from very noisy data simply by taking a sufficient number of data points. While the situation presented here is more complicated, the lesson of decreasing error with increasing sample size is still valid.

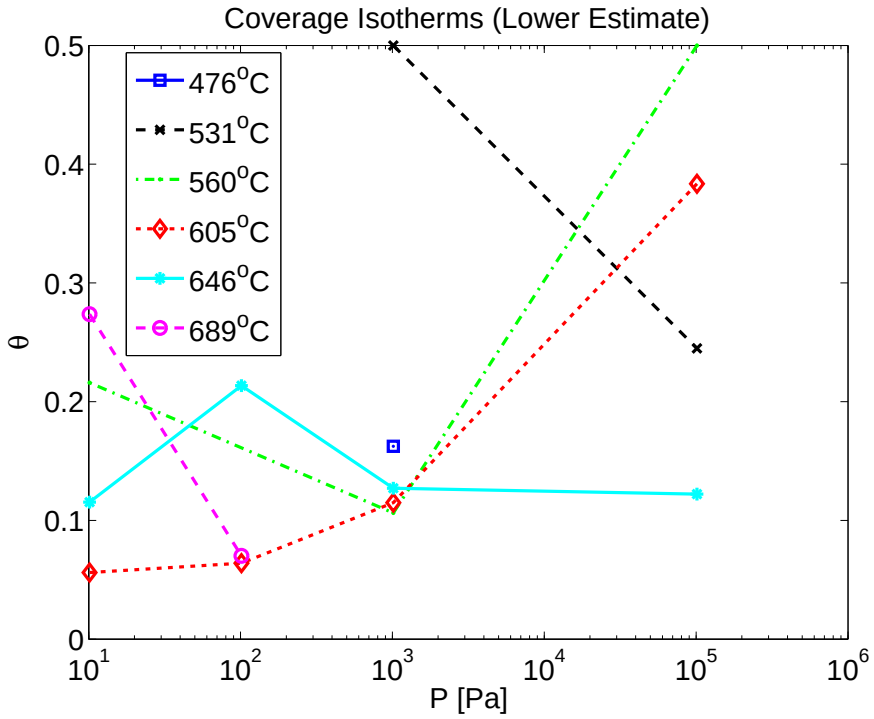

(a)

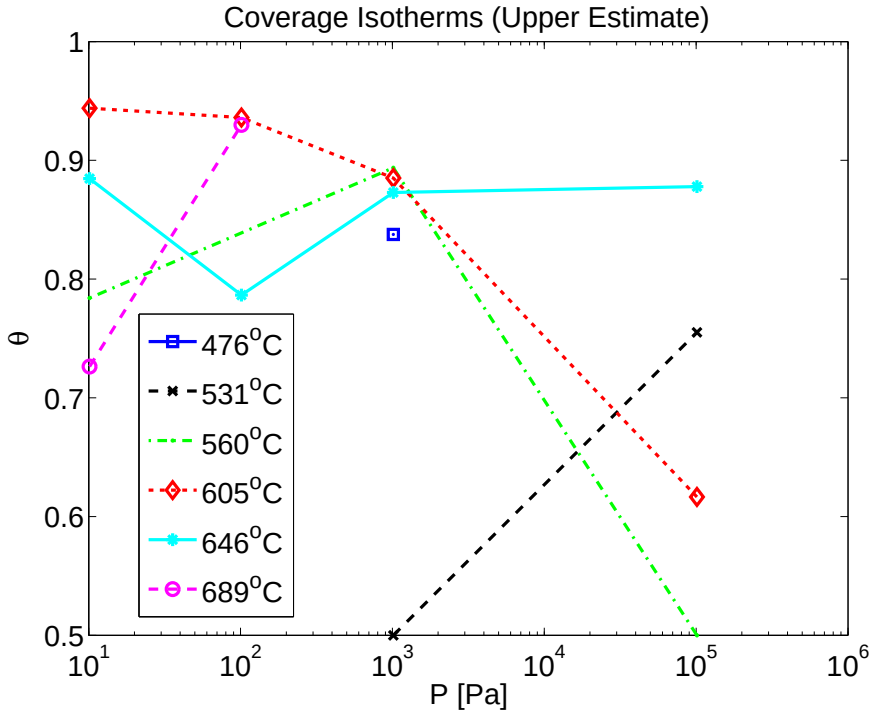

(b)

Figure 4-15: (a) Lower roots in 3.7. (b) Upper roots.

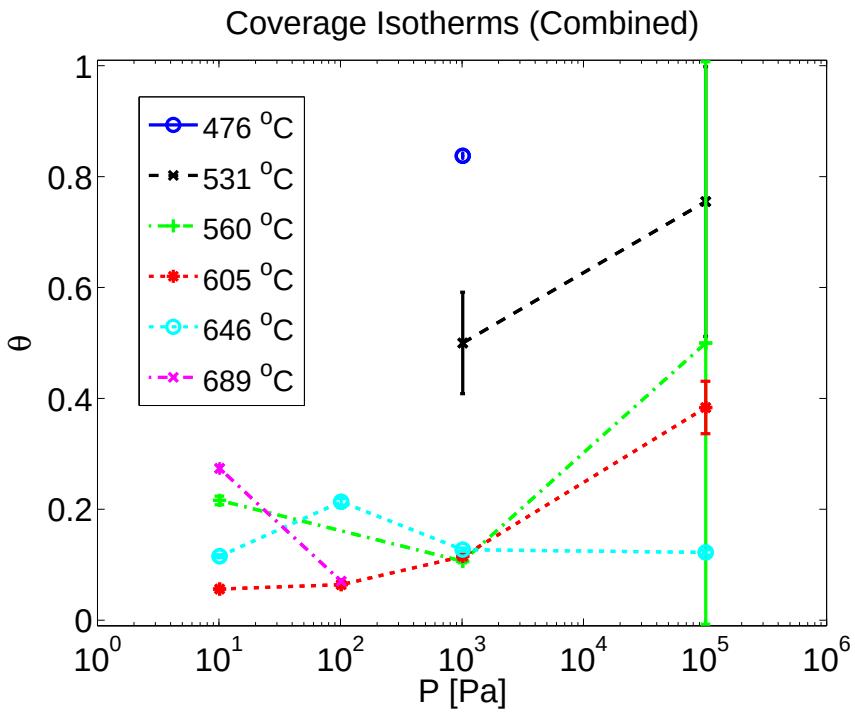

(a)

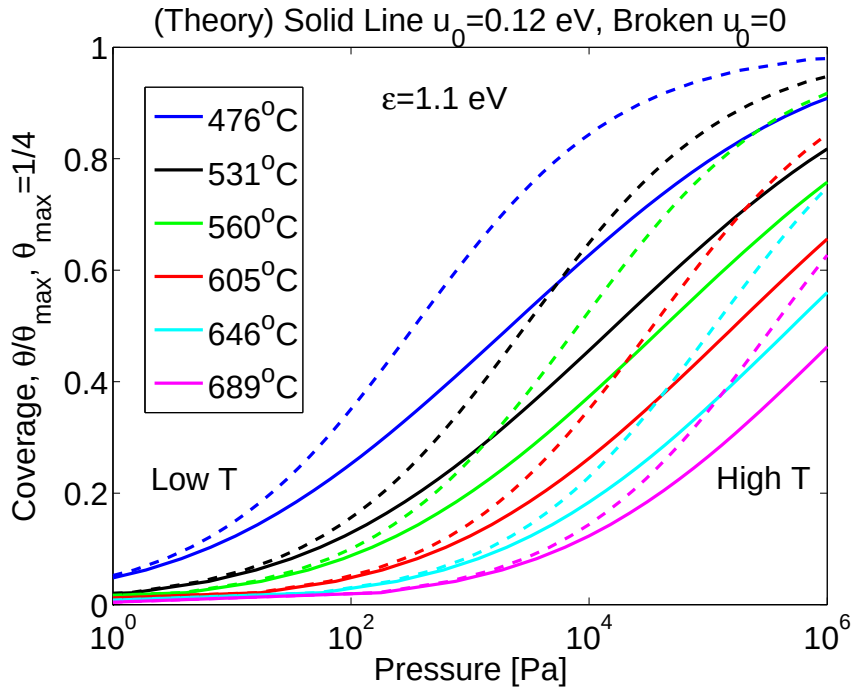

(b)

Figure 4-16: (a) Coverage isotherm **extracted** from impedance spectra, merged from data in Figure 4-15 by selecting the coverage values which produce an isotherm monotonically increasing with pressure. Temperatures shown are averages of each series; variation about each average is $< \pm 10$°C. (b) Coverage isotherm from **theory** shown in Figure 2-3 with repulsive interactions, $u_0 = 0.12$ eV, and chemisorption energy, $\epsilon = 1.1$ eV.

data point seems too high, and the high-temperature, low-pressure data points are arranged in an unexpected fashion. At these low pressures, it would be expected that the coverage has converged to nearly zero, suggesting that the observed scatter is just experimental error. It is possible that these data represent a more endemic problem in the interpretation of the EIS spectra. The higher temperature and pressure data do indicate the expected trend of increased coverage with increased pressure, all else equal, and decreased coverage with increased temperature, all else equal. Further, the data points in this range of temperatures and pressures sample nearly the entire coverage space, allowing for visualization of coverage effects on other parameters. A possible manifestation of this might be marked non-Arrhenius behavior in the diffusion coefficient for the highest-pressure isobar.

It is noteworthy that the simulated isotherms in Figure 2-3, for which the binding energy was taken to be $\epsilon = 1.6$ eV [56], fail to capture the extracted coverage isotherms with quantitative accuracy, and it would appear that the isotherms have been shifted between data and theory along the pressure scale by many orders of magnitude. However, the simulated isotherms in Figure 4-16 are in much better agreement with the data. These were generated using $\epsilon = 1.1$ eV [25], and the same repulsive lateral interaction energy, $u_0 = 0.12$ eV. Other combinations of ϵ and u_0 might also reproduce the data with reasonable accuracy. Further, impurities on the Pt surface that create a marked difference between the properties of the polycrystalline Pt used here and the Pt(111) surfaces used in some of the literature may account for discrepancies in the capacity of the surface to bind oxygen. Despite this, the simple mean field theory employed to derive the coverage isotherm performs surprisingly well.

4.3.6 Linearized Adsorption Rate

Section 4.3 discussed the extraction of the linearized adsorption rate, $\alpha = \gamma_3$, from impedance spectra. The parameter is the "stiffness" defining how fast the coverage value tends to restore itself in response to a perturbation about its equilibrium value, and considers only sorption processes. Because this parameter controls the location of the low-frequency corner frequency in spectra, it is perhaps the least difficult to

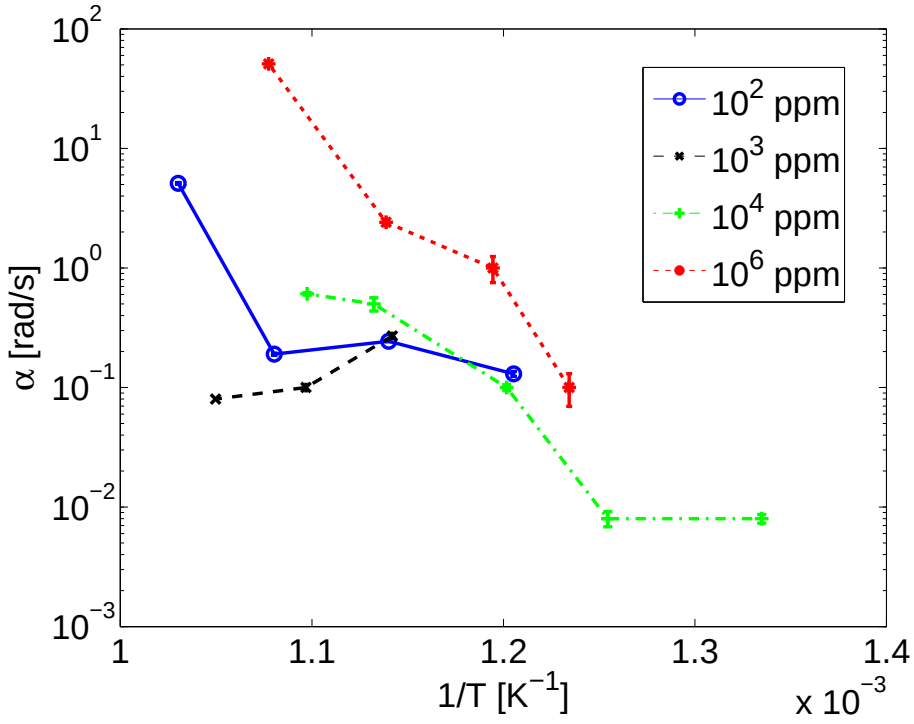

(a)

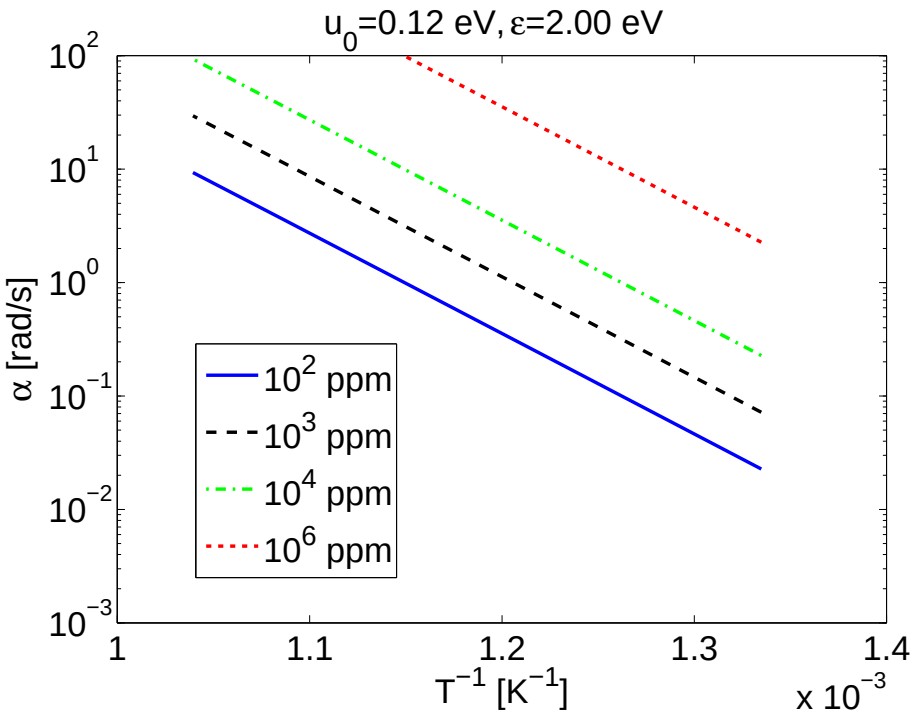

(b)

Figure 4-17: (a) **Extracted** linearized adsorption rate, α, isobars in an Arrhenius plot; (b) α as calculated in mean field theory **model**.

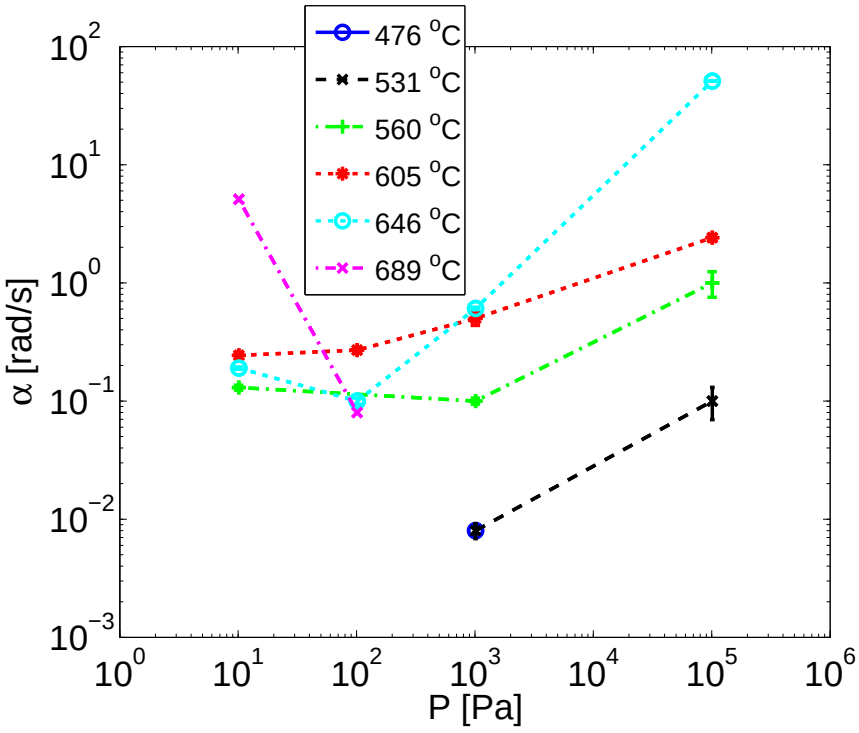

(a)

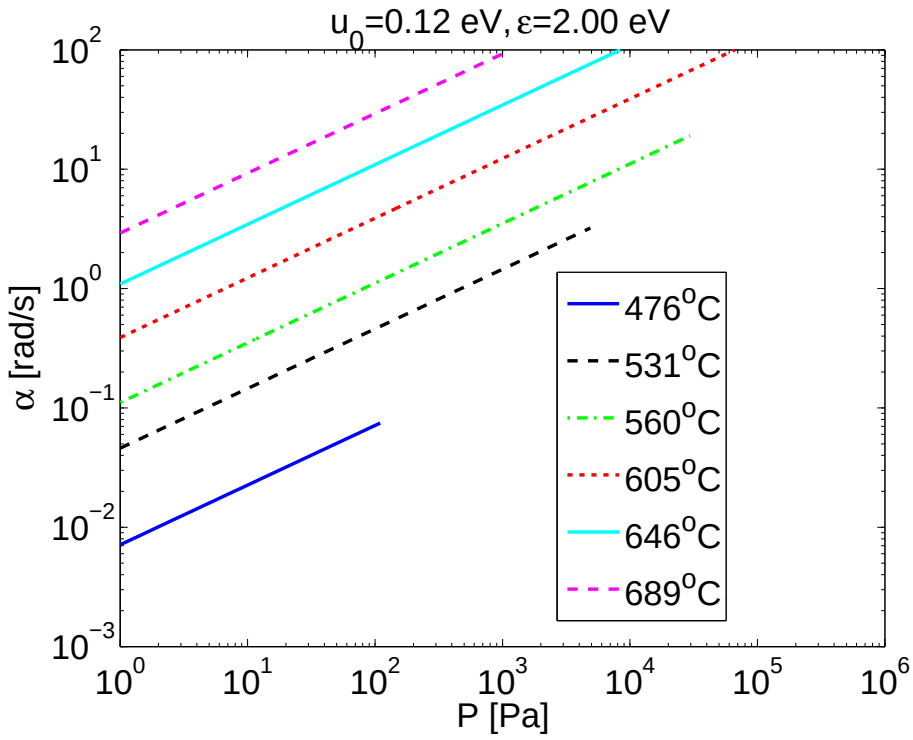

(b)

Figure 4-18: (a) **Extracted** linearized adsorption rate, α, isotherms against pressure; (b) α as calculated in mean field theory **model**.

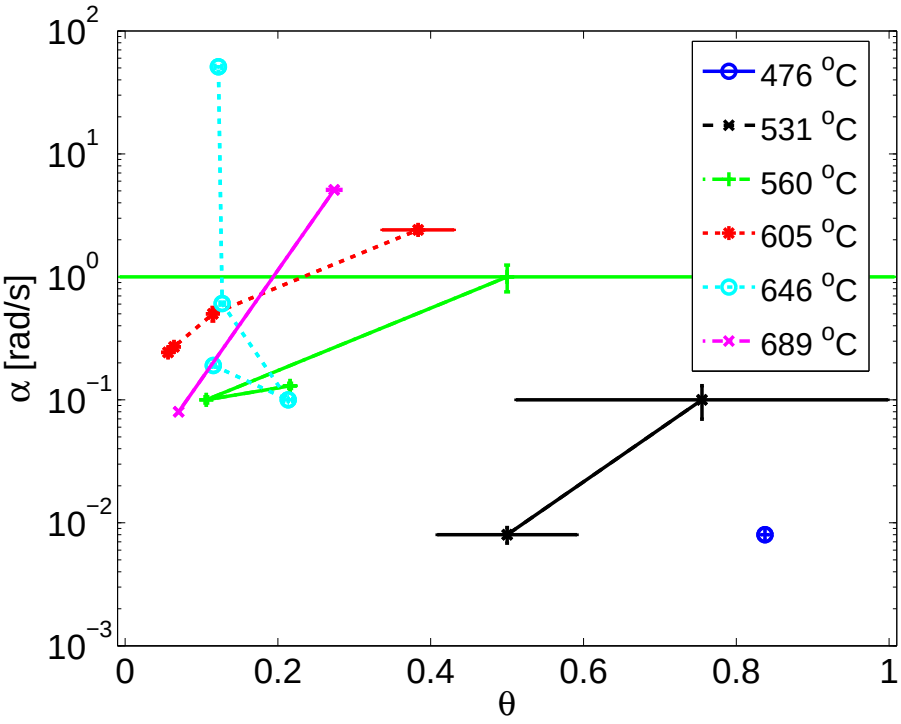

Figure 4-19: **Extracted** linearized adsorption rate, α, isotherms against coverage.

estimate by hand.

However, the extracted values of the adsorption rate seem hard to reconcile with the mean field theory model derived in Chapter 2 (see Equation C.48). In particular, the extracted adsorption rates are very slow so as to require a large binding energy in the MFT model to account for their order of magnitude. Further, the dependence on temperature seen in Figure 4-17 is confusing, especially for the 1000 ppm isobar. Figure 4-18 shows α against pressure alongside isotherms predicted from MFT, and Figure 4-19 shows these isotherms against the extracted coverage values. The higher-pressure data (10^4 ppm $\approx 10^3$ Pa) show α increasing with pressure, but lower pressures show a fairly flat curve against P. Such variations in α with respect to pressure would be more consistent with attractive, rather than repulsive, lateral interactions between adsorbates, as shown in Figure 2-1, though even allowing for this, the observed trends against P are not precisely reproduced.

Because the extraction of α depends largely on obtaining accurate low-frequency data, it is likely that the quality of extracted α values falls off as α becomes smaller,

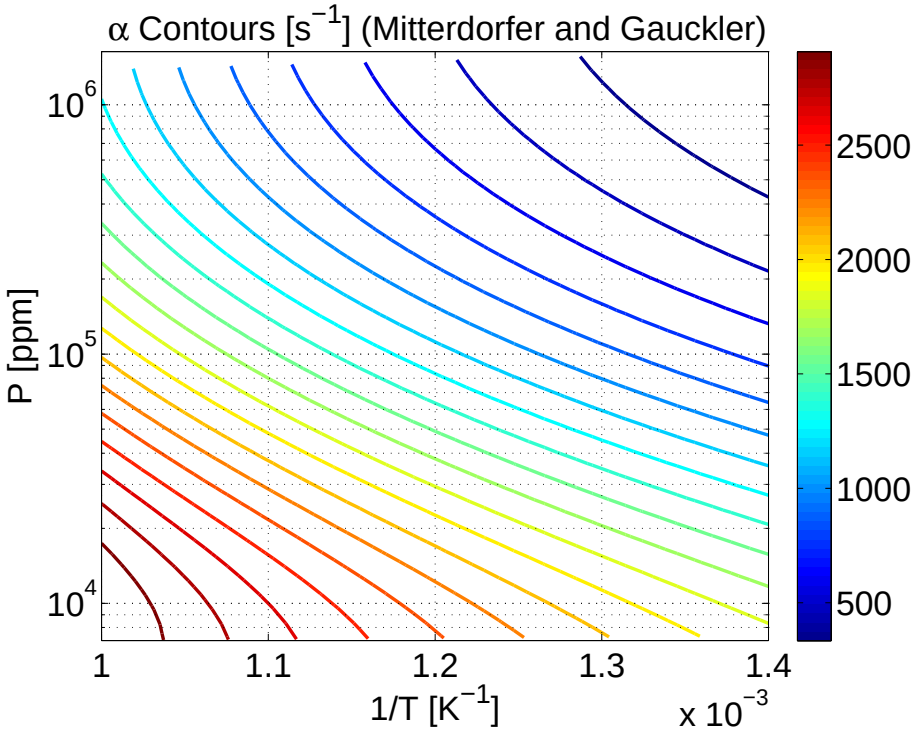

Figure 4-20: **Literature** value of linearized adsorption rate based on the work of Mitterdorfer and Gauckler in [37]. The values are found based on least-squares fits for adsorption and desorption rate constants, k_a and k_d, carried out in [37] that are valid for the coverage range, $0.2 < \theta < 0.75$ (implicit in the temperature and pressure range shown here). The correspondence between Mitterdorfer and Gauckler's k_a and k_d and the linearized adsorption rate of this work, α, is $\alpha = 2\Gamma\sqrt{k_a k_d P}$ (see Section C.10).

since observation may start to approach the time scale of sample degradation or other slow measurement drift processes at these lower-frequency measurements[5]. Examining Figures 4-17 and 4-18, trends do seem more reasonable for $\alpha > 0.1$ [rad/s]. However, this would be a very unfortunate degree of experimental error, essentially nullifying the validity of low-frequency information for a large portion of data.

It is of note that α and the lower-frequency corner frequencies found in these experiments were generally lower than those found in the work of Dr. Koc (see Section 2.4.4), even by as much as an order of magnitude. As the materials, processing, and fabrication in these two sets of experiments were basically the same, and as α is considered to be generally a function of only thermodynamic state and surface properties, this difference is hard to understand. It suggests that the actual Pt surfaces used in these experiments do differ from those used in earlier works, and that electrode surface properties are very sensitive to processing and fabrication details.

Comparing the values of α extracted here to those determined in Mitterdorfer and Gauckler's analysis for porous Pt shows an even greater disparity [37]. Figure 4-20 shows level set curves for α based on [37] for the range of temperatures visited in the present experiments and for pressures corresponding to $0.2 < \theta < 0.75$. Comparison with the α values extracted from the present work shows this work's values between one to four orders of magnitude *lower* than those recovered from [37]. Also, oddly, the data of Mitterdorfer and Gauckler would suggest that α monotonically *decreases* with increasing pressure, as their kinetic adsorption and desorption rate constants, k_a and k_d, are both reported to decrease monotonically with coverage, and $\alpha = 2\Gamma\sqrt{k_a k_d P}$ (see Section C.10 in the appendix). It would be expected that lateral interactions between adsorbates would tend to cause a falling trend against coverage in one parameter and a rising trend in the other. The authors address this inconsistency in a later work by proposing a precursor-mediated adsorption model [38].

[5]Section C.9 suggests that the low-frequency corner frequency is proportional to, but more than an order of magnitude smaller than, α.

4.3.7 Diffusion Coefficient

Figure 4-21a displays an Arrhenius plot of the diffusion coefficient, D, along several isobars. Diffusivity values typically fell between 2×10^{-2} and 2×10^{-7} cm^2/s. It is clear from the plot that (a) diffusivity depends strongly upon oxygen partial pressure and (b) that non-Arrhenius behavior is exhibited over a single isobar. Within the theoretical framework introduced in Chapter 2, these characteristics are attributed to coverage dependence in D.

For comparison, the same Arrhenius plot based upon theory and literature values has been displayed alongside that extracted from data. Extracted diffusivity values are typically much smaller than those obtained from theory. However, the extracted values are of comparable magnitude as in several experimental studies carried out on single-crystal Pt surfaces in high vacuum [4].

Figure 4-22 displays Arrhenius plots based upon empirical diffusion parameters obtained by von Oertzen et al. [53] for oxygen on Pt(110). This study is useful for comparison in particular because it involves long range surface transport at appreciable and varied coverages, and because the measurement technique is based on coarse-grained photographs and not on individual atom trajectories. However, marked differences are anticipated between diffusion on an anisotropic single-crystal Pt surface and the polycrystalline Pt employed here. Further, von Oertzen et al. took measurements at temperatures between 600 and 670 K (about 330 and 400°C); the empirical parameters they report may not be valid for extrapolation at the higher temperatures visited in this work. And it should be noted that the uncertainty cited by von Oertzen et al. results in three to four orders of magnitude difference in their diffusivity values; further, the scatter between all of the various Pt-O surface diffusion studies in the literature is large [4]. These cautionary remarks notwithstanding, the correspondence in magnitude between this study and that of von Oertzen is satisfying.

Already, the dependence of the diffusion coefficient on coverage may be inferred by the realization of marked non-Arrhenius behavior in the highest-pressure isobar, as predicted from analysis of the coverage isotherms. However, while the Arrhenius plot

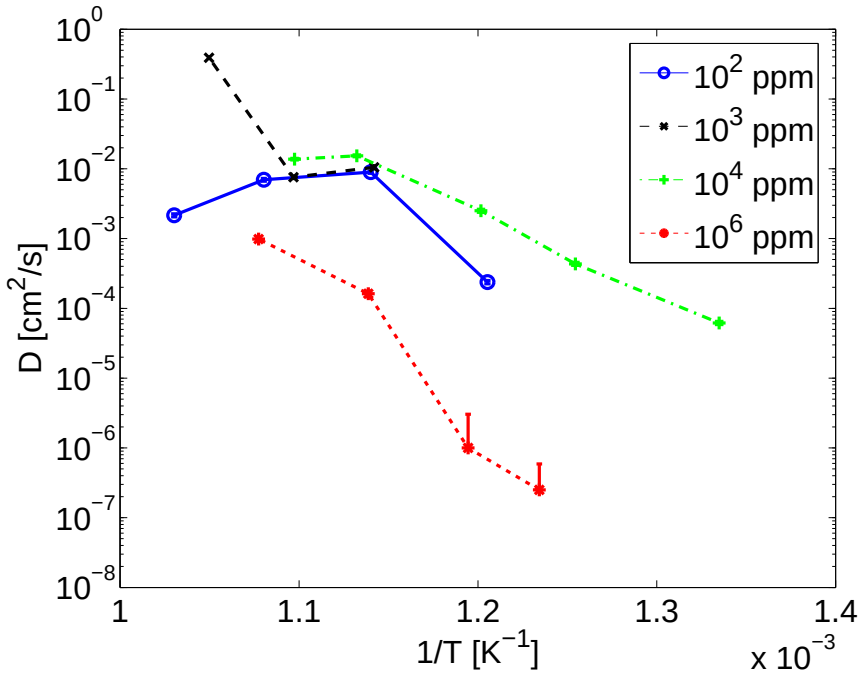

(a)
Data

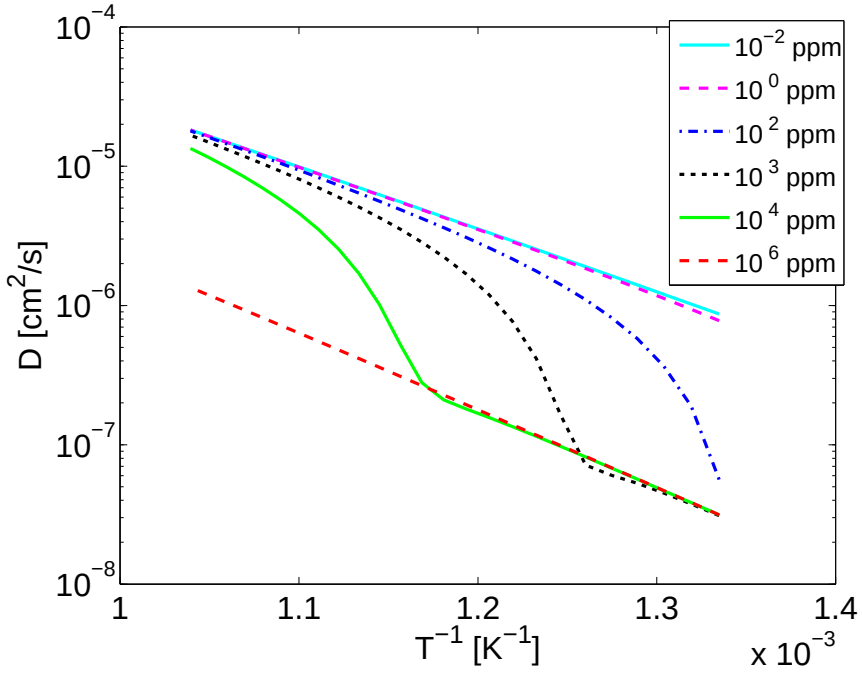

(b)
Sim.

Figure 4-21: (a) Arrhenius plot of several diffusion coefficient isobars **extracted** from impedance spectra according to the method outlined in Chapter 3. Exhibits non-Arrhenius behavior; this is expected. (b) Same plot as predicted from **theory** combined with literature data ($u_0 = -0.21$ eV; $\epsilon = 1.1$ eV).

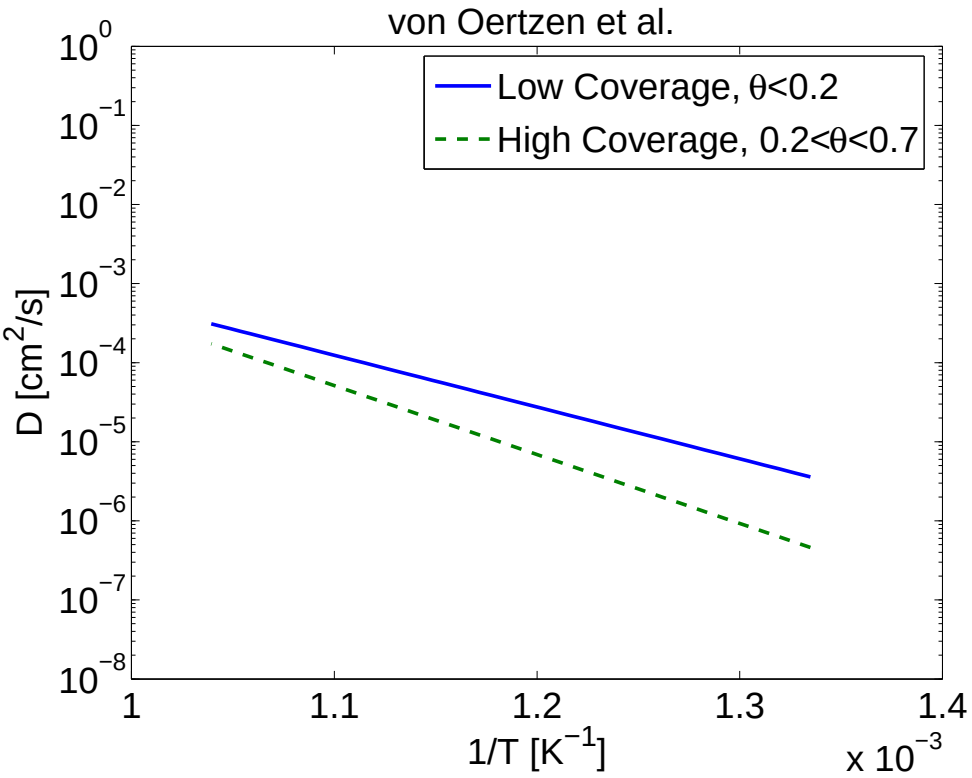

Figure 4-22: Empirical Arrhenius fits to data extracted by von Oertzen et al. [53]. The lines illustrate the data extracted at low and high coverages; there is a very large difference between these two cases.

is a classic tool for analysis of diffusivity data, isotherms displaying diffusivity against pressure and against coverage provide a more direct method of examining coverage dependence. These are shown in Figures 4-23 and 4-24. As before, the isotherms are, in fact, near isotherms, as the temperature varies by as much as 15°C along each series.

The data show a trend of generally decreasing diffusivity with increasing coverage. This is indicative of an attractive interaction between adsorbates according to the mean field theory proposed in Chapter 2. While the mean field theory model derived for the diffusion coefficient arrives at values of D with the same order of magnitude as those values extracted from the data, it is unable to capture the qualitative shape of the D isotherms. In particular, the mean field theory predicts a leveling off of the D isotherms at higher coverages, but this was not observed in the extracted D isotherms. However, as there is only limited high-coverage data from this work, it is very possible that this predicted trend is, in fact, accurate, and that the experimental analysis failed to capture it.

Once more, it is interesting to comment on the fact that the coverage isotherm seems to present evidence for repulsive interactions among adsorbates, while the diffusivity isotherms suggest attractive interactions. This dual personality of u_0 was discussed in Section 2.4.2. Most likely, it is a consequence of the oversimplification realized in the mean field theory schemes commonly used to handle lateral interactions, and a testament to the complexity of the adsorbate-adsorbate and adsorbate-surface relationship.

4.3.8 Utilization Length

The utilization length is calculated through its definition, $l_\delta = \sqrt{D/\alpha}$, where $\alpha = \gamma_3$. Figures 4-25, 4-26, and 4-27 show the results of these calculations in three different ways. Figure 4-25 does not display any consistent trend with respect to temperature. Figure 4-26, however, does show a tendency toward *decreasing* l_δ with *increasing* pressures above about 1000 Pa (10^4 ppm O_2), and weaker pressure dependence below 1000 Pa. The calculation may be checked for consistency by using other methods to

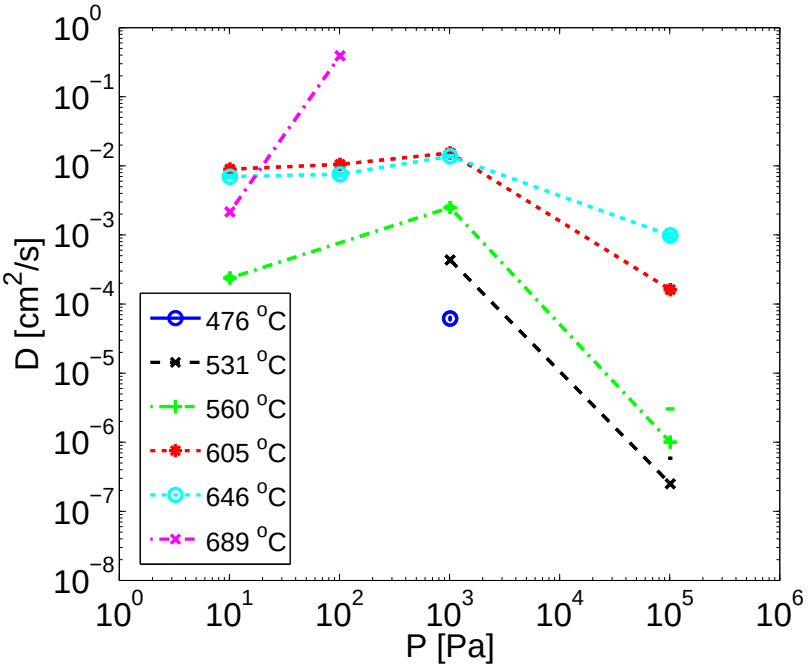

(a)
Data

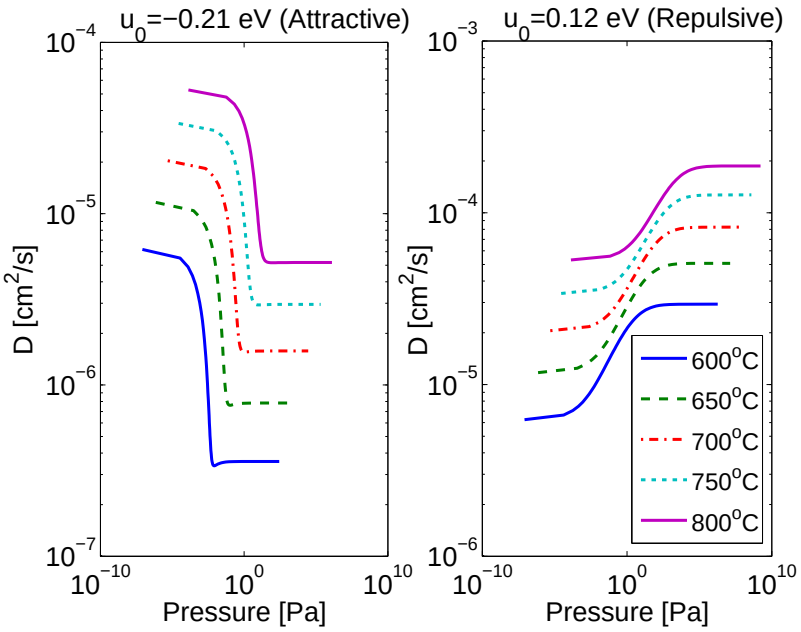

(b)
Sim.

Figure 4-23: Plot of diffusion against pressure. (a) Data. Standard deviation of temperature in pressure series indicated in legend as σ. (b) Simulated from theory using parameters from literature.

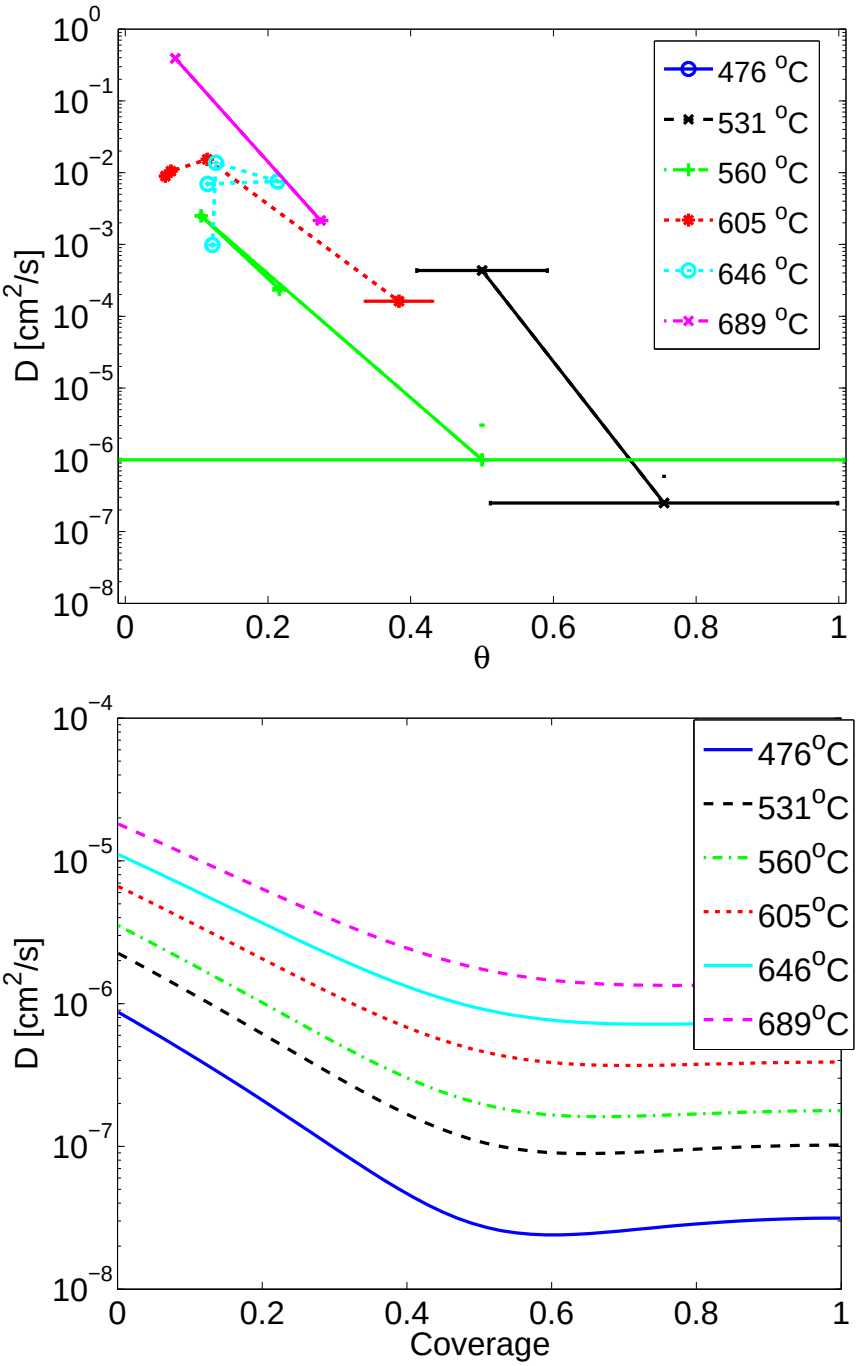

Figure 4-24: (a) Diffusivity vs. coverage as extracted from impedance spectra; (b) same plot as calculated from theory with $u_0 = -0.21$ eV.

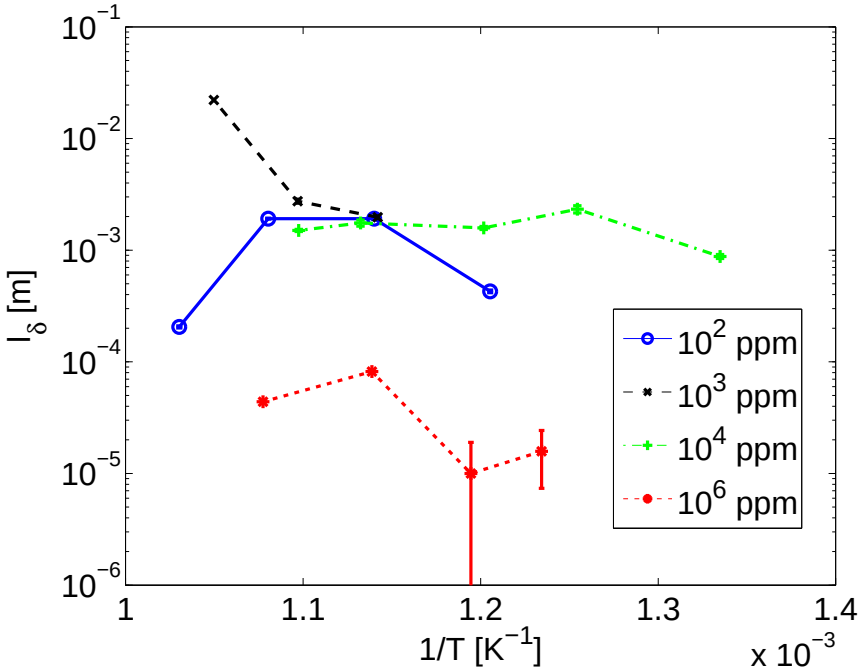

Figure 4-25: Arrhenius plots of utilization length isobars.

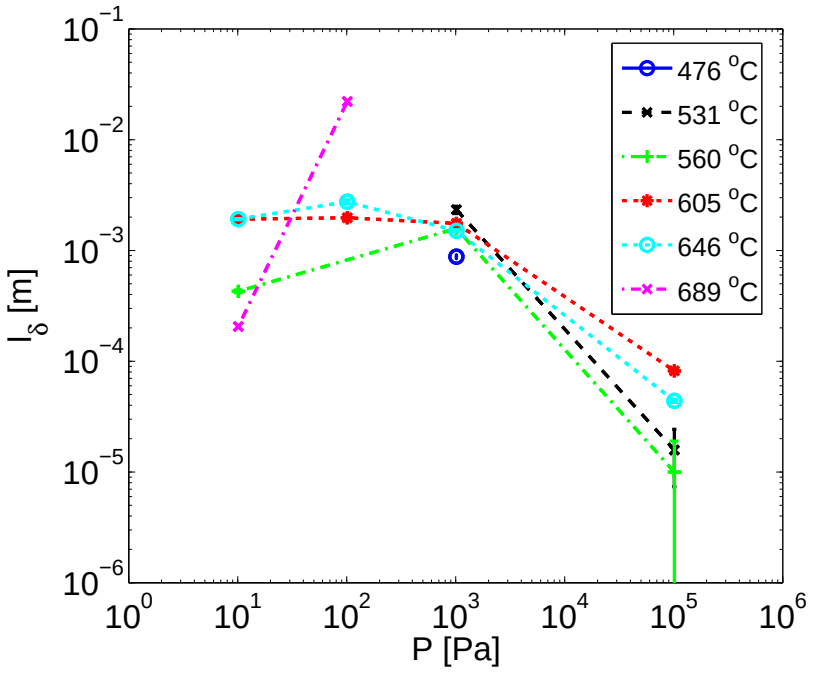

Figure 4-26: Utilization length against pressure, isotherms.

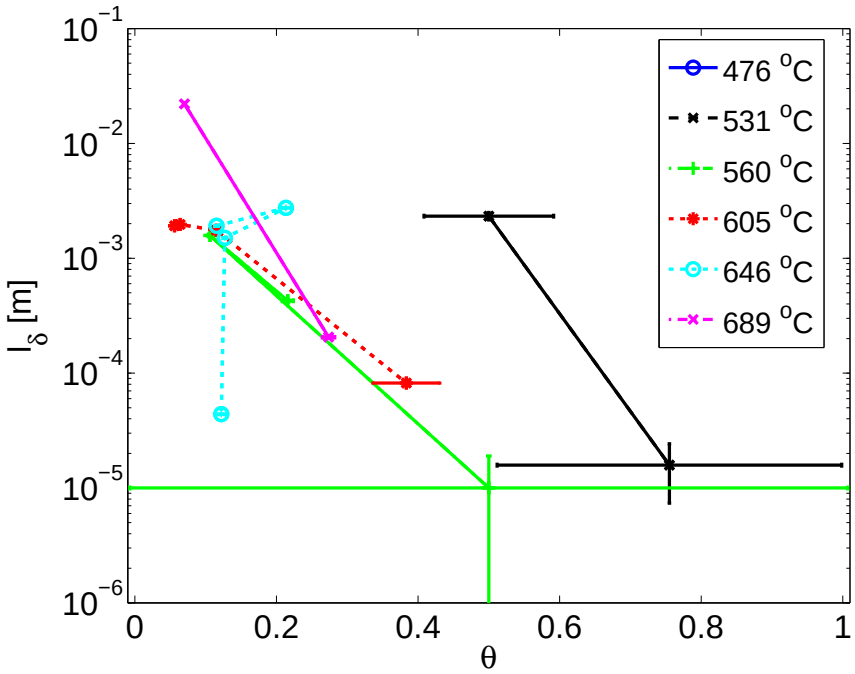

Figure 4-27: Utilization length against coverage, isotherms.

estimate l_δ. Section 4.3.3 mentioned that the utilization lengths were not clearly identified by visual inspection of the spectra; however, scaling analysis of low-frequency impedance intercepts shown in Figure 4-5 had suggested a scale for l_δ between 10 and 100 μm for a temperature of about 600℃ and oxygen partial pressures between 10^4 and 10^6 ppm. The value of l_δ extracted from EIS spectra for this temperature and these pressures fall within or close to this range, as seen in Figure 4-25. The 518℃ and 10^4 ppm data series in Figure 4-5 did not clearly indicate a scale length for l_δ; this, too, is consistent with the extracted value of about 2 mm for this temperature and pressure - a size out of the reach of the scaling analysis performed here. It is of note that for all but the 10^6 ppm data series, the utilization length is much larger than initially predicted by theory.

The coverage isotherms show coverage leveling off to a small value for the pressures below 1000 Pa. This observation suggests a strong correlation of l_δ to coverage, and indeed, this very correlation is appreciated in Figure 4-27. Curiously, the isotherm at 531℃ suddenly seems out of place in the l_δ vs. θ plot, where it lay on top of the other data series in 4-26. Further, two points from the 646℃ series also seem anomalous

given the rest of the data. Nonetheless, l_δ is seen to decrease rapidly with increasing coverage with fairly weak temperature dependence.

The discussion in 2.2.1 showed that α, and hence l_δ, is dependent on pressure not only through coverage, but also through the rate at which oxygen molecules impinge upon the surface. In fact, the expression for l_δ in 2.40 displays no explicit coverage dependence. As such, the behavior of l_δ is expected to be displayed most clearly when plotted in isotherms against pressure as in Figure 2-6 [6], which illustrated the model's $P^{-1/4}$ trend and the weaker, but still important, temperature dependence. However, the extracted values of l_δ do not conform to this picture. For higher pressures, the data follow pressure between $P^{-0.33}$ and $P^{-0.55}$, and again, lose this dependence at lower pressures. In fact, the absence of an explicit coverage dependence for l_δ in Equation 2.40 is probably a severe weakness of this first-order approximation, and the observed deviation from this prediction is likely genuine.

4.3.9 Considering Context-Specific Interactions

Given the aforementioned dichotomy of u_0 in the contexts of adsorption and diffusion, it might be helpful to allow different interaction energies for the diffusion and sorption models. Figure 4-28 shows what happens to the theoretical calculation of l_δ when this is done. Immediately, a new behavior can be seen in that the strict $P^{-1/4}$ dependence predicted earlier is lost in the intermediate pressure and coverage regime, reaching $P^{-1/2}$. The steeper dependence on P in this region is reminiscent of the higher-pressure trends in l_δ seen in the data in Figure 4-26, though the flat plateau in the data is still unaccounted for. Making this modification in the interaction energies (as well as the binding energy) has not changed the fact that the calculated values for l_δ are several orders of magnitude below the extracted values; indeed, the gap has widened as compared to that with Figure 2-6. Insofar as the mean field theory models have achieved at least order-of-magnitude accuracy in predicting the diffusion coefficient, D, the disparity ought to lie in the adsorption rate, where the theory

[6] in contrast to D, for which the behavior was expressed most clearly when plotted against coverage

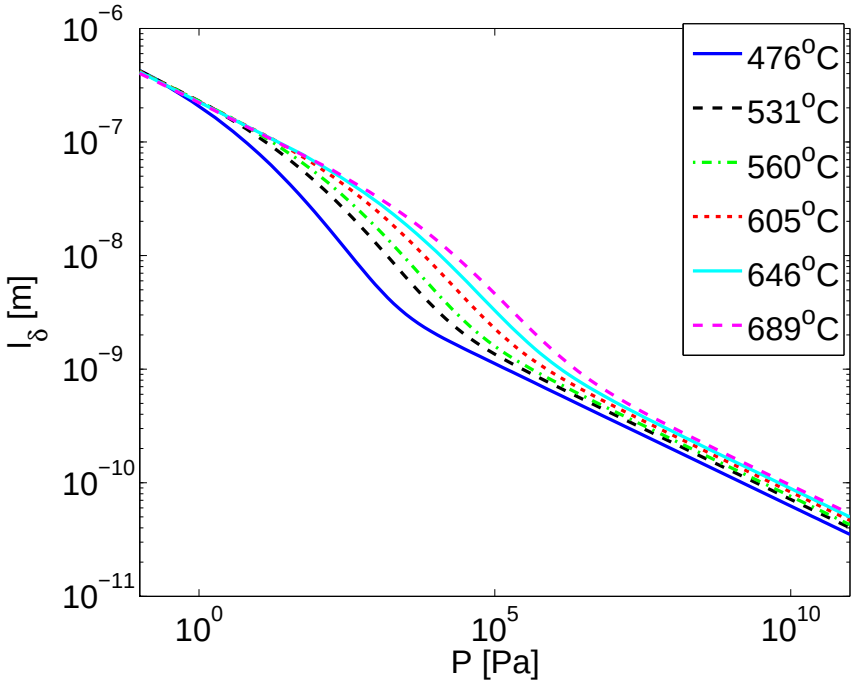

Figure 4-28: (**Theory**) Utilization length against pressure when ϵ is 1.1 eV and u_0 is 0.12 eV (repulsive) in the sorption/coverage calculations, but $u_0 = -0.21$ eV when appearing explicitly in the expressions for D. Note the loss of a constant $P^{-1/4}$ dependence.

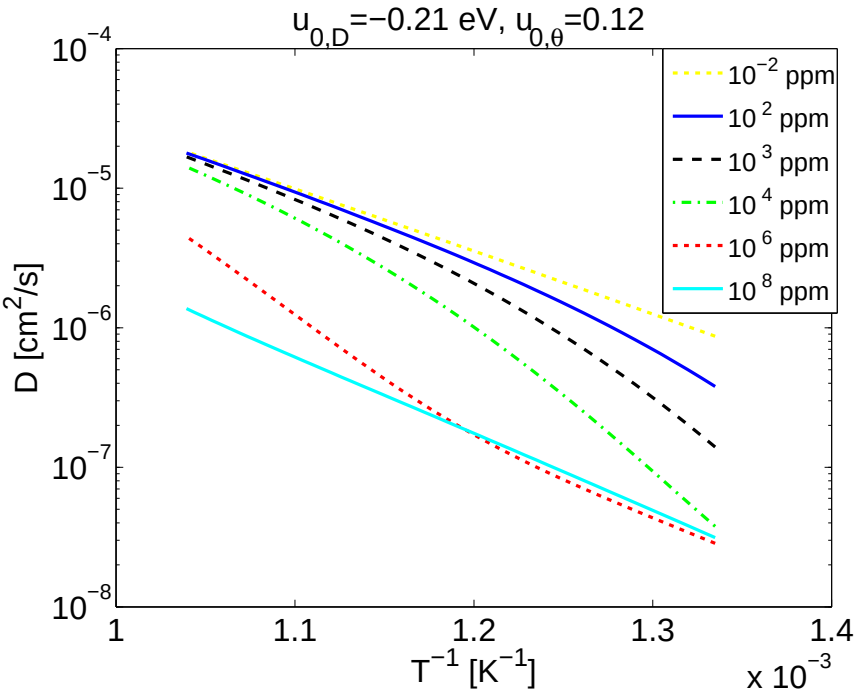

Figure 4-29: (**Theory**) Arrhenius plot of diffusivity isobars when different interaction energies are allowed in the diffusion and sorption contexts. Again, ϵ is 1.1 eV and u_0 is 0.12 eV (repulsive) in the sorption/coverage calculations, but $u_0 = -0.21$ eV when appearing explicitly in the expressions for D. Compare to 4-21b.

predicts much greater rates than actually measured[7].

The same idea might be applied to the calculation of D vs. θ; the result is shown in Figure 4-29 [8]. The highest and lowest pressures correspond to the asymptotes reached at the highest and lowest coverages; the experimental range of temperatures and pressures falls in between these limits.

4.4 Comments on Colimited Reaction

Section 2.6.4 included a discussion regarding the non-uniqueness of the impedance model derived for the cylindrical geometry. The primary message was that it is necessary, but not sufficient, to demonstrate an impedance spectrum which has the same qualitative shape (i.e. a 45° phase angle at high frequencies if real impedance offset is zeroed, and an alternatingly semicircular or Gerischer (teardrop) shape for a given state depending on electrode size) in order to argue for a colimited reaction. In response to this non-uniqueness, it was suggested that, by comparing quantitatively the physical parameters extracted from this model to those recorded in the literature, a conclusion regarding the colimited reaction might be made with more certainty. Since coverage isotherms are not widely available in the literature in a form convenient for comparison[9], focusing on the diffusion coefficient is a more straightforward way to seek verification of the colimiting hypothesis.

Insofar as demonstrating the expected qualitative forms of the derived cylindrical impedance model, the data do exhibit both cylindrical and teardrop shapes in the Nyquist plot, and they do show a 45° phase angle at high frequencies after zeroing the high-frequency real intercept. Yet the expected transition from semicircular to Gerischer-like spectra with an isolated increase of electrode radius was not observed for all data. As this transition is more a result of geometry than ORR mechanisms, and as its analog in the square electrode studies has already been observed (see Figure 2-7), its absence here is puzzling and potentially damning with regard to the validity

[7] In the impedance spectra, this corresponds to especially small low-frequency corner frequencies.
[8] Note that there is no change in the D vs. θ plot, as the coverage is *given* in this case.
[9] especially those not obtained from EIS spectra

of the postulated interpretation.

Nonetheless, most diffusivity values extracted from data seem reasonable relative literature values, as do at least several of the coverage isotherms. And there is some qualitative correspondence between these EIS-spectra-derived parameters and the first principles models created for them. Quantitative accuracy was achieved to some degree with regard to diffusivity values. Correspondence between theoretical and extracted coverage isotherms was achieved after choosing different energetics values, and particularly chemisorption binding energy, listed in the literature. But as the variation in binding energies in the literature is significant (see Appendix F), it is prudent to be skeptical of the quantitative accuracy of the mean field theory models. Utilization length values calculated from theory were far from those extracted from the data; the qualitative agreement between theory and experiment was improved somewhat by allowing for attractive lateral interactions in the diffusion context and repulsive in the adsorption context, but there was no improvement in quantitative accuracy after this change was employed. Discrepancies between data and model derive principally from differences in linearized adsorption rate, α.

In summary, the data do not present entirely conclusive evidence for the colimited model of the oxygen reduction reaction on Pt, but are consistent with this model in many respects. As such, it seems worthy to continue this line of research to move closer to a more definitive solution to the interesting puzzle of ORR processes on platinum.

4.5 Catalyst Design

Finally, this work leads to the contemplation of several valuable lessons for catalysis material selection. Firstly, this work suggests a tangible difference in the properties of the Pt thin film surface as compared to the porous Pt surface. As an example, Mitterdorfer and Gauckler report surface diffusivities in the range from 3×10^{-6} to 3×10^{-7} cm^2/s for oxygen over porous Pt for an electrode exposed to air at a

temperature of around 730℃ [10]. By contrast, this study of thin film Pt yields surface diffusivities from 3×10^{-7} cm^2/s at a temperature and oxygen partial pressure of 530℃ and 10^6 ppm to 10^{-2} cm^2/s for 650℃ and 10^4 ppm, and diffusivities even higher than this.

Along the same lines, Adler, analyzing the data of Mitterdorfer and Gauckler for the porous platinum/YSZ system, estimates a scale range for l_δ of 50 to 500 nm [2, 37]. Interestingly, using the same analysis scheme on data from Luerssen et al. for a thin film Pt electrode at 700℃ and high vacuum, Adler finds a much larger utilization length of 80 μm [2]. The estimates for l_δ determined in the present work range from 10 μm at 560℃ and 10^6 ppm to 2 mm and even greater at higher temperatures and lower pressures.

This line of inquiry suggests that surface diffusion is greatly enhanced on the dense, sputtered-on thin film Pt as compared to porous Pt, while the linearized net adsorption rate, α, is also reduced. It is hard to propose a mechanism for such a difference based on this study. Generically, however, the diffusion barrier would seem lower on the thin film surface; it can be speculated that this is due to the presence of favorable surface defects, or perhaps to a weaker binding between oxygen and the surface. Whereas a lower binding energy leads to a comparatively reduced coverage for the same temperature and pressure, we would expect a coverage isotherm for thin film Pt that is depressed downward from that of porous Pt should the latter of these two suggestions be true. Comparing the coverage isotherm shown in Figure 4-16a to those in the work of Mitterdorfer and Gauckler or Mizusaki for porous Pt, this, indeed, is seen to be the case[11]. A weaker binding energy might also be consistent with a reduced linearized net adsorption rate through a relatively smaller sticking coefficient, though the additional impact on coverage makes this statement more tenuous.

[10] However, it should be noted that, subsequent to the study carried out in [37], the authors greatly modified the model used to analyze their EIS data such that in their following publication, they assume a simple thermally-activated diffusivity and no longer attempt to extract the parameter from EIS data [37].

[11] [37, Fig. 12] and [38, Fig. 6], and for example, for 600℃ and 10^6 ppm, $\theta \approx 0.4 \pm 0.05$ here versus ≈ 0.6 in [38]. The analysis of Kishimoto et al. [23] of Mizusaki's work [39, 40] reports fully saturated coverage at all experimental temperatures visited here for pressures greater than or equal to 7×10^{-4} ppm.

Furthermore, recently, there has been much excitement in the catalysis community over attempts at an *ab initio* explanation of the Sabatier principle - a century-old heuristic due to Nobel laureate Paul Sabatier which holds that the catalytic activity of a surface is related to the binding energy of reactants to the surface, and that the binding energy should be strong enough to capture reacting particles while not too strong so as to prevent their eventual release. Notable work in this area using quantum perturbation theory as well as density functional theory calculations has been performed by Nørskov, Hammer, Mavrikakis, Hu, and others [8, 35]. The relevance to the present work is that in this study, energetics on the surface are demonstrated both theoretically and experimentally to depend not only upon the identity of the materials, but also upon the thermodynamic state that the surface is operated at. In particular, the stability of adsorbates on a surface is dependent upon coverage. As such, binding energies may be tuned not only by manipulating material compounds or growing material sets epitaxially in an interpolative manner [21], but also simply by varying the temperature and pressure to which the surface is exposed. Similarly, a surface which is selected because of good catalytic properties at one reference condition may not be as active under different conditions. As such, it is imperative to consider the operating state of the catalyst when making design decisions regarding material selection.

Chapter 5

Suggestions for Future Work

This iteration of EIS experiments of ORR on Pt represents an improvement over earlier versions, as discussed in the introduction. However, as always, the scheme might be revised to extend its utility and accuracy. With regard to the experimental method, I suggest a departure in the contact of the electrodes. Whereas the electrodes are already created via microfabrication, it seems natural to use thin microstrip conductors, perhaps also of Pt for simplicity, to carry voltage signals to electrodes. These conductors may be buried under a layer of polycrystalline YSZ such that only the circular electrodes are exposed to atmosphere. The dimensions of the electrodes (25 μm in diameter or larger) are such that the microelectrodes may be 5 μm while still being significantly smaller than the electrodes; at these sizes, adequate feature alignment ought to be achieved given the tolerances of the microfabrication equipment encountered in university laboratories. The microstrips may then run signals out to the periphery of the YSZ slide, perhaps to large contact pads. These pads may couple with a reusable cover plate with a mirrored-set of contact pads; this cover might fit over the sample slide so as to simultaneously contact the slide while preventing atmosphere from reaching the contact pads. In this way, only the electrodes contribute to the electrochemical reaction.

The entire system may be placed inside a tube furnace, for example, and an external switch connected to a Pt wire bundle running into the furnace might be used to select individual electrodes. Moreover, future "lab-on-a-chip" designs might

be created with high-temperature integrated circuitry to realize this switching feature on the chip itself, so that only a single pair of signal wires and a control wire need be run into the tube furnace. Such configurations might also include thermocouples nearby every electrode and other features to improve the accuracy and validity of data interpretation.

The benefit of this scheme is that it no longer requires microneedle contacts and the associated complex system of microadjusts and microscopes. Contacts are fabricated from the beginning, and will always be the same for any measurement so long as the integrity of the thin-films is maintained. The electrode is no longer damaged via contact for each measurement. And because all contacts are already in place, EIS experiments may be carried out more rapidly and in a more automated fashion, as there is no longer a need to readjust needles to contact different electrodes. Not only is this a more convenient and reliable scheme of operation for the researcher, but it also limits the time that a sample slide is exposed to the experimental environment. Chapter 3 demonstrated that prolonged exposure of sample slides to high temperatures resulted in damage of the thin film features; as such, the possibility of speeding up the measurement process is very important.

Beyond these design changes, an investigation into the effects of varying the materials at the electrode-electrolyte interface is needed. Experimental samples with a thin film of ceria on top of the YSZ slab were prepared for this work; however, analysis of these samples has yet to be carried out. It should appear in a future work. As the coverage isotherms and diffusivities are properties of the platinum surface, these parameters should not change if the substrate material is modified; their stationarity in the presence of this material swap would be very strong evidence in favor of the proposed colimited model. Indeed, the perturbation theory leading to the derived impedance expression rendered all parameters, $\boldsymbol{\gamma}$, independent of the identity of the electrolyte material with the exception of the charge transfer resistance, γ_1; as such, this model would predict the same Faradaic impedance spectra, but for a different high-frequency real-axis intercept, regardless of the substrate material. This is a readily testable hypothesis, and again its verification would lend credence to the

proposed ORR processes.

Finally, the uncertainties in extracted parameters quoted in Chapter 4 represented only uncertainties due to variations in measurements of impedance spectra (assuming a zero bias). There are many other sources of error which might be considered, including uncertainty in temperature, pressure, triple phase boundary length, signal frequencies, and the number of surface sites per unit area on the thin film platinum, among other system parameters.in was carried out to a there still remains significant work to be carried out with regard to error analysis. The theoretical framework for this effort was presented in Chapter 3; the implementation of this analysis remains to be completed. For accurate determination of the true error bars of the extracted diffusivities, utilization lengths, linearized adsorption rates, and coverages, this extended analysis is essential.

Chapter 6

Conclusion

This body of work was concerned with the oxygen reduction reaction on solid, thin film Pt over a YSZ substrate. By combining microfabrication techniques with electrochemical impedance spectroscopy, it sought to quantitatively characterize the reaction in order to verify that ORR is *colimited* by dissociative adsorption and surface diffusion of oxygen on the Pt surface. As byproducts of the work, coverage isotherms and diffusivity data were produced. These parameters, in themselves, are of value due to the fact that they are not widely available in the literature for the thermodynamic states probed here. And their analysis yields insight into the Pt-O system, the understanding of which is essential to the synthesis of new ORR catalyst materials. Finally, a body of theoretical work used to understand and interpret the physical processes was created; this effort serves as a bridge to connect EIS studies with other work in the literature regarding oxygen on Pt, as well as helping investigators to intuit and understand in a qualitative and, to some degree, quantitative way the physical processes at work in ORR.

Insofar as accomplishing the stated goal, the thesis provided some evidence in favor of the colimited nature of ORR on Pt, but the evidence was not conclusive. In order to truly validate the postulated thesis, further investigation is necessary. In particular, extended study into the effect of changing the solid electrolyte material, at least at the interface, would help to uniquely identify the proposed physical processes as those truly generating the observed EIS spectra. Further, whereas expected

scaling behavior was not observed in all data, it would be worthwhile to make another effort at acquiring measurements under better controlled conditions. If, after this repetition, the expected scaling behavior is still not observed, then there would be evidence against the proposed ORR processes. Lastly, several improvements to the experimental setup have been suggested which might improve the quality of the results.

Nonetheless, the thesis was able to demonstrate the expected forms of EIS spectra. Further, reasonable estimates of diffusivity, and, to a lesser extent, coverage isotherms, were generated, demonstrating the promise of the methodology to yield useful physical parameters that may be checked against other sources in the literature. Finally, an analysis of the O/thin-film-Pt/YSZ characterization provided insight into SOFC ORR catalyst design with regard to material selection and operation.

As promised, the work has certainly not solved the world's energy crisis! But it is, perhaps, an incremental step along the way.

Appendix A

List of Symbols

Table A.1: List of Symbols

Symbol	Name(s)	Description [Units]
α	linearized net adsorption rate	[s^{-1}]
β	inverse temperature	$1/(k_B T)$ - a convenience parameter ubiquitous in statistical mechanics.
$\boldsymbol{\gamma}$	parameters	vector of all cylindrical impedance model parameters; elements are indexed with right subscripts
Γ	surface site density	number of adsorption sites per unit surface area; for Pt(111), about 10^{19} [m^{-2}]
ϵ	binding energy	binding energy of a *single* oxygen atom with the surface *relative to a ground state in gaseous molecular oxygen* [eV]
θ	coverage	[unitless or monolayers]
$\bar{\theta}$	coverage	mean or equilibrium coverage [unitless or monolayers]
$\tilde{\theta}$	coverage	perturbation coverage [unitless or monolayers]
		Continued on next page

Symbol	Name(s)	Description [Units]
λ	thermal wavelength	defined through $h/\sqrt{2\pi m k_B T}$; roughly the average de Broglie wavelength and a ubiquitous normalization factor in statistical mechanics.
ξ		frequency-dependent length-scale of the decay in perturbations from the triple phase boundary [s^{-1}]
ω	angular frequency	[radians/s]
a_s	area per adsorption site	defined through $1/\Gamma$; for Pt(111), about 10^{-19} [m^2]
C_{dl}	double layer capacitance	more properly, interfacial capacitance - capacitances associated with interfacial area between Pt and YSZ [F, F/m^2]
C_e	electromagnetic capacitance	capacitance associated with electromagnetic coupling between electrode and counterelectrode [F, F/m^2]
D	diffusion coefficient, diffusivity	[cm^2/s] or [m^2/s]
EIS	Electrochemical Impedance Spectroscopy	
I	current	[A]
k_{-1}, k_1	backward, forward electrochemical rate constants	
k_B	Boltzmann constant	$\approx 1.381 \times 10^{-23}$ [J/K] $\approx 8.617 \times 10^{-5}$ [eV/K]
l_δ	utilization length	scale length over which perturbations in coverage decay from the triple phase boundary [m]
ℓ	triple phase boundary length	[m]

Continued on next page

Symbol	Name(s)	Description [Units]
$M_0()$	modified Bessel function	modified Bessel function of the first kind, zeroth order
$M_1()$	modified Bessel function	modified Bessel function of the first kind, first order
n		number of electrons exchanged per electrolyte-incorporation reaction (2 for ORR)
P	gaseous oxygen *partial pressure*	[atm or parts per million (ppm) or Pa] (1 atm = 10^6 ppm $\approx 10^5$ Pa)
q_e	electron charge	[C]
R_e	electrode radius	[m]
R_{hf}	high-frequency intercept	on a Nyquist plot (complex impedance plane), the point on the real axis toward which the impedance locus tends at very high frequencies [Ω]
R_{lf}	low-frequency intercept	on a Nyquist plot (complex impedance plane), the point on the real axis toward which the impedance locus tends at very low frequencies (dc limit) [Ω]
R_{ct}	charge transfer resistance	[Ω]
R_{ysz}	electrolyte resistance	impedance contribution associated with ohmic conduction of oxygen ions through the solid electrolyte
S	sticking coefficient	sometimes decomposed with a zero-coverage prefactor, S_0 [s^{-1} = Hz]
T	temperature	[°C or K]
u_0	interaction energy	defined through $u_0 \equiv \sum_{i=1}^{\Gamma} v(\mathbf{r}_i)$; interaction energy of an adsorbate with a full monolayer [eV]
$\tilde{v}$	phasor voltage	[V]
$\bar{v}$	polarization voltage	0 for the EIS experiments performed in this study [V]

Continued on next page

Symbol	Name(s)	Description [Units]
V	voltage	[V]
YSZ	yttria-stabilized zirconia	cubic zirconia; the solid electrolyte used in this study
z_v, $z_{v,ads}$	vibrational partition function	local, single-site, vibrational partition function
$z_{v,r}$, $z_{v,r,gas}$	single-molecule partition function	
Z	electrochemical impedance partition function	complex-valued [Ω] in the statistical mechanics context.
Z_{cyl}	cylindrical impedance	impedance relation derived for cylindrically-shaped, solid, blocking electrodes [Ω]
Z_G	Gerischer impedance element	impedance element corresponding to semi-infinite medium
Z_i		imaginary component of impedance [Ω]
Z_r		real component of impedance [Ω]

Appendix B

Selected Derivations in Statistical Mechanics

B.1 Introduction

The purpose of this appendix is to catalogue a number of the more involved derivations of the present work. Many of the formulations below derive from statistical mechanics. Some knowledge of statistical mechanics is assumed, but brief explanations are included for readers unfamiliar or long-separated from the field. A fun textbook on this subject is that of the MIT Physics Department's Professor Mehran Kardar [22], but there are many other excellent references, among them one by Richard Feynman.

B.2 Coverage Isotherm

In deriving the coverage isotherm, the program will be to first calculate the partition function for adsorbates on the surface, and then to use the partition function to obtain the grand partition function. The grand partition function leads to the chemical potential, a result that shall be used again for the diffusion coefficient. Next, imposing equilibrium conditions forces the chemical potential of the surface species to be related to that of the gas phase oxygen.

Let us write a Hamiltonian for N adsorbates:

$$\mathcal{H} = \sum_{i=1}^{N} (-\epsilon + u_{vib}) + \sum_{i<j} v\left(\mathbf{r}_i - \mathbf{r}_j\right) \tag{B.1}$$

where ϵ is the adsorption energy per adsorbate (positive when a site on the surface is more stable occupied than empty), u_{vib} is the energy associated with vibrations, $\{\mathbf{r}_i\}$ are the coordinates of all adsorbates, and $v(\mathbf{r}_i - \mathbf{r}_j)$ is a pairwise potential between the i^{th} and j^{th} particles. N is the number of adsorbates on the surface, so that $\theta = N/\Gamma$. It will be assumed throughout that adsorbates are point particles - in the physical system under study, these particles correspond to the oxygen anions. We do not consider the added rotational degrees of freedom of molecular adsorbates; while the molecular adsorbate is an important precursor in the adsorption/dissociation step, there is ample evidence that molecular precursors are not long-lived on the surface at the elevated temperatures relevant to these experiments [17, 18, 54].

The non-interacting portion of the Hamiltonian (those terms with no coupling between adsorbates) may be written as

$$\mathcal{H}_0 = \sum_{i=1}^{N} (-\epsilon + u_{vib}) \tag{B.2}$$

Assuming uniformity over the surface[1], this becomes

$$\mathcal{H}_0 = -N\epsilon + N u_{vib}. \tag{B.3}$$

Statistical mechanical quantities may be evaluated exactly when the elements of the system are decoupled (do not interact with one another). However, interactions are the rule rather than the exception, and useful approximation schemes are a necessary tool. One of the simplest schemes is the *mean field* approximation, wherein the particle distribution is assumed to be unperturbed from the uniform distribution of

[1] certainly, the polycrystalline surface is not uniform at the grain-size scale, or perhaps even below this, but it is hoped that uniform average quantities arise from polycrystallinity over the scales of interest

the non-interacting system. The interaction energy resulting from this approximation is labelled as U_0, so that,

$$\mathcal{H} = \mathcal{H}_0 + U \approx \mathcal{H}_0 + U_0, \tag{B.4}$$

To evaluate U_0, we first start with the definition of U,

$$U = \sum_{i=1}^{\Gamma} \sum_{j<i}^{i-1} \sigma_i \sigma_j v\left(\mathbf{r}_i - \mathbf{r}_j\right) \tag{B.5}$$

The sum is now over *sites*, as opposed to adparticles. As such, we now require an occupation variable, σ_i, at each site, zero when a site is empty and unity when it is occupied. Also, the $\{\mathbf{r}_i\}$ are now the coordinates of the surface sites, as opposed to the adsorbates. The expected value of U is then

$$\langle U \rangle = \sum_{i=1}^{\Gamma} \sum_{j<i}^{i-1} \langle \sigma_i \sigma_j \rangle v\left(\mathbf{r}_i - \mathbf{r}_j\right) \tag{B.6}$$

The mean field approximation takes the occupation of one site as approximately independent of that of all other sites; then

$$\langle \sigma_i \sigma_j \rangle \approx \langle \sigma_i \rangle \langle \sigma_j \rangle \approx \langle (\sigma_i) \rangle^2 \tag{B.7}$$

But the occupation probability of a single site is exactly the coverage, $\langle sigma_i \rangle = \theta = N/\Gamma$. We then define U_0 as an approximation to $\langle U \rangle$,

$$U_0 \equiv \left(\frac{N}{\Gamma}\right)^2 \sum_{i=1}^{\Gamma} \sum_{j=1}^{i-1} v(\mathbf{r}_i - \mathbf{r}_j) = \left(\frac{N^2}{2\Gamma}\right) u_0, \tag{B.8}$$

where

$$u_0 \equiv \sum_{i=1}^{\Gamma} v(\mathbf{r}_i), \tag{B.9}$$

and a spherical (circular) symmetry has been assumed for $v(\mathbf{r}) = v(|\mathbf{r}|)$. [2]

The next step is to calculate the partition function, Z - the normalization constant

[2]Note: when u_0 is positive, the interaction between adsorbates is repulsive; when negative, it is attractive.

for configuration probabilities in the canonical ensemble[3]. This is written as

$$Z = \mathrm{tr}\left\{e^{-\beta\mathcal{H}}\right\}, \tag{B.10}$$

where, for convenience, $\beta \equiv \frac{1}{k_B T}$, and tr$\{\}$ (trace) is used here a shorthand for summing over all the allowed configurations of the system. Now, with the mean field approximation, Z becomes

$$Z \approx \mathrm{tr}\left\{e^{-\beta\mathcal{H}_0 - \beta U_0}\right\}, \tag{B.11}$$

First, note that if there are N particles on the surface and Γ available sites, then there are $\begin{pmatrix} \Gamma \\ N \end{pmatrix}$ ways to arrange these particles on the surface. While in general, we would expect some variation in the Hamiltonian from each of these configurations, the mean field approximation ignores such variation. As such,

$$Z \approx \begin{pmatrix} \Gamma \\ N \end{pmatrix} e^{N\beta\epsilon - \beta N^2 u_0/(2\Gamma)} \mathrm{tr}\left\{e^{-\beta N u_{vib}}\right\}_{vib}, \tag{B.12}$$

where the notation, tr$\{\}_{vib}$ refers to the sums (or integrations) over all allowed vibrational states. For the moment, the precise details of the vibrations will be put aside, and we will simply label $(z_v)^N \equiv \mathrm{tr}\left\{e^{-\beta N u_{vib}}\right\}_{vib}$, where z_v represents the local (single-site) vibrational partition function. Then, all together, the partition function is written as

$$Z \approx \begin{pmatrix} \Gamma \\ N \end{pmatrix} e^{N\beta\epsilon - \beta N^2 u_0/(2\Gamma)} (z_v)^N. \tag{B.13}$$

Next, for convenience, we'll introduce

$$x \equiv \beta\left[\epsilon + \ln\left(z_v\right)/\beta\right]. \tag{B.14}$$

[3]The partition function is a fundamental quantity in statistical mechanics, containing information about the Boltzmann weights for all allowed configurations. Thermodynamic quantities are obtained from its logarithm (free energy) and various derivatives (entropy, internal energy, etc.). Later, we'll see the grand partition function, which plays the same role for the grand canonical ensemble that the partition function does for the canonical ensemble.

Now,

$$\begin{pmatrix} \Gamma \\ N \end{pmatrix} = \frac{\Gamma!}{N!(\Gamma - N)!}, \tag{B.15}$$

so that

$$Z = \exp\left[-\beta\frac{N^2 u_0}{2\Gamma} + xN + \ln\left(\frac{\Gamma!}{N!(\Gamma - N)!}\right)\right]. \tag{B.16}$$

Introducing the Sterling approximation for the factorial,

$$\ln(A!) \approx A\ln(A) + A \tag{B.17}$$

when A is large, we now approximate

$$\begin{pmatrix} \Gamma \\ N \end{pmatrix} \approx \Gamma\ln(\Gamma) - N\ln(N) - (\Gamma - N)\ln(\Gamma - N). \tag{B.18}$$

Then

$$Z \approx \exp\left[-\beta\frac{N^2 u_0}{2\Gamma} + xN + \Gamma\ln(\Gamma) - N\ln(N) - (\Gamma - N)\ln(\Gamma - N)\right]. \tag{B.19}$$

We now have a working approximation for the partition function, Z; this allows us to calculate the free energy, $F = -k_B T\ln(Z)$, the internal energy, $\langle\mathcal{H}\rangle = -\partial\ln(Z)/\partial\beta$, the entropy, $S = -\partial F/\partial T|_N$, and various other quantities. For now, we will concern ourselves with the grand partition function, which is found from

$$Q = \sum_{N=0}^{\Gamma} e^{\beta\mu N} Z, \tag{B.20}$$

where μ is the chemical potential. Now, Q can be expressed as

$$Q = \sum_{N=0}^{\Gamma} \exp\left[\beta\mu N - \beta\frac{N^2 u_0}{2\Gamma} + xN + \Gamma\ln(\Gamma) - N\ln(N) - (\Gamma - N)\ln(\Gamma - N)\right]. \tag{B.21}$$

This sum of exponentials may be approximated with its largest term, so we will

maximize the argument to the exponential in the summation index, N:

$$0 = \frac{\partial}{\partial N}\left[\beta\mu N - \beta\frac{N^2 u_0}{2\Gamma} + xN + \Gamma\ln(\Gamma) - N\ln(N) - (\Gamma - N)\ln(\Gamma - N)\right], \quad \text{(B.22)}$$

from which results the following constraint,

$$\frac{\theta}{1-\theta} = e^x e^{\beta\mu} e^{-\beta\theta u_0}, \quad \text{(B.23)}$$

where we have recognized $N/\Gamma = \theta$. The quantity, e^x, is

$$e^x = z_v e^{\beta\epsilon}, \quad \text{(B.24)}$$

so we can write

$$\frac{\theta}{1-\theta} = z_v e^{\beta\mu} e^{\beta(\epsilon - \theta u_0)}, \quad \text{(B.25)}$$

A brief summary is in order. Starting with a Hamiltonian, we utilized a mean field approximation to account for interactions between adsorbates. This, in conjunction with the Sterling approximation, was used to obtain an expression for the partition function, which, in turn, was used to evaluate the grand partition function. We realized that the sum of exponentials defining the grand partition function might be approximated by its largest term, so we maximized the argument of the exponential with respect to the total number of adsorbates on the surface, N. This gave us an expression relating coverage to ϵ, u_0, μ, and z_v. It may seem odd to obtain the key relation as a side effect of calculating another quantity, Q, whose value we are not interested in at the present. In fact, what we have done is to select the value of coverage which gives the correct grand partition function under the constraint that the chemical potential is held constant. By allowing the surface to reach equilibrium with gaseous oxygen above, this condition is physically realized, and we may have some faith in the result just obtained.

The last step is to establish this equilibrium with the diatomic oxygen gas. The equilibrium condition is given from

$$\mu_{gas} = 2\mu_{adsorbates}, \tag{B.26}$$

since the diatomic gas dissociates into two adsorbates. The chemical potential for a classical dilute (non-interacting) monatomic gas is

$$\mu_{monatomic} = -k_B T \ln\left(\frac{k_B T}{P\lambda^3}\right), \tag{B.27}$$

where P is the gas pressure, $\lambda = h/\sqrt{2\pi m k_B T}$ is the thermal wavelength of the gas with m the mass of each gas constituent and h Planck's constant [22]. We will account for molecular (rotational and vibrational) degrees of freedom for the diatomic gas on a quantum level with

$$\mu_{gas} = -k_B T \ln\left(z_{v,r}\frac{k_B T}{P\lambda^3}\right), \tag{B.28}$$

where $z_{v,r}$ is the single-molecule partition function. That we can do this follows from the same set of steps which led to the introduction of z_v for the adsorbates (see B.25). From this follows the coverage isotherm,

$$\boxed{\left(\frac{\theta}{1-\theta}e^{\beta u_0 \theta}\right)^2 = e^{2\beta\epsilon}\frac{z_{v,ads}^2}{z_{v,r,gas}}\frac{P\lambda^3}{k_B T}}. \tag{B.29}$$

This style of isotherm is sometimes called the Frumkin isotherm.

B.29 may be compared with a similar expression found in [25]. It is also instructive to compare to the Langmuir isotherm, which might be written in the formalism of Mitterdorfer and Gauckler [36, 37] as,

$$\left(\frac{\theta}{1-\theta}\right)^2 = \frac{k_a}{k_d}P, \tag{B.30}$$

with k_a the adsorption rate constant and k_d the desorption rate constant. B.30 explicitly reproduces the correct dependence of coverage on the experimental state variable, P; temperature dependence is masked inside the phenomenological rate constants. Our isotherm reduces to the Langmuir situation when there is no interaction between adsorbates, or $u_0 = 0$. It should be noted that the Langmuir isotherm shown

above was obtained from a very different method involving kinetic equations from a model adsorption-desorption reaction[4].

B.2.1 Single-Element Partition Functions, $z_{v,ads}$ and $z_{v,r,gas}$

The quantities, $z_{v,ads}$ and $z_{v,r,gas}$, account for the additional degrees of freedom associated with vibrational and (in the case of the molecular gas) rotational degrees of freedom of the adsorbate and the diatomic oxygen gas. In the case of the adsorbate, the vibrations here refer to oscillations on and out of the Pt surface plane; the diatomic gas molecules have vibrational modes along their longitudinal axis. As such, we can attribute vibrational contributions for both gas molecules and adsorbates to strong, molecular interactions (envisioning the chemisorption of oxygen onto Pt as a quasimolecular bond). Presently, we'll treat these degrees of freedom in a standard manner [22].

We start with a Hamiltonian for a classical simple harmonic oscillator,

$$\mathcal{H}_v^c = \sum_{i=1}^{d} \left[\frac{1}{2} m(\omega_i r_i)^2 + \frac{p_i^2}{2m} \right], \tag{B.31}$$

where p is momentum, ω_i is the angular vibrational frequency of the oscillator in the i direction, r_i is the i$^t h$ position component, and d is the number of dimensions in which the simple harmonic oscillator vibrates[5]. The partition function is then calculated directly as

[4]Historically, it was from this kinetic standpoint that Langmuir originally derived the isotherm in 1916 [28], as discussed in 2.2.1.

[5]For oxygen on the the Pt surface, $d = 3$ - two in-plane modes and one out-of-plane mode

$$
\begin{aligned}
z_v &= \int\int \frac{\mathrm{d}^3 r \mathrm{d}^3 p}{h^3} e^{-\beta \mathcal{H}} \\
&= \int\int \frac{\mathrm{d}^d r \mathrm{d}^d p}{h^d} \exp\left(-\beta \sum_{i=1}^{d} \left[\frac{1}{2} m(\omega_i r_i)^2 + \frac{p_i^2}{2m}\right]\right) \\
&= \frac{1}{\lambda^d} \left(\sqrt{\frac{2\pi}{m\beta}}\right) \prod_{i=1} d\omega_i^{-1} \\
&= \prod_{i=1} d\left(\frac{k_B T}{\hbar \omega_i}\right)
\end{aligned}
\tag{B.32}
$$

where $\hbar \equiv h/2\pi$.

In the quantum mechanical treatment, the energy levels of the simple harmonic oscillator are quantized. Assuming that we can quantize each vibrational mode *independently*, the resulting Hamiltonian is

$$
\mathcal{H}_v^q = \sum_{i=1}^{d} \hbar \omega_i \left(n + \frac{1}{2}\right) \tag{B.33}
$$

If each vibrational mode occurs with probability proportional to its Boltzmann weight [22],

$$
\begin{aligned}
z_v^q &= \sum_{n=0}^{\infty} e^{\beta \sum_{i=1}^{d} \hbar \omega_i (n+1/2)} = \sum_{n=0}^{\infty} \prod_{i=1}^{d} e^{-\beta \hbar \omega_i (n+1/2)} = \prod_{i=1}^{d} \frac{e^{-\beta \hbar \omega_i / 2}}{1 - e^{-\beta \hbar \omega_i}} \\
&= \prod_{i=1}^{d} \frac{1}{2 \sinh\left(\frac{\hbar \omega_i}{2 k_B T}\right)}
\end{aligned}
\tag{B.34}
$$

In the high-temperature limit, this expression approaches that obtained from the classical treatment. Defining a characteristic temperature, $T_{v,i} \equiv \frac{\hbar \omega_i}{k_B}$, associated with the quantization of the vibrational modes, we can write

$$
z_v = \prod_{i=1}^{d} \frac{1}{2 \sinh\left(\frac{T_{v,i}}{T}\right)}, \tag{B.35}
$$

with $z_v \approx \prod_{i=1}^{d} T/T_{v,i}$ for $T \gg T_{v,i}$.

The classical Hamiltonian for rotations of the gas molecules is [22]

$$\mathcal{H}^c_{rot} = \frac{1}{2I}\left(p^\theta + \frac{p_\phi^2}{\sin^2(\theta)}\right) \tag{B.36}$$

where I is the moment of inertia, θ and ϕ are the polar and azimuthal spherical angles, and p_θ, p_{phi} are the corresponding angular momenta. This gives for the classical rotational partition function [22]

$$\begin{aligned} z_r &= \frac{1}{h^2}\int_0^\pi \mathrm{d}\theta \int_0^{2\pi} (d)\phi \int_{-\infty}^{\infty}\int_{-\infty}^{\infty} \mathrm{d}p_\theta \mathrm{d}p_\phi \exp\left[-\beta\frac{1}{2I}\left(p^\theta + \frac{p_\phi^2}{\sin^2(\theta)}\right)\right] \\ &= \frac{2Ik_BT}{\hbar^2} \end{aligned} \tag{B.37}$$

It is convenient to define a characteristic temperature associated with the quantization of rotational degrees of freedom, just as has been done for the vibrational degrees of freedom,

$$T_{rot} = \frac{2Ik_BT}{\hbar^2}. \tag{B.38}$$

Then $z_r^c = T/T_r$.

Quantum mechanics dictates that the angular momentum is quantized according to $\mathbf{L}^2 = \hbar^2\ell(\ell+1)$, with $\ell = 0, 1, 2, \cdots$, with each state having a degeneracy of $2\ell+1$ [22]. As such, the quantum mechanical partition function is written as the discrete summation [22],

$$z_r^q = \sum_{\ell=0}^{\infty} \exp\left[-\frac{\beta\hbar^2\ell(\ell+1)}{2I}\right](2\ell+1) = \sum_{\ell=0}^{\infty} \exp\left[-\frac{T_r\ell(\ell+1)}{T}\right](2\ell+1). \tag{B.39}$$

For diatomic oxygen, $m_{\mathrm{O}} = 16$ amu with a bond length of about 121 pm [31], leading to a moment of inertia of $I_{\mathrm{O}_2} = m_{\mathrm{O}}(\ell_{bond}/2)^2 \approx 1.945 \times 10^{-46}$. Substituting this value into B.38 gives $T_{rot}^{\mathrm{O}_2} \approx 2.07$ K, well below the experimental range of temper-

atures. As such, we may safely employ the classical approximation for the rotational contribution to the partition function.

Values are available for the vibrational fundamental frequencies of monatomic oxygen on Pt(111): $\nu_{in-plane} = 800$ cm^{-1} and $\nu_{out-of-plane} = 480cm^{-1}$ [48]. These result in vibrational temperatures of $T_{in} \approx 1150$ K and $T_{out} \approx 691$ K. Further, the characteristic temperature for quantized longitudinal vibration in diatomic oxygen is 2274 K [25]. As these temperatures are either close to or surpass those of the experiment, the quantum-mechanical treatment for the partition function is necessary.

B.3 Diffusion Coefficient

The following section gives an estimate for the diffusion coefficient from a lattice hopping-model. It is based on an application of the work of Bokun et al [9] for the specific approximations and chemical potential already introduced in Section B.2. Bokun's work inherits from that of Zhdanov, and has a conceptual anchor in an influential work by Reed and Ehrlich [42]. Other schemes for computation of D may be found in [57, 24], as well as in [4].

It should be noted that such lattice hopping models are based upon an assumption of a Markovian model of motion that is, motion proceeds by uncorrelated "hops", so that an adsorbates position in the next instant of time only depends on where it is instantaneously[6] This condition is not satisfied at high temperatures when the thermal energy, k_BT, approaches or exceeds the migration barrier energy, E_m; a good rule of thumb is that the Markovian assumption may be invoked when $k_BT < \frac{1}{5}E_m$ [4]. Applying this basic test, we note that the heat of adsorption for oxygen on Pt(111) ranges from somewhat less than 1.7 eV at intermediate coverage to 5.2 eV at low coverage [18]. Ibach et al record another rule of thumb of estimating the diffusion migration barrier by halving the desorption/adsorption energy [20]; doing this gives a range of 0.8 to 2.6 eV for E_m. By comparison, the highest thermal energy at 800℃ is

[6]Actually, a Markovian framework may still be used as long as an adsorbates next movement only depends upon its history for a finite number of steps backward in time.

about $k_BT \approx 0.093$ eV $< \frac{1}{5}E_m$, so the Markovian hypothesis is appropriate, and the lattice hopping models are a valid interpretation of atomic oxygen diffusion on the Pt surface.

One further comment before continuing: it is not apparent how the lattice model that will be presented here maps to the actual surface lattice of oxygen on Pt. For example, there is an overwhelming body of evidence that oxygen sits in a p(2×2) ordering on the Pt(111) surface at coverage of around 1/4 monolayers (relative to (1×1) ordering) for temperatures between around 150 K to about 700 K [17, 18, 48, 49], and evidence that it occupies a (2×1) ordering on Pt(110) [53, 54]. How should we interpret the "lattice" in each of these cases? Ought we to consider only, say, the p(2×2) sites on Pt(111)? What effect, then, do the interstitial sites of the underlying Pt surface have? And how do we compensate for the fact that the actual Pt under study is polycrystalline? The answer to these questions is, in some sense, that the lattice hopping model is clearly a major simplification, as many of the modern experimental and simulation surface studies demonstrate [4], and as such, it is not particularly informative to chase after any exact representation of the polycrystalline surface with the crude methods employed here. Still, insofar as it is desirable to have some rationale in comparing the experimental results derived in this work with those already in the literature[7], some thought must be given to this matter.

In their 1980 work, Reed and Ehrlich pointed out that the diffusion flux, J, is driven not by a gradient in concentration, but in chemical potential[42]

$$J = -L_T \frac{\partial \beta\mu}{\partial x} \tag{B.40}$$

where D_J is a phenomenological transport coefficient and, again, $\beta \equiv 1/(k_BT)$. This results in an expression,

$$J = -D_J(\frac{\partial \mu/k_BT}{\partial \ln(\theta)})(\frac{\partial \theta}{\partial x}). \tag{B.41}$$

By comparison with 2.7, we can now identify the diffusion coefficient as

[7] e.g. interaction energetics may be estimated from these experiments, and such data exists in the literature for oxygen on Pt(111) [49]

$$D = D_J(\frac{\partial \beta\mu}{\partial \ln(\theta)}) \tag{B.42}$$

This can be further decomposed into a tracer diffusion prefactor, D_J, related to the hopping rate into empty sites, and a dimensionless thermodynamic factor,

$$\chi_T = (\frac{\partial \beta\mu}{\partial \ln(\theta)}), \tag{B.43}$$

related to the mean square particle number fluctuation. D_J is the diffusion coefficient which arises when particle-particle interactions are negligible (in which case χ_T tends to unity).

Bokun et al rederive an expression for D_J due to Zhdanov under more general conditions [9],

$$D_J = D_0 \frac{e^{\beta\mu} F(0,0)}{\theta} \tag{B.44}$$

with $D_0 = z w_0 a^2/(2d)$, where z is the coordination number of the lattice, w_0 is the transition rate scale, a is the lattice spacing, and d is the number of dimensions. $F(0,0)$ is the probability that two neighboring sites are both unoccupied[8] Within the mean field approximation, the occupation probability on the surface is unmodified from the non-interacting system; therefore $F(0,0) = F(0)F(0) = (1-\theta)^2$; more precise (and complicated) methods exist for evaluating the joint non-occupation probability [9, 22]. A value for D_0 might be obtained from estimating w_0 using the atomic vibration frequencies found in [48] (e.g. 800 cm^{-1}), but we will ultimately leave D_0 as a free fit parameter.

We obtained an expression for $e^{\beta\mu}$ in B.25, which was

$$e^{\beta\mu} = \frac{\theta}{1-\theta} e^{\beta(\theta u_0 - \epsilon)} z_v^{-1}. \tag{B.45}$$

[8]The hopping model employed here assumes nearest neighbor (NN) transitions, only; there is evidence in the literature of long-distance hops for surface diffusion [4], but as our goal here is mostly to obtain a qualitative dependence of the diffusion coefficient on state variable, we will ignore this potentially important correction. Bokun et al provide some details for how to include such longer transitions into a lattice hopping expression for D [9].

Applying it here gives

$$\begin{aligned} D_J &= D_0 \frac{\theta}{1-\theta} \frac{1}{z_v} \frac{e^{\beta\theta u_0} e^{-\beta\epsilon} (1-\theta)^2}{\theta} \\ &= D_0 (1-\theta) e^{\beta\theta u_0} e^{-\beta\epsilon} z_v^{-1} \end{aligned} \tag{B.46}$$

For the thermodynamic factor, the same expression for $e^{\beta\mu}$ may be used,

$$\begin{aligned} \chi_T = \frac{\partial \beta\mu}{\partial \ln(\theta)} &= \theta \frac{\partial}{\partial\theta} \left[e^{\beta\mu}\right] / e^{\beta\mu} \\ &= \theta \frac{\partial}{\partial\theta} \ln\left[\frac{\theta}{1-\theta} e^{\beta\theta u_0}\right] \\ &= \theta \left[\frac{1}{\theta(1-\theta)} + \beta u_0\right] \\ &= \frac{1 + \beta u_0 \theta (1-\theta)}{1-\theta} \end{aligned} \tag{B.47}$$

Putting these two results together gives for the diffusion coefficient,

$$\boxed{D(\theta) = D_J \chi_T = D_0 e^{\beta\theta u_0} e^{-\beta\epsilon} z_v^{-1} \left[1 + \beta u_0 \theta (1-\theta)\right]} \tag{B.48}$$

resulting in a very compact estimate for D which captures much of the interesting behavior of this parameter. Examining the behavior of D, we first see an increase with θ for repulsive interactions ($u_0 > 0$) and a decrease with θ for attractive interactions ($u_0 < 0$). This behavior follows from adsorbates tending to stick together with attractive interactions, and to push each other apart for repulsive interactions[9]. Differentiating D with respect to θ shows that D always has critical points at $\theta = 1$, leveling off after a sharp change at low coverage. More precise treatments do not retain a slope of exactly zero at $\theta = 1$, but nonetheless show the same behavior of a greater dependence at low coverage than high [9, 42]; such behavior is also seen in the diffusion data of Mitterdorfer and Gauckler [37]. There is another root in the slope

[9]Note that without interactions beyond the one-adsorbate-per-site limit (u_0=0), there is *no* change in D with respect to θ, as shown in [42].

at $\theta = -2/(\beta u_0)$; this shows that for attractive interactions ($u_0 < 0$) of sufficiently large magnitude $-\beta u_0 > 2$, D goes through a *minimum* at an intermediate coverage, a behavior also seen in other work [9, 42]. However, there is no corresponding maximum for repulsive interactions. Lastly, the expression predicts D to be less than zero down for attractive interactions when $-\beta u_0 > 4$. There is a physical significance associated with this situation: when attractive interactions between are dominant over random thermal motion in determining the evolution of the coverage profile (energetics dominates over statistics), diffusing particles will actually tend to move *up* the concentration gradient, rather than down, so that particles can be closer together.

Appendix C

Selected Electrochemical Derivations

C.1 Introduction

This appendix details the solution (and creation) of the partial differential equations used to describe the oxygen reduction reaction. It also compares the model used here with that found in Mitterdorfer and Gauckler's work [36, 37], and shows how the system of equations used by Mitterdorfer and Gauckler actually produce an electrochemical impedance which may be written analytically in the Gerischer form.

C.2 Generalized Model

All electrochemical impedance measurements are based upon a perturbation about some steady state by a small voltage signal. This is a physical manifestation of linearizing a very nonlinear response of current due to voltage, as the impedance corresponds to the fundamental terms in the harmonic series of the current response. It is entirely possible to measure the higher-order harmonics and thus probe the nonlinearity of the electrochemical system, and some work has been done in this area [6]. However, an *impedance* study implies a focus on the fundamental terms, only.

This motivates the creation of a system of equations which generalizes the *lin-*

earized response of current due to voltage. The value in such a generalized model results from the fact the mathematical description of many different, nonlinear systems will assume this same general form upon linearization. One consequence of this is that it is not possible to pinpoint the physics and chemistry of a particular system simply by identifying the impedance response as conforming to this general form [2, 10]; as such, a more careful interpretation of impedance results is necessary.

C.2.1 Transport

Fick's first law of diffusion is

$$\boldsymbol{\phi} = -D\nabla\rho \tag{C.1}$$

where $\boldsymbol{\phi}$ is the flux, D is the diffusion coefficient (or diffusivity) and ρ is the density (or concentration). In two dimensions, *phi* has units of number per unit time per unit length, and ρ has units of number per unit area (note that D *always* has units of unit area per unit time). Because we are dealing with a lattice gas (i.e. we envision that particles can only occupy a finite number of fixed sites), it is convenient to normalize by the total number of sites per unit area, Γ. Then $\rho/\Gamma = \theta$, the coverage, $\in [0, 1]$, and $\boldsymbol{\phi}/\Gamma = \phi_\theta$ is a flux for the coverage quantity.

Appendix B discussed a subtlety of this phenomenological constitutive relation which resulted in an implicit dependence of the diffusion coefficient, D, on the coverage. Here, we will continue to use Fick's formalism keeping this proviso in mind.

Other transport processes might be envisioned (e.g. ohmic drift, tunneling, ballistic diffusion, etc.), but for a wide-class of situations, and in particular situations involving surfaces, diffusion ought to be the dominant, if not the only, transport mechanism.

C.2.2 Sorption

There is also a generation/annihilation process: adsorption and desorption. For now, we will not specify the details of this process, but will leave it in a generic form, g:

$$\left.\frac{\partial \rho}{\partial t}\right|_{sorption} = g(\rho, T) \tag{C.2a}$$

$$\left.\frac{\partial \theta}{\partial t}\right|_{sorption} = g(\rho, T)/\Gamma = g_\theta(\theta, T) \tag{C.2b}$$

$$\tag{C.2c}$$

Here, it is assumed that g only depends on the state variables, coverage, θ and temperature, T (note that the three relevant intensive variables, temperature, pressure, and number, are related through an equation of state, the *coverage isotherm*). A uniformity of the surface is implicit in this assumption. For simplicity, it is assumed that g is time-independent; any time-dependence of g should be associated with changes to the surface due to annealing, oxide formation, and so forth, processes which, at the least, are expected to occur on a timescale longer than an individual EIS measurement.

Henceforth, the temperature dependence will be suppressed in the expression of g for the sake of convenience.

C.2.3 Synthesis of Governing Partial Differential Equation

Applying the conservation of particle number,

$$\frac{\partial \rho}{\partial t} + \nabla \cdot \boldsymbol{\phi} = g \tag{C.3}$$

where g is a local generation term which here corresponds to the sorption process. Using Fick's constitutive law for the flux term gives

$$\frac{\partial \rho}{\partial t} = \nabla \cdot (D \nabla \rho) + g(\rho) \tag{C.4}$$

In normalized form, this becomes

$$\frac{\partial \theta}{\partial t} = \nabla \cdot (D(\theta) \nabla \theta) + g_\theta(\theta) \tag{C.5}$$

where the dependence of D on θ is now shown explicitly.

This is a very generic governing partial differential equation, as g may have other interpretations besides sorption (e.g. incorporation into the surface, surface reaction leading to synthesis of diffusing particles, etc.).

C.3 Linearization

It will next be assumed that the coverage is only modified by a small amount,

$$\theta = \bar{\theta} + \delta\theta \approx \bar{\theta} \tag{C.6}$$

Carrying out a Taylor series expansion for any quantity, $f(\theta)$, in θ about $\bar{\theta}$,

$$f(\theta) = \sum_{n=0}^{\infty} \frac{1}{n!} \left[\frac{\mathrm{d}^n f}{\mathrm{d}\theta^n}\right]_{\bar{\theta}} \delta\theta^n = f(\bar{\theta}) + \left[\frac{\mathrm{d}f}{\mathrm{d}\theta}\right]_{\bar{\theta}} \delta\theta + \cdots \tag{C.7}$$

Assuming the series is well-ordered such that the higher-order terms decay, we desire that $f(\theta) = f(\bar{\theta}) + \left[\frac{\mathrm{d}f}{\mathrm{d}\theta}\right]_{\bar{\theta}} \delta\theta + \mathscr{O}(\delta\theta^2) \approx f(\bar{\theta})$, or

$$f(\bar{\theta}) \gg \left[\frac{\mathrm{d}f}{\mathrm{d}\theta}\right]_{\bar{\theta}} \delta\theta \tag{C.8}$$

The quantities that will be linearized are D and g. In the first case, we will keep only the zeroth-order term of D, $D(\bar{\theta})$. This allows the diffusion coefficient to be pulled outside of the divergence operator in C.5, since any variation in θ, spatial or temporal, is only in $\delta\theta$. For g, physical intuition suggests that the sorption process acts to return θ to its equilibrium value, $\bar{\theta}$. As such, the zeroth-order term in the expansion should vanish, and the first-order term should move in the opposite direction as $\delta\theta$ (negative feedback). Then it is natural to construct a linearized form of g as

$$g_\theta(\bar{\theta} + \delta\theta) \approx -\alpha\delta\theta \tag{C.9}$$

These linearizations allow the governing partial differential equation to be written

as

$$\frac{\partial \theta}{\partial t} = D(\bar{\theta})\nabla^2(\delta\theta) - \alpha(\delta\theta) \tag{C.10}$$

This is the linearized governing partial differential equation we had been after.

C.4 Phasor Representation

Because we are only working with the fundamental modes of oscillations, it is convenient to work in the formalism of phasors. Here, a quantity, $f(t;\mathbf{x})$, is related to its complex amplitude (phasor), $\tilde{f}(\mathbf{x})$, by

$$f(t;\mathbf{x}) = \Re(e^{j\omega t}\tilde{f}(\mathbf{x})) \tag{C.11}$$

Transforming C.10 to the phasor domain gives

$$j\omega\tilde{\theta} = D(\bar{\theta})\nabla^2\tilde{\theta} - \alpha\tilde{\theta} \tag{C.12}$$

where $\tilde{\theta}$ is the phasor of $\delta\theta$.

Henceforth, the tilde superscript, $\backsim$, will be used to indicate a phasor quantity.

C.5 Solution in One-Dimensional, Semi-Infinite Geometry

In order to solve the governing differential equations, we need boundary conditions. These depend both on the physical processes occurring at the boundaries and on the geometry of the system. In a one-dimensional geometry in a semi-infinite space, these boundary conditions are as follows:

$$\frac{\tilde{\phi}}{\Gamma} = -D\nabla\tilde{\theta} \tag{C.13a}$$

$$\tilde{\theta}(r \to \infty) = 0 \tag{C.13b}$$

$$\tag{C.13c}$$

Here, the triple phase boundary is placed at position $r = 0$. The second boundary condition states that very far from the TPB, the perturbation in coverage vanishes. The first boundary condition corresponds to applying Fick's first law at the TPB. But at this point, we might write a charge incorporation step [36, 37],

$$\Gamma\theta + \mathrm{V}_{\ddot{\mathrm{O}}} + \times e^- \underset{k_{-1}}{\overset{k_1}{\rightleftharpoons}} \mathrm{O}_{\mathrm{O}}^{\times} + \Gamma(1-\theta) \tag{C.14}$$

where k_1 is the forward electrochemical rate constant, k_{-1} the backward, $\mathrm{V}_{\ddot{\mathrm{O}}}$ is the oxygen vacancy concentration inside the YSZ (material constant), $\mathrm{O}_{\mathrm{O}}^{\times}$ the oxygen ions concentration, $\times e^-$ is representative of a final transfer before adsorbate incorporation into the YSZ[1], and the term, $\Gamma(1-\theta)$ is the empty-site concentration on the surface. This leads (by mass action) to an expression for the flux of oxygen ions *into* the YSZ:

$$\phi(r_{tpb})_{\text{into YSZ}} = \Gamma\theta k_1 \mathrm{V}_{\ddot{\mathrm{O}}} - \Gamma(1-\theta)k_{-1}\mathrm{O}_{\mathrm{O}}^{\times} \tag{C.15}$$

The electric current *into* the YSZ is simply the flux multiplied by the total TPB length, ℓ, and the charge carried by each oxygen anion, $-nq_e$ (here, n=2):

$$I = -nq_e\ell\phi(r_{tpb})_{\text{into YSZ}} = nq_e\ell\Gamma((1-\theta)k_{-1}\mathrm{O}_{\mathrm{O}}^{\times} - \theta k_1 \mathrm{V}_{\ddot{\mathrm{O}}}) \tag{C.16}$$

where θ here is evaluated at the triple phase boundary.

The forward and backward electrochemical rate constants, k_{-1} and k_1, are defined

[1]Oxygen is likely already reduced upon adsorption, but the degree to which it is reduced is subject to debate [2]. As such, $\times e^-$ is included here to represent "whatever is left" to reduce oxygen to its charge state inside the YSZ bulk. The term does not appear in the kinetic equations because the electron concentration is essentially unlimited, and the rate of transfer is implicit in k_1, k_{-1}.

as

$$k_{-1} = k_{-1,0} e^{b_{-1} V} \tag{C.17a}$$

$$k_1 = k_{1,0} e^{b_1 V} \tag{C.17b}$$

with

$$b_{-1} \equiv \frac{q_e}{k_B T}(1 - \zeta) \tag{C.18a}$$

$$b_1 \equiv -\frac{q_e}{k_B T}\zeta \tag{C.18b}$$

where V is the overpotential above the equilibrium voltage, $V = V_{external} - V_{eq}$, and $\zeta \in [0, 1]$ is the charge transfer coefficient[2] between the forward and backward reactions, and is usually around $\frac{1}{2}$. The overpotential may be a foreign term for some readers; it is a convenient quantity to work with in light of the fact that there is generally a nonzero voltage between the terminals of an electrochemical device at equilibrium (zero current), just as occurs across the metallic junction in a pn-diode.

Shortly, the quantity $\partial I / \partial \theta$ will appear; it is calculated here as

$$\frac{\partial I}{\partial \theta} = -n q_e \ell \Gamma (k_{-1} \mathrm{O}_{\mathrm{O}}^{\times} + k_1 \mathrm{V}_{\ddot{\mathrm{O}}}) \tag{C.19}$$

In one dimension, the natural eigenfunctions of C.10 are exponentials,

$$\tilde{\theta} = A e^{r/\xi} + B e^{-r/\xi} \tag{C.20}$$

where

$$\xi \equiv \sqrt{\frac{D(\bar{\theta})}{j\omega + \alpha}} \tag{C.21}$$

is a characteristic length of the perturbation extent.

The boundary condition at $r \to \infty$ requires $A = 0$. B is defined through the

[2] or Tafel constant, symmetry factor

remaining boundary condition,

$$\begin{aligned}
\tilde{\phi}(r_{tpb})_{\text{into YSZ}} &= \Gamma(\tilde{\theta}k_1\mathrm{V}_{\ddot{\mathrm{O}}} - (1-\tilde{\theta})k_{-1}\mathrm{O}_{\mathrm{O}}^{\times}) \\
&= -D\frac{\mathrm{d}\Gamma\tilde{\theta}}{\mathrm{d}r} \\
&= \frac{D}{\xi}\Gamma\tilde{\theta} \\
&= -\frac{\tilde{I}}{nq_e\ell} \\
&\implies \tilde{\theta}(r=0) = B = \frac{k_{-1}\mathrm{O}_{\mathrm{O}}^{\times}}{k_1\mathrm{V}_{\ddot{\mathrm{O}}} + k_{-1}\mathrm{O}_{\mathrm{O}}^{\times} - D/\xi} \\
= -\frac{\tilde{I}}{nq_e\Gamma\ell D/\xi}
\end{aligned} \tag{C.22}$$

Finally, $\tilde{\theta}$ is

$$\tilde{\theta}(r) = -\frac{\tilde{I}}{nq_e\Gamma\ell D/\xi}e^{-r/\xi} \tag{C.23}$$

Note that $\tilde{\theta}$ is proportional to $\tilde{I}$; this fact will be useful later.

C.6 Solution in One-Dimensional, Finite Geometry

The next iteration in one dimension is to solve for a finite-length geometry. To do this, we will now place the triple-phase boundary at a position, R_e, and we will impose a zero-flux boundary condition, $\phi = 0$, at $r = 0$ [3]. Mathematically,

[3]This is a rather artificial boundary condition, as the "other end" of the electrode probably has a charge-transfer reaction as at R_e, but the impedance expression it develops has an intuitive correspondence to that which will develop for the cylindrical geometry. One situation in which it might arise is for two identical electrode edges (TPBs) at $r = \pm R_e$; then the flux at $r = 0$ should be equal in both directions by symmetry, so it must be zero.

$$\left.\frac{\tilde{\phi}}{\Gamma}\right|_{r=R_e} = -D\nabla\tilde{\theta}(R_e) \qquad \tilde{\phi}(r=0) = 0 \tag{C.24}$$

In this case, it is more convenient to express the eigenfunctions of C.12 in terms of hyperbolic trigonometric functions,

$$\tilde{\theta} = A\cosh\left(\frac{r}{\xi}\right) + B\sinh\left(\frac{r}{\xi}\right) \tag{C.25}$$

where ξ is defined in C.21. The boundary condition at $r = 0$ requires that $B = 0$, while that at R_e gives for A

$$\begin{aligned}
\tilde{\phi}(r_{tpb})_{\text{into YSZ}} &= \Gamma(\tilde{\theta}k_1\mathrm{V}_{\ddot{\mathrm{O}}} - (1-\tilde{\theta})k_{-1}\mathrm{O}_{\mathrm{O}}^{\times}) \\
&= -D\frac{\mathrm{d}\Gamma\tilde{\theta}}{\mathrm{d}r} \\
&= \frac{D}{\xi}\Gamma A\sinh\left(\frac{R_e}{\xi}\right) \\
&= -\frac{\tilde{I}}{nq_e\ell} \\
&\Longrightarrow A = -\frac{\tilde{I}}{nq_e\Gamma\ell\sinh(R_e/\xi)D/\xi}
\end{aligned} \tag{C.26}$$

Then $\tilde{\theta}$ is expressed as

$$\tilde{\theta}(r) = -\frac{\tilde{I}}{nq_e\Gamma\ell D/\xi}\frac{\cosh(r/\xi)}{\sinh(R_e/\xi)}. \tag{C.27}$$

C.7 Solution in Finite Cylindrical Geometry

Having become comfortable with two one-dimensional solutions, we can now investigate solutions in two dimensions. Perhaps the most accessible is that pertaining to cylindrically-symmetric geometry. In this case, the interface between the Pt elec-

trode and YSZ electrolyte occurs at $r = R_e$, where now r is the radial coordinate. A zero-flux boundary condition may be imposed at $r = 0$ based upon symmetry.

$$\begin{aligned} \left.\frac{\tilde{\phi}}{\Gamma}\right|_{r=R_e} &= -D\nabla\tilde{\theta}(R_e) \\ \tilde{\phi}(r=0) &= 0 \end{aligned} \tag{C.28}$$

It is instructive to rewrite C.12 so that the Laplacian (axial symmetry) is shown explicitly in terms of partial derivatives in ϕ and r:

$$\begin{aligned} j\omega\tilde{\theta} = D(\bar{\theta})\left(\frac{\partial^2\tilde{\theta}}{\partial r^2} + \frac{1}{r}\frac{\partial\tilde{\theta}}{\partial r}\right) - \alpha\tilde{\theta} \\ \Longrightarrow 0 = \frac{\partial^2\tilde{\theta}}{\partial r^2} + \frac{1}{r}\frac{\partial\tilde{\theta}}{\partial r} - \xi^2\tilde{\theta} \end{aligned} \tag{C.29}$$

Now, the natural eigenfunctions are *modified Bessel functions of the first kind*, so classified because of the negative sign before *adsRate*. As sinusoidal functions become hyperbolic sinusoidal functions when given an imaginary argument, modified Bessel functions are sometimes called *hyperbolic* Bessel functions[4]. The comparison is useful in understanding the properties of the modified Bessel function, as well as how the geometry effects the solutions and, later, the impedance expressions. We will try as a solution

$$\tilde{\theta} = A\mathrm{J}_0(jr/\xi) = A\mathrm{M}_0(r/\xi) \tag{C.30}$$

where J_0 is the zeroth-order Bessel function of the first kind, M_0 is the zeroth-order modified Bessel function of the first kind, and the imaginary argument to J_0 is traced back to the sign before ξ^2. The gradient of $\tilde{\theta}$ in cylindrical coordinates with axial symmetry is just $\hat{r}\partial\tilde{\theta}/\partial r$ ($\hat{r}$ denotes the radial unit vector). Since $\partial\mathrm{J}_0(x)/\partial x = -\mathrm{J}_1(x)$, $\partial\mathrm{M}_0(x)/\partial x = \mathrm{M}_1(x)$, and since $\mathrm{M}_1(0) = 0$, the zero-flux boundary condition

[4]In general, the Bessel function of the first kind is related to the modified Bessel function of the first kind by $\mathrm{M}_p(x) = \mathrm{J}_p(jx)/j^p$.

at $r = 0$ is satisfied. At the triple phase boundary,

$$\begin{aligned}
\tilde{\phi}(r_{tpb})_{\text{into YSZ}} &= \Gamma(\tilde{\theta}k_1 \mathrm{V}_{\ddot{\mathrm{O}}} - (1-\tilde{\theta})k_{-1}\mathrm{O}_{\mathrm{O}}^{\times}) \\
&= -D\frac{\mathrm{d}\Gamma\tilde{\theta}}{\mathrm{d}r} \\
&= -j\frac{D}{\xi}\Gamma A \mathrm{J}_1\left(\frac{R_e}{\xi}\right) \\
&= -\frac{\tilde{I}}{nq_e\ell} \\
&\implies A = j\frac{\tilde{I}}{nq_e\Gamma\ell \mathrm{J}_1(jR_e/\xi)D/\xi}
\end{aligned} \tag{C.31}$$

Then $\tilde{\theta}$ is, in cylindrical coordinates,

$$\tilde{\theta}(r) = j\frac{\tilde{I}}{nq_e\Gamma\ell D/\xi}\frac{\mathrm{J}_0(jr/\xi)}{\mathrm{J}_1(jR_e/\xi)}. \tag{C.32}$$

C.8 Electrochemical Impedance

To obtain an expression for impedance from these solutions, let us first express the current, I, and voltage across the device, V, as perturbations,

$$I = \bar{i} + \Re(e^{j\omega}\tilde{i}) \tag{C.33a}$$

$$V = \bar{v} + \Re(e^{j\omega}\tilde{v}) \tag{C.33b}$$

$$\tag{C.33c}$$

Then the variation in I is expanded to first order as

$$\tilde{i} = \left.\frac{\partial I}{\partial\theta}\right|_{\bar{\theta},\bar{v}} \mathrm{d}\theta + \left.\frac{\partial I}{\partial V}\right|_{\bar{\theta},\bar{v}} \mathrm{d}V + \cdots \tag{C.34}$$

But $\mathrm{d}\theta = \tilde{\theta}$ and $\mathrm{d}v = \tilde{v}$; then

$$\tilde{i} = \left.\frac{\partial I}{\partial \theta}\right|_{\bar{\theta},\bar{v}} \tilde{\theta} + \left.\frac{\partial I}{\partial V}\right|_{\bar{\theta},\bar{v}} \tilde{v} + \cdots \tag{C.35}$$

where it is understood that $\tilde{\theta}$ refers to the coverage perturbation *at the boundary*. The quantity, $\left(\frac{\partial I}{\partial V}\right)^{-1}$ is called the *charge transfer resistance*, R_{ct}. $\partial I/\partial\theta$ is given in C.19.

Now, we have seen that $\tilde{\theta}$ is proportional to $-\tilde{i}$ for all of the cases investigated here. As such, we might factor out $-\tilde{i}$

$$\tilde{i}\left[1 + \left.\frac{\partial I}{\partial \theta}\right|_{\bar{\theta},\bar{v}} \frac{\tilde{\theta}}{-\tilde{i}}\right] = (R_{ct})^{-1}\tilde{v}. \tag{C.36}$$

This leads to the Faradaic impedance, $Z_F \equiv \tilde{v}/\tilde{i}$,

$$\boxed{Z = R_{ct}\left[1 + \frac{\tilde{\theta}}{-\tilde{i}}\frac{\partial I}{\partial \theta}\right]} \tag{C.37}$$

The term, "Faradaic impedance", is used to distinguish this component of impedance from the total impedance measured across the device terminals.

From here, we can substitute the solutions for $\tilde{\theta}$ directly into C.37 to obtain Faradaic impedance expressions for each case.

For the one-dimensional semi-infinite case, with the triple-phase boundary at $r = 0$,

$$\boxed{Z_G = R_{ct}\left[1 + \frac{\frac{\partial I}{\partial \theta}}{nq_e\Gamma\ell\sqrt{D(j\omega+\alpha)}}\right]} \tag{C.38}$$

where D/ξ has been written explicitly. This takes the form of the well-known "Gerischer" impedance [2]. The salient feature of this impedance expression is the $1/\sqrt{j\omega+\alpha}$ factor in the frequency-dependent component. For $\omega \gg adsRate$, this term has equal real and imaginary parts, leading to a forty-five-degree line in the Nyquist plot (locus of points for all ω in the complex-Z plane). The low-frequency portion of the Nyquist plot more resembles a semicircle. This leads to a familiar "teardrop" shape.

In the one-dimensional finite-length case, with triple-phase boundary at $r = R_e$,

$$\boxed{Z_{FL} = R_{ct}\left[1 + \frac{\frac{\partial I}{\partial \theta}}{nq_e\Gamma\ell\sqrt{D(j\omega+\alpha)}}\coth\left(R_e/\xi\right)\right]} \tag{C.39}$$

This expression is similar to the form of the "finite-length Warburg" impedance element, also well-known in electrochemical impedance spectroscopy [2], except that in this element, the *coth* is replaced by a *tanh*. The finite-length Warburg would have appeared exactly if the boundary condition at $r = 0$ had been $\tilde{\theta} = 0$ instead of $\tilde{\phi} = 0$[5].

Finally, for the cylindrical case, again with triple-phase boundary at $r = R_e$,

$$\boxed{Z_{cyl} = R_{ct}\left[1 + \frac{\frac{\partial I}{\partial \theta}}{nq_e\Gamma\ell\sqrt{D(j\omega+\alpha)}}\frac{\mathrm{M}_0\left(R_e/\xi\right)}{\mathrm{M}_1\left(R_e/\xi\right)}\right]}. \tag{C.40}$$

It is noteworthy that both finite-length expressions, Z_{FL} and Z_{cyl}, approach the Gerischer form for the case when the *utilization length*, $l_\delta \equiv \xi(\omega = 0)$ (see [2] for introduction of this term), becomes very small[6]. This is very reasonable, and should be expected in general, since perturbations are restricted to a narrow region very close to the triple-phase boundary have no way of knowing about the geometry of the electrode (i.e. the electrode is effectively infinitely large for the short-range perturbations, satisfying the Gerischer conditions). Further, the finite-length impedance in one-dimension closely parallels that in cylindrical coordinates, as $\coth(R_e/\xi)$ and $\mathrm{M}_0\left(R_e/\xi\right)/\mathrm{M}_1\left(R_e/\xi\right)$ behave similarly, though the latter decays much more slowly than the former.

It must be pointed out that if $\bar{\theta}$ is independent of position, $\nabla\bar{\theta} = 0$, then by Fick's first law, $\bar{i} = 0$, so that the perturbation must be carried out about equilibrium. For this condition to be met, $\bar{v} = 0$. It would be desirable to run EIS experiments under nonzero polarization; however, in order to do this, it necessary to know precisely how the diffusion coefficient depends upon coverage. As the estimates conducted in

[5]This boundary condition is, perhaps, even more artificial than the one we used.

[6]This happens when $D \ll \alpha$, corresponding to slow diffusion *relative to* the *linearized* net sorption rate.

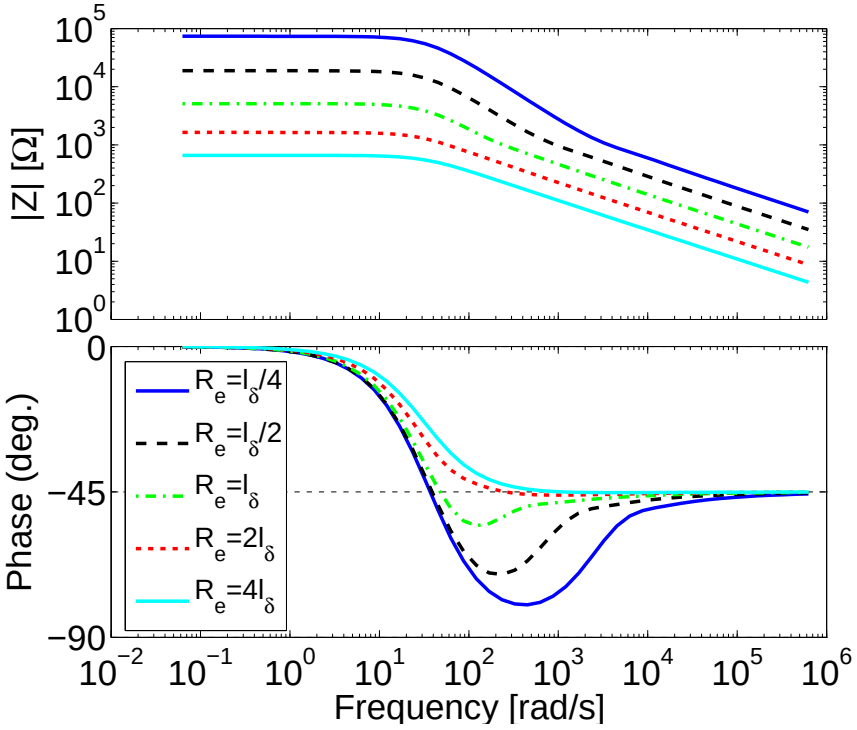

Figure C-1: Bode magnitude and phase plots for the cylindrical impedance element. Figures show response when utilization length, l_δ, is less than, equal to, and greater than the electrode radius. High-frequency real asymptote has been zeroed to reveal 45° phase angle. Reprise of Figure 2-5b.

Appendix B are crude at best, we are not in a position to proceed in this direction.

C.9 Frequency Responses and Bode Plots

Graphical analysis provides intuition as to the behavior of these impedance elements.

All three frequency responses show a low- and high-frequency value with varyingly-steep transition regions in between. It is typical in the experiments comprising this study for there to be several orders of magnitude difference between these low- and high-frequency limits, as depicted in the plots.

Defining $\boldsymbol{\gamma}$ analogously to 3.3 for the Gerischer case as

$$\begin{aligned}
\gamma_1 &= R_{ct} = \left[nq_e\ell\Gamma\left(b_{-1}k_{-1}\mathrm{O}_{\ddot{\mathrm{O}}}^{\times}\left(1-\bar{\theta}\right) - b_1k_1\mathrm{V}_{\ddot{\mathrm{O}}}\bar{\theta}\right)\right]^{-1} \\
\gamma_2 &= R_{ct}\frac{\partial I/\partial\theta}{nq_e\Gamma\ell\sqrt{D}} = R_{ct}\frac{k_1\mathrm{V}_{\ddot{\mathrm{O}}} + k_{-1}\mathrm{O}_{\ddot{\mathrm{O}}}^{\times}}{\sqrt{D}} \approx \frac{1}{nq_e\ell\Gamma\frac{q_e}{k_BT}\bar{\theta}(1-\bar{\theta})\sqrt{D}} \\
\gamma_3 &= S(\theta,T)\left[a_s\frac{\lambda}{h}\left(\frac{\partial\theta}{\partial P}\right)^{-1}\right]
\end{aligned} \tag{C.41}$$

the observation of the large difference between low- and high-frequency impedance limits is captured via parameter relations through the statement, $\gamma_2/\sqrt{\gamma_3} \gg \gamma_1$. Expressions for the magnitude, $|Z|$, and phase, ϕ, real, and imaginary parts of the Gerischer impedance are written below:

$$\begin{aligned}
|Z_G| &= R_1 + \frac{R_2}{\sqrt{A}} = R_1\frac{\sqrt{A}+R_2/R_1}{\sqrt{A}} \\
\phi \equiv \angle Z &= \arctan\left[-\frac{\frac{R_2}{\sqrt{A}}\sin\left(\frac{\delta}{2}\right)}{R_1 + \frac{R_2}{\sqrt{A}}\cos\left(\frac{\delta}{2}\right)}\right] \\
\Re\{Z\} &= R_1 + \frac{R_2}{\sqrt{A}}\cos\left(\frac{\delta}{2}\right) \\
\Im\{Z\} &= -\frac{R_2}{\sqrt{A}}\sin\left(\frac{\delta}{2}\right)
\end{aligned} \tag{C.42}$$

where

$$\begin{aligned}
A^2 &\equiv \omega^2 + \alpha^2 \\
\tan(\delta) &\equiv \frac{\omega}{\alpha}.
\end{aligned} \tag{C.43}$$

A useful result for the Gerischer impedance regarding the lower corner frequency[7] follows:

$$\omega_{c,g} = \sqrt{\left(\frac{4\gamma_2}{(\gamma_2/\sqrt{\alpha}) - 2R_1}\right)^4 - \alpha^2} \approx \sqrt{255\alpha_3^2} \approx 16\alpha \tag{C.44}$$

[7]The corner frequency is variously defined as a kink in the Bode plots; traditionally, it is the point where the magnitude of the transfer function under study drops by a factor of $\frac{1}{2}$, or approximately 3 dB, from some important limiting value, and this is the definition used here.

As such, the corner frequency may be used to rapidly estimate this adsorption-related model parameter. For the other geometries and boundary conditions, the corner frequency ought to track with α in approximately the same way.

C.10 Kinetics-Based Model of Mitterdorfer and Gauckler

The work above is generalized from the model of Mitterdorfer and Gauckler only in the treatment of sorption. However, where Mitterdorfer and Gauckler chose a numerical, state-space solution to calculate the impedance, we have chosen to restrict ourselves to simple geometries and write analytical solutions.

Sorption is handled in Mitterdorfer and Gauckler by a Langmuirian surface reaction,

$$P_{O_2,gas} + 2\Gamma(1-\theta) \underset{k_d}{\overset{k_a}{\rightleftharpoons}} 2\Gamma\theta. \tag{C.45}$$

where $P_{O_2,gas} = P$ is the oxygen gas partial pressure and k_a and k_d are the adsorption and desorption rate constants. This gives rise to a coverage isotherm,

$$\theta = \frac{1}{1+\sqrt{k_d/(k_a P)}} \tag{C.46}$$

When linearized, this model exactly corresponds to the generalized case above for $\alpha = 2\Gamma\sqrt{k_a k_d P}$, as can be seen by writing the kinetic equations resulting from C.45 and linearizing the quadratic terms. As such, the electrochemical impedance of the Mitterdorfer-Gauckler model is exactly of the Gerischer analytical form. The numerical solution carried out in their original work is, with appropriate generalized differential operators, extensible to a number of other arbitrary geometries, in which case the Gerischer form does not arise exactly[8]. In fact, in analysis of their data, Mitterdorfer and Gauckler only apply their model within a one-dimensional semi-infinite framework[36, 37, 38], where their numerical solution ought to reproduce a

[8]though much of the same qualitative behavior ought to exist, as observed for the finite-length and cylindrical cases above.

Gerischer impedance.

C.11 Model Used Here

The model used in the present study differs from that of Mitterdorfer and Gauckler only in the sorption terms. In B, a coverage isotherm is derived from a statistical mechanics framework. This may then be used in conjunction with a kinetics-motivated expression that is more standard with respect to surface studies for oxygen on Pt [25, 54, 20, 17]. In particular, as seen in an expression typifying the work of Kreuzer et al [25],

$$\left(\frac{d\theta}{dt}\right)_{ad-des} = S(\bar{\theta}, T)\left[a_s \frac{\lambda}{h}(P - \bar{P})\right], \tag{C.47}$$

where λ is the thermal wavelength (see B), $a_s = \frac{1}{\Gamma}$ is the area per adsorption site so that $a_s \frac{\lambda}{h} P$ is the total flux rate of impinging particles per adsorption site, P is the instantaneous oxygen gas partial pressure and $\overline{P}(\theta)$ the pressure corresponding to equilibrium at the instantaneous coverage, and S the sticking coefficient - the probability that an impinging particle will adsorb. An advantage of this scheme is that data for S exists from surface studies [54, 20, 17, e.g]. For our purposes, we might more conveniently define the instantaneous adsorption rate in the perturbation limit where $\Delta P = P - \bar{P} = -(P(\bar{\theta} + \mathrm{d}\theta) - P(\bar{\theta})) \approx -\left.\partial P/\partial\theta\right|_{T,\bar{\theta}} \mathrm{d}\theta$ is small as

$$\left(\frac{d\theta}{dt}\right)_{ad-des} = -S(\bar{\theta}, T)\left[a_s \frac{\lambda}{h}\left(\frac{\mathrm{d}P}{\mathrm{d}\theta}\right)_{T,\bar{\theta}} \mathrm{d}\theta\right]. \tag{C.48}$$

Then α is identified immediately as $\alpha = S(\bar{\theta}, T)\left[a_s \frac{\lambda}{h}\left(\frac{\mathrm{d}\theta}{\mathrm{d}P}\right)^{-1}\right]$, a quantity which is ultimately positive because $\left.\partial\theta/\partial P\right|_T$ is positive (as can be seen in the Langmuir isotherm of Mitterdorfer and Gauckler).

Appendix D

Fitting Details

D.1 Introduction

In the following, several derivations are worked out pertaining to the numerical fitting process. Important results include the Jacobian matrices used in the fitting procedure; while it is possible to calculate these matrices numerically, exact closed-form expressions lead not only to faster, but also more stable, fitting. As a matter of practically, methods are reviewed and recorded for approximating the ratio of modified Bessel functions, which occur in the cylindrical impedance element expressions. Finally, some discussion is devoted to parameter sensitivity and error analysis so that the accuracy of predictions made from this procedure may be gauged.

D.2 Jacobians of Fitting Expressions

In a number of numerical schemes for the solution to 3.4, the Jacobian matrix of Z_{cyl} is an item of central importance.

The Jacobian matrix for an n-component vector function, $\mathrm{G}(\mathbf{x};\boldsymbol{\gamma})$, is the $n \times k$ matrix whose columns are the partial derivatives of each of the n components of G with respect to the parameters in $\boldsymbol{\gamma}$,

$$\mathcal{J} = \begin{bmatrix} \frac{\partial \mathrm{G}(x_1;\boldsymbol{\gamma})}{\partial \gamma_1} & \frac{\partial \mathrm{G}(x_1;\boldsymbol{\gamma})}{\partial \gamma_2} & \cdots & \frac{\partial \mathrm{G}(x_1;\boldsymbol{\gamma})}{\partial \gamma_k} \\ \frac{\partial \mathrm{G}(x_2;\boldsymbol{\gamma})}{\partial \gamma_1} & \frac{\partial \mathrm{G}(x_2;\boldsymbol{\gamma})}{\partial \gamma_2} & & \\ \vdots & & \ddots & \\ \frac{\partial \mathrm{G}(x_n;\boldsymbol{\gamma})}{\partial \gamma_1} & & & \frac{\partial \mathrm{G}(x_n;\boldsymbol{\gamma})}{\partial \gamma_k} \end{bmatrix} \tag{D.1}$$

In a compact notation, the $\mu\nu^{th}$ element of this matrix is written as $\mathcal{J}_{\mu\nu} = \frac{\partial \mathrm{G}(x_\mu;\boldsymbol{\gamma})}{\partial \gamma_\nu}$.

Fortunately, it is possible to write an analytical expression for this Jacobian, a fact which assures increased speed and robustness of the numerical procedure.

Define the ratio of zero to first order modified Bessel functions of the first kind as $f(x) \equiv M_0(x)/M_1(x)$. Then $f'(x) \equiv \mathrm{d}f(x)/\mathrm{d}x = 1 - f(x)[f(x) - 1/x]$.

With this definition, the column vectors of the Jacobian matrix for the Faradaic impedance in the cylindrical geometry are written as follows:

$$\mathcal{J}_{all,1} = \mathbf{1}, \tag{D.2}$$

$$\mathcal{J}_{all,2} = \frac{f(x)}{\sqrt{j\omega + \gamma_3}}, \tag{D.3}$$

$$\mathcal{J}_{all,3} = \frac{1}{2}\gamma_2 \frac{xf'(x) - f(x)}{(\sqrt{j\omega + \gamma_3})^3}, \tag{D.4}$$

and

$$\mathcal{J}_{all,4} = \gamma_2 f'(x), \tag{D.5}$$

where $\mathbf{1}$ is a vector of all ones.

D.2.1 Error Estimation and the Hessian Matrix

The Jacobian matrix contains the function first derivatives about every data point; this provides an essential tool for numerical minimization schemes. The second derivatives are also useful, especially in estimating errors. For a scalar function, $\mathrm{F}(\boldsymbol{\gamma})$, the

Hessian matrix operator, H, contains the second derivatives. In a shorthand notation,

$$\mathrm{H}\{\mathrm{F}(\boldsymbol{\gamma})\}_{\mu\nu} = \frac{\partial^2 \mathrm{F}(\boldsymbol{\gamma})}{\partial\gamma_\mu \partial\gamma_\nu}. \tag{D.6}$$

The matrix is symmetric.

The reason that the Hessian matrix is useful in error estimation is that the second moment of a probability distribution provides information about deviation about the mean (or first moment and first cumulant) of the distribution. Because the matrix contains all permutations of second derivatives, it might be intuited that it contains information about the correlation coefficients, and this is indeed the case.

D.2.2 Error Propagation in Derived Parameters of Interest

The final step in obtaining estimates for the stated parameters of interest is to determine the errors in these estimates associated with measurement precision. Assuming the errors are small, a Taylor expansion may be used to map errors from one set of random variables to another. Specifically, a quantity of interest, $\mathrm{G}(\boldsymbol{\gamma})$, that is a function of a set of random variables, $\boldsymbol{\gamma} = \{\gamma_1, \gamma_2, \cdots, \gamma_k\}$, might be approximated by the Taylor series [43]

$$G(\boldsymbol{\gamma}) \approx G(\bar{\boldsymbol{\gamma}}) + \left.\frac{\partial G}{\partial \gamma_1}\right|_{\bar{\boldsymbol{\gamma}}} (\gamma_1 - \bar{\gamma_1}) + \left.\frac{\partial G}{\partial \gamma_2}\right|_{\bar{\boldsymbol{\gamma}}} (\gamma_2 - \bar{\gamma_2}) + \cdots = G(\bar{\boldsymbol{\gamma}}) + \nabla_{\boldsymbol{\gamma}} G \cdot (\boldsymbol{\gamma} - \bar{\boldsymbol{\gamma}}) + \cdots \tag{D.7}$$

where $\bar{\boldsymbol{\gamma}}$ is the expected value of the initial set of random variables.

Then the variance of this derived random variable is, for small fluctuations in $\boldsymbol{\gamma}$ about the mean [43],

$$\sigma_G^2 = \left(\overline{G - \bar{G}}\right)^2 = \sum_{i,j=1}^{n} \left.\frac{\partial G}{\partial \gamma_i}\right|_{\bar{\boldsymbol{\gamma}}} \left.\frac{\partial G}{\partial \gamma_j}\right|_{\bar{\boldsymbol{\gamma}}} \overline{(\gamma_i - \bar{\gamma_i})(\gamma_j - \bar{\gamma_j})}. \tag{D.8}$$

Here, $\overline{(\gamma_i - \bar{\gamma_i})(\gamma_j - \bar{\gamma_j})}$ is the ijth correlation coefficient, C_{ij}. It can be shown that [43, chap. 14.1]

$$C_{ij}^{-1} = \frac{1}{2} E\left\{\frac{\partial^2 \chi^2}{\partial\gamma_i \partial\gamma_j}\right\} \tag{D.9}$$

where $E\{\}$ denotes the expectation value of a quantity and χ^2 is defined in Equation 3.4. But this is none other than half the ijth element of the Hessian matrix of scalar norm, χ^2. From equation D.6, we approximate D.8 in terms of the Hessian matrix, $\mathrm{H}(\chi^2_{ex})$, evaluated using the experimentally-determined values for the inverse variances[1], $\mathbf{w}$

$$\sigma_G^2 = \left(\overline{G - \bar{G}}\right)^2 = \sum_{i,j=1}^{n} \left.\frac{\partial G}{\partial\gamma_i}\right|_{\bar{\boldsymbol{\gamma}}} \left.\frac{\partial G}{\partial\gamma_j}\right|_{\bar{\boldsymbol{\gamma}}} (2[\mathrm{H}(\chi^2_{ex})]^{-1}_{ij}) \tag{D.10}$$

which may be written in a compact matrix notation as

$$\sigma_G^2 = 2\left(\nabla_{\boldsymbol{\gamma}} G\right)^{\mathrm{T}} \left[\mathrm{H}(\chi^2_{ex})\right]^{-1} \left(\nabla_{\boldsymbol{\gamma}} G\right) \tag{D.11}$$

where $(\nabla_{\boldsymbol{\gamma}} G)$ is the column vector containing all the partial derivatives with respect to each individual γ and where all quantities are evaluated at the expected values of the parameters, $\boldsymbol{\gamma}^*$.

The task of estimating errors is then reduced to evaluating D.11 for each derived quantity of interest (e.g. G $\rightarrow D$, where $D = (R_e/\gamma_4)^2$, etc.).

In order to calculate the error propagated to the extracted real-valued parameters, it is necessary to construct a norm for the error which is positive definite, which would require some generalization of 3.4 due to the fact that the trial function - the impedance - is complex-valued. For the purposes of fitting, it was proposed that the same formalism might be appled for both the real and imaginary components of Z, and this is, inded, is the method employed here in fitting calculations. However, it is now convenient to redefine χ^2 to be

$$\chi^2 = \sum_{k=1}^{n} w_k (y_k - Z(\omega_k; \boldsymbol{\gamma}))(y_k - Z(\omega_k; \boldsymbol{\gamma}))^*, \tag{D.12}$$

[1]This is an approximation because the experimental $\mathbf{w}$ are used.

where the superscript asterisk indicates the complex conjugate transpose.

The Hessian matrix for χ^2 is determined as follows:

$$\begin{aligned}
\mathrm{H}\left\{\chi^2\right\}_{\mu\nu} &= \mathrm{H}\left\{\sum_{k=1}^{n} w_k \left|y_k - Z(\omega_k;\boldsymbol{\gamma})\right|^2\right\}_{\mu\nu} \\
&= \sum_{k=1}^{n} w_k[\mathrm{H}\left\{Z(\omega_k;\boldsymbol{\gamma})\right\}_{\mu\nu}\left(Z(\omega_k;\boldsymbol{\gamma}) - y_k\right)^* + \mathrm{H}\left\{Z^*(\omega_k;\boldsymbol{\gamma})\right\}_{\mu\nu}\left(Z(\omega_k;\boldsymbol{\gamma}) - y_k\right) \\
&+ \mathcal{J}\{Z^*(\omega_k;\boldsymbol{\gamma})\}_{k\mu}\mathcal{J}\{Z(\omega_k;\boldsymbol{\gamma})\}_{k\nu} + \mathcal{J}\{Z(\omega_k;\boldsymbol{\gamma})\}_{k\mu}\mathcal{J}\{Z^*(\omega_k;\boldsymbol{\gamma})\}_{k\nu}],
\end{aligned} \tag{D.13}$$

where $\mathcal{J}_{k\mu}\{\}$ is the $k\mu^{th}$ component of the Jacobian matrix operator as defined in Equations D.2 to D.5. Because $\mathcal{J}\{Z^*\} = (\mathcal{J}\{Z\})^*$ and $\mathrm{H}\{Z^*\} = (\mathrm{H}\{Z\})^*$,

$$\mathrm{H}\left\{\chi^2\right\}_{\mu\nu} = 2\sum_{k=1}^{n} w_k \Re\left[\mathrm{H}\left\{Z(\omega_k;\boldsymbol{\gamma})\right\}_{\mu\nu}\left(Z(\omega_k;\boldsymbol{\gamma}) - y_k\right)^* + \mathcal{J}^*_{k\mu}\mathcal{J}_{k\nu}\right], \tag{D.14}$$

with $\Re[A]$ is the real part of A. [2] $\mathrm{H}\left\{Z(\omega_k;\boldsymbol{\gamma})\right\}$ is a 4×4 matrix symmetric about the main diagonal. Its elements are:

$$\begin{aligned}
\mathrm{H}_{11} &= \mathrm{H}_{12} = \mathrm{H}_{13} = \mathrm{H}_{14} = \mathrm{H}_{22} = 0 \\
\mathrm{H}_{23} &= \frac{1}{2(j\omega + \gamma_3)}\left(f'(x)\gamma_4 - \frac{f(x)}{\sqrt{j\omega + \gamma_3}}\right) \\
\mathrm{H}_{24} &= f'(x) \\
\mathrm{H}_{34} &= \frac{1}{2}\frac{\gamma_2\gamma_4 f''(x)}{\sqrt{j\omega + \gamma_3}} \\
\mathrm{H}_{33} &= \frac{1}{2}\frac{1}{j\omega + \gamma_3}\left(\gamma_4\mathrm{H}_{34} - 3\gamma_2\mathrm{H}_{23}\right) \\
\mathrm{H}_{44} &= \gamma_2\sqrt{j\omega + \gamma_3} f''(x),
\end{aligned} \tag{D.15}$$

where $x \equiv \gamma_4\sqrt{j\omega + \gamma_3}$ and $f''(x) = 2f^3(x) - \frac{3}{x}f^2(x) - 2f(x) + \frac{1}{x}$, and again,

[2] It is also useful to point out that $Z^*(\boldsymbol{\omega};\boldsymbol{\gamma}) = Z(-\boldsymbol{\omega};\boldsymbol{\gamma})$.

$f(x) = \frac{\mathrm{M}_0(x)}{\mathrm{M}_1(x)}$. The rest of the elements are known from symmetry. For completeness, the parameter gradients for the diffusivity, linearized adsorption rate, coverage, and utilization length are given below.

$$\nabla_{\boldsymbol{\gamma}} D = \begin{bmatrix} 0 \\ 0 \\ 0 \\ -2R_e^2/\gamma_4^3 \end{bmatrix} \tag{D.16}$$

$$\nabla_{\boldsymbol{\gamma}} \alpha = \begin{bmatrix} 0 \\ 0 \\ 1 \\ 0 \end{bmatrix} \tag{D.17}$$

$$\nabla_{\boldsymbol{\gamma}} \theta = \begin{bmatrix} 0 \\ \pm\frac{1}{2}\left(\frac{1}{4} - \frac{\gamma_4}{nq_e\ell\Gamma R_e \frac{q_e}{k_B T}\gamma_2}\right)^{-1/2}\left(\frac{\gamma_4}{nq_e\ell\Gamma R_e \frac{q_e}{k_B T}\gamma_2^2}\right) \\ 0 \\ \mp\frac{1}{2}\left(\frac{1}{4} - \frac{\gamma_4}{nq_e\ell\Gamma R_e \frac{q_e}{k_B T}\gamma_2}\right)^{-1/2}\left(\frac{1}{nq_e\ell\Gamma R_e \frac{q_e}{k_B T}\gamma_2}\right) \end{bmatrix} \tag{D.18}$$

$$\begin{aligned} \nabla_{\boldsymbol{\gamma}} l_\delta = \nabla_{\boldsymbol{\gamma}} \sqrt{D/\gamma_3} &= \frac{1}{2}\sqrt{\frac{1}{\gamma_3 D}}\left(\nabla_{\boldsymbol{\gamma}} D - \frac{D}{\gamma_3}\nabla_{\boldsymbol{\gamma}}\gamma_3\right) \\ &= -\frac{1}{2}\frac{1}{\sqrt{\gamma_3 D}}\begin{bmatrix} 0 \\ 0 \\ D/\gamma_3 \\ 2R_e^2/\gamma_4^3 \end{bmatrix} \end{aligned} \tag{D.19}$$

Lastly, it should be noted that the errors estimated from this procedure are only those resulting from the limit of experimental precision in measurements and setup; these estimates say nothing about how accurate the underlying theory is. To address this issue, we compare the experimentally-determined results with available literature data and our crude first-principles estimates.

D.3 Approximation for Ratio of Modified Bessel Function

In the expression for the cylindrical Faradaic impedance, C.40, there is a term proportional to the ratio of the zeroth- and first-order modified Bessel functions of the first kind, $f(x) \equiv M_0(x)/M_1(x)$, where x is a real number and $J_n(jx)/j^n = M_n(x)$, with J_n the nth-order Bessel of the first kind and M_n the nth-order modified Bessel function of the first kind. Because this is the ratio of the lowest-order eigenfunction in cylindrical coordinates and its first derivative, it may be compared to a ratio of hyperbolic functions like tanh or coth, and indeed its behavior is similar to that of coth, but with a stronger singularity at zero argument and a slower convergence to unity. A convenient tool for calculating the ratio of Bessel functions does not seem to exist in MATLAB®, and the individual modified Bessel functions exceed the maximum size of double precision quantities when the real portion of the argument exceeds 700. However, a ratio of tabulated polynomial approximations for the modified Bessel function may be used to approximate the function for large arguments [1].

For the convenience of future users of this method, the coefficients used to estimate the ratio in $f(x)$ are tabulated below in order of highest-order coefficient to zero-order. These coefficients are calculated from those provided in [1] for the individual modified Bessel functions. The numbers of given as MATLAB code; the reader may implement the code as a MATLAB function:

```
cRatio=[0.00005552948079670...
 -0.00055797090136633...
 0.00235024942138674...
 -0.00556183154959959...
 0.00835900945593707...
 -0.00851043374776648...
 0.00621119175968176...
 -0.00264779529352971...
 0.00172310887399821...
```

```
 -0.06705071494922321...
 0.12212359788455404...
 -0.10069929872563232...
 0.04812819010930715...
 -0.00404265668853017...
 0.02804446259747899...
 0.13326780004365546...
 1.00000000000000000];

%Use approximation for arguments > 700
index = find(real(x) > 700, 1, 'last');
if(isempty(index))
    y = besseli(0,x) ./ besseli(1,x) ;
else
    y( 1:index,1 ) = polyval( cRatio, (3.75./x( 1:index )) );
    y(index+1:length(x),1)=besseli(0,x(index+1:length(x))./ ...
       (besseli(1,x(index+1:length(x))));
end
```

Figure D-1 displays the accuracy of the approximation for purely real arguments less than 700, as compared to the native modified Bessel functions in MATLAB. Note that the approximation is only used for arguments with real components greater than 700.

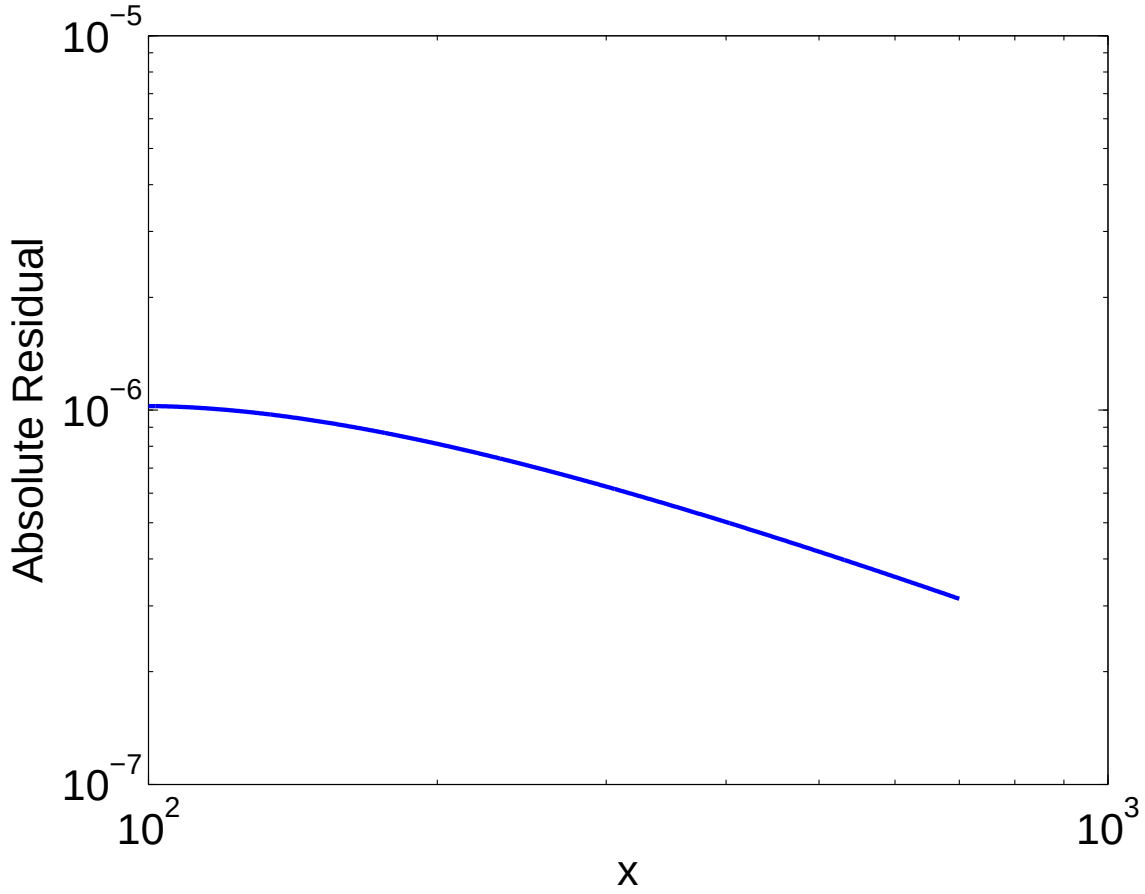

Figure D-1: Absolute error of polynomial approximation to ratio of zeroth- and first-order modified Bessel functions of the first kind, $f(x)$ against real input, x. The value for this range of arguments is close to unity.

Appendix E

Generalization of Result in Mitterdorfer and Gauckler: Coverage at Maximum i_0

The following generalizes a result obtained in Mitterdorfer and Gauckler [36] - namely, that the exchange current density is maximized at a given temperature by the value, $1-\zeta$, where ζ is the energy exchange coefficient (or Tafel constant).

A basic relation in electrochemistry relating Faradaic current, I_F, to overpotential, v, is the Butler-Volmer equation, which in two dimensions is written as

$$I_F = i_0 \ell \left(e^{b_{-1} v} - e^{b_1 v} \right), \tag{E.1}$$

where the b's are defined in C.18a.

By comparison with 2.24, we see that the Butler-Volmer equation arises when $k_{-1,0}\mathrm{O}_{\mathrm{O}}^{\times}(1-\theta) = k_{1,0}\mathrm{V}_{\ddot{\mathrm{O}}}\theta$. In this case,

$$i_0 = n q_e \Gamma k_{-1,0}\mathrm{O}_{\mathrm{O}}^{\times}(1-\theta) = n q_e \Gamma k_{1,0}\mathrm{V}_{\ddot{\mathrm{O}}}\theta. \tag{E.2}$$

In general, we might subtract an offset from the overpotential, η to enforce this relationship, where η is defined through

$$\begin{aligned} k_{-1,0} &= k_{-1,c}e^{-b_{-1}\eta} \\ k_{1,0} &= k_{1,c}e^{-b_1\eta} \end{aligned} \tag{E.3}$$

such that 2.24 can be written as

$$I_F = nq_e\ell\Gamma\left[k_{-1,c}e^{b_{-1}(v-\eta)}\mathrm{O}_{\mathrm{O}}^{\times}(1-\theta) - k_{1,c}e^{b_1(v-\eta)}\mathrm{V}_{\ddot{\mathrm{O}}}\theta\right]. \tag{E.4}$$

To convert this expression to Butler-Volmer form, we require

$$k_{-1,c}e^{-b_{-1}\eta}\mathrm{O}_{\mathrm{O}}^{\times}(1-\theta) = k_{1,c}e^{-b_1\eta}\mathrm{V}_{\ddot{\mathrm{O}}}\theta. \tag{E.5}$$

This constrains η to be

$$\eta = \frac{1}{b_1 - b_{-1}}\ln\left(\frac{k_{1,c}\mathrm{V}_{\ddot{\mathrm{O}}}}{k_{-1,c}\mathrm{O}_{\mathrm{O}}^{\times}}\frac{\theta}{1-\theta}\right). \tag{E.6}$$

Now, the forward and backward current under the Butler-Volmer condition become

$$i_0 = nq_e\Gamma k_{-1,c}e^{-b_{-1}\eta}\mathrm{O}_{\mathrm{O}}^{\times}(1-\theta) = nq_e\Gamma k_{1,c}e^{-b_1\eta}\mathrm{V}_{\ddot{\mathrm{O}}}\theta. \tag{E.7}$$

In Mitterdorfer and Gauckler's work, an expression for i_0 is obtained by taking the square root of the product of the forward and backward exchange currents at equilibrium [36][1],

$$i_0 = nq_e\Gamma\sqrt{e^{(-(b_{-1}+b_1))\eta}k_{-1,c}\mathrm{O}_{\mathrm{O}}^{\times}k_{1,c}\mathrm{V}_{\ddot{\mathrm{O}}}\theta(1-\theta)} \tag{E.8}$$

It is subsequently demonstrated in [36] that, for the specific case of Langmuir adsorption, the equilibrium surface concentration at which i_0 is maximized occurs at

$$\theta^* = 1 - \zeta. \tag{E.9}$$

[1] I am not altogether sure that this is a valid operation, but the goal here is to generalize the development of these authors.

In fact, this result is more general. Using Mitterdorfer and Gauckler's procedure for obtaining i_0, E.9 is seen to be a consequence of the charge transfer model employed, and not the isotherm (so that any isotherm might be employed without changing the value for θ^* so long as the same style of charge transfer reaction, 2.24, is used). To see this, substitute the expression for η into E.8:

$$i_0 = nq_e\Gamma\sqrt{\left(\frac{k_{1,c}\mathrm{V}_{\ddot{\mathrm{O}}}\theta}{k_{-1,c}\mathrm{O}_{\mathrm{O}}^{\times}(1-\theta)}\right)^{(b_{-1}+b_1)/(b_{-1}-b_1)} k_{-1,c}\mathrm{O}_{\mathrm{O}}^{\times}(1-\theta)k_{1,c}\mathrm{V}_{\ddot{\mathrm{O}}}\theta} \tag{E.10}$$

Noting that (after considering C.18a)

$$\frac{b_{-1}+b_1}{b_{-1}-b_1} = 1-2\zeta, \tag{E.11}$$

we find

$$i_0 = nq_e\Gamma\left[k_{1,c}\mathrm{V}_{\ddot{\mathrm{O}}}\theta\left(\frac{k_{-1,c}\mathrm{O}_{\mathrm{O}}^{\times}(1-\theta)}{k_{1,c}\mathrm{V}_{\ddot{\mathrm{O}}}\theta}\right)^{\zeta}\right] = nq_e\Gamma\left[\left(k_{1,c}\mathrm{V}_{\ddot{\mathrm{O}}}\theta\right)^{1-\zeta}\left(k_{-1,c}\mathrm{O}_{\mathrm{O}}^{\times}[1-\theta]\right)^{\zeta}\right]. \tag{E.12}$$

The desired quantity is the coverage which maximizes the exchange current density, i_0, *at a given temperature*. As such, we maximize E.13 with respect to the other control (and state) parameter, pressure, P. We will take the k's to be electrochemical constants, and all other parameters except θ to be independent of pressure.

$$\left(\frac{\partial i_0}{\partial P}\right)_T = nq_e\Gamma\left[\left(k_{1,c}\mathrm{V}_{\ddot{\mathrm{O}}}\right)^{1-\zeta}\left(k_{-1,c}\mathrm{O}_{\mathrm{O}}^{\times}\right)^{\zeta}\right]\frac{\mathrm{d}}{\mathrm{d}P}\left[\theta^{1-\zeta}(1-\theta)^{\zeta}\right] = 0 \tag{E.13}$$

This requires

$$\frac{\mathrm{d}}{\mathrm{d}P}\left[\theta^{1-\zeta}(1-\theta)^{\zeta}\right] = \theta'\frac{\mathrm{d}}{\mathrm{d}\theta}\left[\theta^{1-\zeta}(1-\theta)^{\zeta}\right] = 0, \tag{E.14}$$

after application of the chain rule, where $\theta' \equiv \mathrm{d}\theta/\mathrm{d}P$. The key step is not to specify the isotherm through leaving unknown the functional dependence of θ on P.

The only constraint made on the isotherm is that θ' is not zero (which would be very unrealistic for the given situation). Then the other term in E.14 must be zero, namely,

$$\frac{\mathrm{d}}{\mathrm{d}\theta}\left[\theta^{1-\zeta}(1-\theta)^{\zeta}\right] = (1-\zeta)\left(\frac{1-\theta}{\theta}\right)^{\zeta} - \zeta\left(\frac{1-\theta}{\theta}\right)^{\zeta-1} = 0 \qquad \text{(E.15)}$$

The only allowable root of this constraint, θ^*, is $\theta^* = 1-\zeta$. As such, we have demonstrated that, using the same starting point as in Mitterdorfer and Gauckler, the result that $\theta^* = 1-\zeta$ is valid *independently* of the isotherm used, so that it must be a consequence of the model used to describe the charge transfer step.

Appendix F

Selected Literature Values For Model Parameters

The following tables list literature values from multiple sources for several model parameters.

F.1 Sticking Probability

Most experimental works observe and argue for a coverage dependence of the oxygen sticking probability according to $S(\theta) = S_0(1-\theta)^2$[17, 54, 58, 15]; this corresponds to a site-limited view of adsorption. Hopster et al. suggest a more complicated $S(\theta) = S_0 \exp -A\frac{\theta^{3/2}}{k_B T}$ dependence from their studies, and estimate S_0 at 0.018 with $A = 3.2$ eV; this model was employed by Sales et al. in their studies of oxygen adsorption [44], but is otherwise not popular in the literature.

Table F.1 shows zero-coverage sticking coefficients obtained from the literature for several different experimental conditions. All of the data pertains to clean or stepped single-crystal surfaces. The authors use a wide variety of techniques, including Auger spectroscopy [20] to single crystal adsorption calorimetry [56] and second harmonic generation [15].

Table F.1: Zero-Coverage Sticking Coefficient: Values in the Literature

Source	Value	Description
[15]	0.054	On clean Pt(111) at 300 K
	0.023	On clean Pt(111) at 600 K
	0.02	High temperature asymptote, with monotonic decay from low to high temperatures
[17]	0.05	On clean Pt(111) at 200 K
	0.4	On stepped Pt(S)-12(111)×(111) surface at 200 K
[54]	0.14	On Pt(110) at room temperature (300 K)
[56]	0.05	On clean Pt(111) at room temperature (300 K)
[58]	0.03	On clean Pt(111) at 160 K
[20]	0.02	On clean Pt(111) at 550 K using Auger spectroscopy
	0.03	On stepped Pt(S)-14(111)×(111) at 550 K, argue $S(\theta) = S_0 \exp -A\frac{\theta^{3/2}}{k_B T}$, $S_0 = 0.018$, A = 3.2 eV for O_2 on Pt(111)

F.2 Chemisorption Energies

There is significant scatter in the literature among adsorption energies for oxygen on Pt(111). This may be due to differences in sample preparation and experimental conditions, as well as inaccurate means of assessing coverage, presence of contaminants, and so forth. To give some context to these numbers, we might use the adsorption isotherm model without including lateral interactions. For the lowest temperature visited in the experiments carried out in this work, 476℃, a binding energy of 1.1 eV [25] would require a pressure of about 10^5 Pa (about 1 atm oxygen partial pressure) to reach 95 % saturation coverage; by contrast, a binding energy of 2.6 eV would reach 95 % saturation coverage at around 10^{-15} Pa [18].

One lesson to be learned from this tremendous spread in energetics data is that caution should be exercised when comparing energetics values obtained by different methods of analysis. Fits to data as in Wilf et al.[54], Kreuzer et al.[25], and other works may not necessarily correspond to those values obtained by *ab initio* calculations [7, 33, 8]. This is especially important when looking for trends in adsorption/desorption energy; in this case, it is perhaps more instructive to compare trends determined by several data sets all using the same analysis method.

Another key point is that the model used here, which uses a single binding and a single interaction energy, is an extreme simplification from the complexities of actual oxygen sorption on Pt. Lynch and Hu examine four different binding configurations on Pt(111) alone [33]; Lewis and Gomer report on local Pt{100} sites acting as traps to diffusion along Pt{111} facets [30]. But it is important to remember our purpose in examining sorption, which is to get an idea of how coverage depends upon temperature and pressure, rather than to determine precise atomic details which, aside from which, are best analyzed by more direct means (e.g. low-energy electron diffraction, etc.). And we desire the simplest model possible which will nonetheless describe these trends with some degree of quantitative accuracy. Ideally, the complex microscopic details will be sufficiently "washed out" from a macroscopic (i.e. micrometer scale) statistical point of view to make our simplified model adequate.

The format in which binding energy is reported varies. Some sources give the energy relative to a ground state of isolated monatomic oxygen. This is especially true in DFT studies, for which it is convenient to calculate energies with oxygen atoms separated from the Pt surface at the bond length, and then again at a large separation, taking the binding energy to be the difference of the two states. Because this method is employed by Nørskov et al.[8, see p. 257], and because the binding energies reported in the other DFT studies [7, 33, 49], as well as some experimental studies [18], approach the value shown by Nørskov, it is assumed that the ground state in these works is also isolated monatomic oxygen. However, the thermodynamic model employed here identifies $\frac{1}{2}O_2$ and O/Pt as the only two states available for oxygen atoms. As such, it is appropriate to use $\frac{1}{2}O_2$ as the ground state. To convert from the binding energy relative to monatomic gaseous oxygen, V_a, to that relative to half diatomic gaseous oxygen, ϵ, we use the heat of fission of gaseous O_2, $D_e^g = 5.28$ eV [31, for about 900 K $\approx$ 630 ℃] (5.26 eV, [25]) $\epsilon = (2V_a - D_e^g)/2$.

(Key to abbreviations: LEED = Low-Energy Electron Diffraction, EELS = Electron Energy Loss Spectroscopy, TDS = Thermal Desorption (mass) Spectroscopy, AES = Auger Electron Spectroscopy, UPS = Ultraviolet Photoemission Spectroscopy, DFT = Density Functional Theory (an *ab initio* technique for quantum calculations).)

Table F.2: Chemisorption Binding Energetics Per Atomic O on Pt, Relative to $\frac{1}{2}$ Gaseous O_2 (Estimates for ϵ)

Source	Value [eV]	Description
[56]	1.6	On clean Pt(111) at room temperature (300 K) - single crystal adsorption calorimetry; quote energy of 3.16 eV as energy difference between $O_{2,gas}$ and $2O_{ads}$/Pt
[25]	1.1	On clean Pt(111), fitting from TDS data by [3]. This value results from stressing recovery of accurate zero-coverage desorption energy; when first TDS peak is stressed, a binding energy of 1.4 eV results. Value is probably most appropriate for this work since the model employed is similar to the one used here. Should not, as such, necessarily be interpreted as a true Pt-O binding energy.
[18]	2.6	On Pt(111) at zero coverage using LEED, EELS; Gland et al. actually report the desorption energy for O on Pt(111) as 5.2 eV; converted to relative $\frac{1}{2}O_2$ through method described above.
[15]	2.1-2.2	For Pt(111), citing work of Campbell et al., Winkler et al., and Parker et al. *Desorption energies*, not, strictly speaking, binding energies, as may include an activation.
[40]	2.3	Porous Pt; value determined by analysis of dc electrode conductivities, σ_E, under both anodic and cathodic polarizations and measured at temperatures between 370 and 800℃ and oxygen partial pressures between 10^{-4} and 1 atm. Analysis carried out according to [39] and involves examining Arrhenius behavior of pressure which minimizes σ_E.
Continued on next page		

Source	Value [eV]	Description
[54]		On Pt(110), TDS with LEED and AES, 400-1000 K (330-730℃), high vacuum (10^{-9} Torr) even during O_2 dosing. Isotopic mixing of O^{16} and O^{18} in O_2 formed after desorption implies *dissociative adsorption*. Identify two *desorption* phases, β_1 and β_2, distinguished by first-order (direct) and second-order (associative) *desorption* kinetics. Numbers found by Arrhenius fitting to TDS peaks.
	1.4	β_1 desorption activation energy
	1.3	β_2 desorption activation energy
[49]	1.79	On clean Pt(111) at fcc site, DFT study (0 K); again, quote energy of 4.43 eV; converted to relative $\frac{1}{2}O_2$ through method described above.
[7]	1.79	clean Pt(111), p(2 × 2) ordering, DFT study (0 K); quote energy of 4.43 eV; converted to relative $\frac{1}{2}O_2$ through method described above.
[33]		DFT study on Pt(111) using a p(2×2) unit cell. Chemisorption energies given for four potential binding sites on Pt(111) surface.
	1.15	hcp hollow
	1.62	fcc hollow (most stable)
	0.99	bridge
	-0.01	top (slightly unstable relative to $\frac{1}{2}O_2$)

F.3 Lateral Interactions

As a point of clarification, lateral interactions here refer to the interactions between adsorbates which modify the energetics of adsorbed particles in a thermodynamic sense.

There is an important conceptual difference in the treatment of lateral interactions in this work and those listed in the table below. Many of the works in the literature, and all of those referred to in Table F.3, attempt to isolate interaction energies between specific configurations of chemisorbed atoms (always nearest-neighbor pairs except in [49]). This assumes a specific form of the interaction potential. An advantage of the mean field theory is that it does not make assumptions about the interaction potential, but rather approximates the occupation probability as being roughly independent of the coverage (see B.2). The parameter, u_0, which controls the contribution of lateral interactions in this model is simply the total interaction energy of one adsorbate with all particles on a completely covered surface. The correspondence between these two points of view is found by calculating the total interaction energy for a surface at saturation coverage given the potential used in the determination of the interaction energy. For all of the energetics data reported below with the exception of that from [49], the correspondence with u_0 is either exactly or nearly six times the energy, where six is the number of nearest neighbors on the Pt(111) surface and the p(2×2) covering.

(Note: positive values in the energetics values below indicate *repulsive* interactions; negative values, *attractive*.)

F.4 Diffusion

(Key to abbreviations: PEEM = Photoemission Electron Microscopy)

Table F.3: Interaction Energies Between Chemisorbed Oxygen Atoms

Source	Value [eV]	Description
[49]		From DFT calculations on Pt(111); a set of various interaction combinations used together in diagram expansion to treat interactions more comprehensively.
	0.237	Isolated nearest-neighbor pairwise interaction on (1×1) surface.
	0.0395	Isolated pairwise interaction, nearest-neighbor on $(\sqrt{3}\times\sqrt{3})$ surface, second-nearest-neighbor on (1×1).
	-0.00581	Isolated pairwise interaction, nearest-neighbor on p(2×2), third-nearest-neighbor on (1×1).
		Three-way interactions are also included in [49].
[56]	0.228	On clean Pt(111) at room temperature (300 K) - single crystal adsorption calorimetry. The number is obtained by fitting to data via Monte Carlo simulations assuming nearest-neighbor interaction, only, in a p(2×2) ordering on the surface. Actually report 1.68 eV as the energy difference between a fully covered and a clean surface where $1.68/6 \approx 0.28$ eV.
[25]	0.023	From thermodynamic model fits to TDS spectra by [3], which refers to clean Pt(111). They reference 0.072 eV [11, 41] and 0.038 eV [55] for comparison.

Table F.4: Diffusion Activation Energy

Source	Value [eV]	Description
[30]		Pt(111) and (100) field emitter tips, high vacuum. Pt(111) more mobile than Pt(100).
	1.2	450-500 K (180-230℃) and high coverage.
	1.5	$>$ 500 K (230℃) and low coverage.
[20]	$1.6 \times \theta^{3/2}$	see Table F.1; claim that E_d can be estimated as half desorption energy, and report $3.2 \times \theta^{3/2}$ eV as heat of *adsorption*.
[40]	1.8	See Table F.2
[53]		Single-crystal Pt(110) at 606-668 K, use PEEM; grow oxygen islands on a CO monolayer, then raise temperature so that CO desorbs completely while oxygen islands stay; subsequently, image in real time diffusion of oxygen islands. Argue that change in diffusion activation energy at $\theta = 0.2$ is related to adsorption occurring on valley sites of (2×1), where before, it occurred primarily at ridge sites. $[1\bar{1}0]$ is the preferred direction.
	1.3 ± 0.17	low coverage ($\theta < 0.2$)
	1.7 ± 0.86	high coverage ($0.2 < \theta < 0.7$)

Table F.5: Diffusion Preexponential Factor

Source	Value [cm^2/s]	Description
[30]	2.5	see Table F.4
[53]		see Table F.4
	$2 \times 10^{3\pm1}$	low coverage ($\theta < 0.2$)
	$2 \times 10^{5\pm0.5}$	high coverage ($0.2 < \theta < 0.7$)

Appendix G

About The Author

As of the submission of this thesis, Theodore (Ted) Golfinopoulos is a graduate student in the Electrical Engineering and Computer Science Department at MIT. He completed a bachelors degree in mechanical engineering and a bachelors degree in electrical engineering at Rensselaer Polytechnic Institute in the spring of 2006. He was born in the city so nice, they named it twice: New York, New York. He grew up in a suburb of this city, Croton-on-Hudson, with his mother, Sara, father, Elias, and sister, Elisa. He enjoys learning, teaching, and doing.

Currently, a large portion of his free time is devoted to work for Middle East Education through Technology (MEET), an incredible program based in Jerusalem which brings together excelling Israeli and Palestinian high school students into a fast-paced curriculum of computer science and entrepreneurship. And the rest of his time out of the lab belongs to family and friends.

Ted believes that science represents the purest ambition of the human intellect to better itself, and engineering the greatest tool for a society to better itself.

Figure G-1: The author at age 24 in Zurich, Switzerland, en route to MEET, July 2008.

Bibliography

[1] M. Abramowitz and I. A. Stegun, editors. *Handbook of Mathematial Functions*. Dover Publications, Inc., NY, 9th edition, 1970.

[2] S. B. Adler. *Chem. Rev.*, 104(10):4791–4843, Oct.

[3] K. Allers, H. Pfnur, P. Feulner, and D. Menzel. *Phys. Chem. (Munich)*, 197:253, 1996.

[4] J. Barth. *Surface Science Reports*, 40(3-5):75–149, Oct. 2000.

[5] F. Berthier, J.-P. Diard, B. Le Gorrec, and C. Montella. *Corrosion*, 51:105–115, 1995.

[6] W. Bessler. *Solid State Ionics*, 176(11-12):997–1011, Mar. 2005.

[7] K. Bleakley and P. Hu. *J. Am. Chem. Soc.*, 121(33):7644–7652, 1999.

[8] T. Bliggard and J. K. Nørskov. *Chemical Bonding at Surfaces*, chapter 4: Heterogeneous Catalysis, pages 255–321. Elsevier B.V., Amsterdam, 2008.

[9] G. Bokun, Y. Groda, C. Uebing, and V. Vikhrenko. *Physica A*, 296(14):83–105, Jan. 2001.

[10] B. A. Boukamp and H. J. Bouwmeester. *Solid State Ionics*, 157:2933, 2003.

[11] C. T. Campbell, G. Ertl, H. Kuipers, and J. Segner. *Surface Science*, 107:220, 1981.

[12] A. Cassuto and D. King. *Surface Science*, 102(2-3):388–403, Jan. 1981.

[13] U. S. Congress. Public law 110-140-dec. 19, 2007: Energy independence and security act of 2007. Available from the Library of Congress website, http://thomas.loc.gov/cgi-bin/bdquery/z?d110:H.R.6:.

[14] A. Eichler and J. Hafner. *Physical Review Letters*, 79(22):4481–4484, 1997.

[15] A.-P. Elg, F. Eisert, and A. Rosón. *Surface Science*, 382(1-3):57–66, June 1997.

[16] E. D. German, I. Efremenk, A. M. Kuznetsov, and M. Sheintuch. *J. Phys. Chem. B.*, 106:11784–11794, 2002.

[17] J. Gland. *Surface Science*, 93(2-3):487–514, 1980.

[18] J. Gland, B. Sexton, and G. Fisher. *Surface Science*, 95(2-3):587–602, May 1980.

[19] J. Hertz. Ph.d., Massachusetts Institute of Technology, September 2006.

[20] H. Hopster, H. Ibach, and G. Comsa. *Journal of Catalysis*, 40:37–48, 1977.

[21] C. J. Jacobsen, S. Dahl, B. S. Clausen, S. Bahn, A. Logadottir, and J. K. Nørskov. *Journal of the American Chemical Society*, 123:8404–8405, 2001.

[22] M. Kardar. *Statistical Physics of Particles*. Cambridge University Press, 1st edition, 2007.

[23] H. Kishimoto, N. Sakai, K. Yamaji, T. Horita, M. Brito, H. Yokokawa, K. Amezawa, and Y. Uchimoto. *Solid State Ionics*, 179:347–354, 2008.

[24] M. Kotur-Załuska and Z. W. Gortel. *Physical Review B*, 72:235425, Dec. 2005.

[25] H. Kreuzer, S. Payne, A. Drozdowski, and M. D. *Journal of Chemical Physics*, 110(14):6982–6999, April 1999.

[26] G.-J. la O'. Ph.d., Massachusetts Institute of Technology, January 2008.

[27] G.-J. la O', B. Yildiz, S. McEuen, and Y. Shao-Horn. *Journal of the Electrochemical Society*, 154:B427–B438, 2007.

[28] I. Langmuir. *Phys. Rev.*, 8:48, 1916.

[29] P. Légaré. *Surface Science*, 580:137–144, 2005.

[30] R. Lewis and R. Gomer. *Surface Science*, 12:157–176, 1968.

[31] D. R. Lide, editor. *CRC Handbook of Chemistry and Physics*, chapter 9: Characteristic Bond Lengths in Free Molecules. CRC Press, Taylor and Francis Group LLC, Boca Raton, FL, 88th edition, Internet Version 2008.

[32] C. Lin and L. Segel. *Mathematics Applied to Deterministic Problems in the Natural Sciences*. SIAM, Dec 1988.

[33] M. Lynch and P. Hu. *Surface Science*, 458:1–14, 2000.

[34] J. R. Macdonald, editor. *Impedance Spectroscopy: Emphasizing Solid Materials and Systems*. John Wiley & Sons, 1st edition, 1987.

[35] M. Mavrikakis, B. Hammer, and J. K. Nørskov. *Physical Review Letters*, 81(13):2819–2822, Sept. 1998.

[36] A. Mitterdorfer and L. Gauckler. *Solid State Ionics*, 117(3-4):187–202, Feb. 1999.

[37] A. Mitterdorfer and L. Gauckler. *Solid State Ionics*, 117(3-4):203–217, Feb. 1999.

[38] A. Mitterdorfer and L. Gauckler. *Solid State Ionics*, 120(1-4):211–225, May 1999.

[39] J. Mizusaki, K. Amano, S. Yamauchi, and K. Fueki. *Solid State Ionics*, 22(4):313–322, Feb. 1987.

[40] J. Mizusaki, K. Amano, S. Yamauchi, and K. Fueki. *Solid State Ionics*, 22(4):323–330, Feb. 1987.

[41] D. H. Parker, M. E. Bartram, and B. E. Koel. *Surface Science*, 217:489, 1989.

[42] D. Reed and G. Ehrlich. *Surface Science*, 102(2-3):588–609, Jan. 1981.

[43] B. P. Roe. *Probability and Statistics in Experimental Physics*. Undergraduate Texts in Contemporary Physics. Springer-Verlag New York, Inc., second edition, 2001.

[44] B. Sales, J. Turner, and M. Maple. *Surface Science*, 112:272–280, 1981.

[45] Solartron Analytical, Unit B1 Armstrong Mall, Farnborough Hampshire, England GU14 0NR. *1260 Impedance/Gain Phase Analyzer Operating Manual*, 2001.

[46] Solatron Analytical, Unit B1 Armstrong Mall, Farnborough Hampshire, England GU14 0NR. *1296 Dielectric Interface User Guide*, 2003.

[47] Solatron Analytical, Unit B1 Armstrong Mall, Farnborough Hampshire, England GU14 0NR. *1296 Dielectric Interface (Datasheet)*, 2008.

[48] H. Steininger, S. Lehwald, and H. Ibach. *Surface Science*, 123(1):1–17, Sep. 1982.

[49] H. Tang, A. Van der Ven, and B. L. Trout. *Phys. Rev. B*, 70(4):045420, July 2004.

[50] A. Tarasenko, L. Jastrabik, and T. Muller. *Physical Review B*, 75:085401, Feb. 2007.

[51] H. Taylor. *Biographical Memoirs of Fellows of the Royal Society*, 4:167–184, Nov 1958.

[52] F. T. Ulaby. *Fundamentals of Applied Electromagnetics*. Prentice Hall, Upper Saddle River, NJ, 2001 media edition edition, 2001.

[53] A. von Oertzen, H. Rotermund, and S. Nettesheim. *Surface Science*, 311(3):322–330, May 1994.

[54] M. Wilf and P. Dawson. *Surface Science*, 65:399–418, 1977.

[55] A. Winkler, X. Guo, H. R. Siddiqui, P. L. Hagans, and J. T. J. Yates. *Surface Science*, 201:419, 1988.

[56] Y. Yeo, L. Vattuone, and D. King. *J. Chem. Phys.*, 106(1):392–401, 1997.

[57] M. Załuska-Kotur and Z. W. Gortel. *Physical Review B*, 74:045405, July 2006.

[58] T. Zambelli, J. Barth, J. Wintterlin, and G. Ertl. *Nature*, 390:495–497, Dec. 1997.